Jordan Journal of Mechanical and Industrial Engineering (JJMIE)

JJMIE is a high-quality scientific journal devoted to fields of Mechanical and Industrial Engineering. It is published by The Jordanian Ministry of Higher Education and Scientific Research in corporation with the Hashemite University.

SUBMISSION ADDRESS:

Prof. **Mousa S. Mohsen**, Editor-in-Chief Jordan Journal of Mechanical & Industrial Engineering, Hashemite University, PO Box 330127, Zarqa, 13133 , Jordan
E-mail: jjmie@hu.edu.jo

Hashemite Kingdom of Jordan

Hashemite University

Jordan Journal of Mechanical and Industrial Engineering

JJMIE

An International Peer-Reviewed Scientific Journal

http://jjmie.hu.edu.jo/

ISSN 1995-6665

Jordan Journal of Mechanical and Industrial Engineering (JJMIE)

JJMIE is a high-quality scientific journal devoted to fields of Mechanical and Industrial Engineering. It is published by The Jordanian Ministry of Higher Education and Scientific Research in corporation with the Hashemite University.

Intruduction: The Editorial Board is very committed to build the Journal as one of the leading international journals in mechanical and industrial engineering sciences in the next few years. With the support of the Ministry of Higher Education and Scientific Research and Jordanian Universities, it is expected that a heavy resource to be channeled into the Journal to establish its international reputation. The Journal's reputation will be enhanced from arrangements with several organizers of international conferences in publishing selected best papers of the conference proceedings.

Aims and Scope: Jordan Journal of Mechanical and Industrial Engineering (JJMIE) is a refereed international journal to be of interest and use to all those concerned with research in various fields of, or closely related to, mechanical and industrial engineering disciplines. Jordan Journal of Mechanical and Industrial Engineering aims to provide a highly readable and valuable addition to the literature which will serve as an indispensable reference tool for years to come. The coverage of the journal includes all new theoretical and experimental findings in the fields of mechanical and industrial engineering or any closely related fields. The journal also encourages the submission of critical review articles covering advances in recent research of such fields as well as technical notes.

Guide for Authors

Manuscript Submission

High-quality submissions to this new journal are welcome now and manuscripts may be either submitted online or mail.

Online: For online submission upload one copy of the full paper including graphics and all figures at the online submission site, accessed via E-mail: jjmie@hu.edu.jo. The manuscript must be written in MS Word Format. All correspondence, including notification of the Editor's decision and requests for revision, takes place by e-mail and via the Author's homepage, removing the need for a hard-copy paper trail.

By Mail: Manuscripts (1 original and 3 copies) accompanied by a covering letter may be sent to the Editor-in-Chief. However, a copy of the original manuscript, including original figures, and the electronic files should be sent to the Editor-in-Chief. Authors should also submit electronic files on disk (one disk for text material and a separate disk for graphics), retaining a backup copy for reference and safety.

Note that contributions may be either submitted online or sent by mail. Please do NOT submit via both routes. This will cause confusion and may lead to delay in article publication. Online submission is preferred.

Submission address and contact:

Prof. **Mousa S. Mohsen**, Editor-in-Chief
Jordan Journal of Mechanical & Industrial Engineering,
Hashemite University,
PO Box 330127, Zarqa, 13133 , Jordan
E-mail: jjmie@hu.edu.jo

Types of contributions: Original research papers

Corresponding author: Clearly indicate who is responsible for correspondence at all stages of refereeing and publication, including post-publication. Ensure that telephone and fax numbers (with country and area code) are provided in addition to the e-mail address and the complete postal address. Full postal addresses must be given for all co-authors.

Original material: Submission of an article implies that the work described has not been published previously (except in the form of an abstract or as part of a published lecture or academic thesis), that it is not under consideration for publication elsewhere, that its publication is approved by all authors and that, if accepted, it will not be published elsewhere in the same form, in English or in any other language, without the written consent of the Publisher. Authors found to be deliberately contravening the submission guidelines on originality and exclusivity shall not be considered for future publication in this journal.

Supplying Final Accepted Text on Disk: If online submission is not possible: Once the paper has been accepted by the editor, an electronic version of the text should be submitted together with the final hardcopy of the manuscript. The electronic version must match the hardcopy exactly. We accept MS Word format only. Always keep a backup copy of the electronic file for reference and safety. Label the disk with your name. Electronic files can be stored on CD.

Notification: Authors will be notified of the acceptance of their paper by the editor. The Publisher will also send a notification of receipt of the paper in production.

Copyright: All authors must sign the Transfer of Copyright agreement before the article can be published. This transfer agreement enables Jordan Journal of Mechanical and Industrial Engineering to protect the copyrighted material for the authors, but does not relinquish the authors' proprietary rights. The copyright transfer covers the exclusive rights to reproduce and distribute the article, including reprints, photographic reproductions, microfilm or any other reproductions of similar nature and translations.

PDF Proofs: One set of page proofs in PDF format will be sent by e-mail to the corresponding author, to be checked for typesetting/editing. The corrections should be returned within 48 hours. No changes in, or additions to, the accepted (and subsequently edited) manuscript will be allowed at this stage. Proofreading is solely the author's responsibility. Any queries should be answered in full. Please correct factual errors only, or errors introduced by typesetting. Please note that once your paper has been proofed we publish the identical paper online as in print.

Author Benefits

Page charge: Publication in this journal is free of charge.

Free off-prints: Three journal issues of which the article appears in along with twenty-five off-prints will be supplied free of charge to the corresponding author. Corresponding authors will be given the choice to buy extra off-prints before printing of the article.

Manuscript Preparation:

General: Editors reserve the right to adjust style to certain standards of uniformity. Original manuscripts are discarded after publication unless the Publisher is asked to return original material after use. If online submission is not possible, an electronic copy of the manuscript on disk should accompany the final accepted hardcopy version. Please use MS Word for the text of your manuscript.

Structure: Follow this order when typing manuscripts: Title, Authors, Affiliations, Abstract, Keywords, Introduction, Main text, Conclusions, Acknowledgements, Appendix, References, Figure Captions, Figures and then Tables. For submission in hardcopy, do not import figures into the text - see Illustrations. For online submission, please supply figures imported into the text AND also separately as original graphics files. Collate acknowledgements in a separate section at the end of the article and do not include them on the title page, as a footnote to the title or otherwise.

Text Layout: Use double spacing and wide (3 cm) margins. Ensure that each new paragraph is clearly indicated. Present tables and figure legends on separate pages at the end of the manuscript. If possible, consult a recent issue of the journal to become familiar with layout and conventions. All footnotes (except for table and corresponding author footnotes) should be identified with superscript Arabic numbers. To conserve space, authors are requested to mark the less important parts of the paper (such as records of experimental results) for printing in smaller type. For long papers (more that 4000 words) sections which could be deleted without destroying either the sense or the continuity of the paper should be indicated as a guide for the editor. Nomenclature should conform to that most frequently used in the scientific field concerned. Number all pages consecutively; use 12 or 10 pt font size and standard fonts. If submitting in hardcopy, print the entire manuscript on one side of the paper only.

Corresponding author: Clearly indicate who is responsible for correspondence at all stages of refereeing and publication, including post-publication. The corresponding author should be identified with an asterisk and footnote. Ensure that telephone and fax numbers (with country and area code) are provided in addition to the e-mail address and the complete postal address. Full postal addresses must be given for all co-authors. Please consult a recent journal paper for style if possible.

Abstract: A self-contained abstract outlining in a single paragraph the aims, scope and conclusions of the paper must be supplied.

Keywords: Immediately after the abstract, provide a maximum of six keywords (avoid, for example, 'and', 'of'). Be sparing with abbreviations: only abbreviations firmly established in the field may be eligible.

Symbols: All Greek letters and unusual symbols should be identified by name in the margin, the first time they are used.

Units: Follow internationally accepted rules and conventions: use the international system of units (SI). If other quantities are mentioned, give their equivalent in SI.

Maths: Number consecutively any equations that have to be displayed separately from the text (if referred to explicitly in the text).

References: All publications cited in the text should be presented in a list of references following the text of the manuscript.

Text: Indicate references by number(s) in square brackets in line with the text. The actual authors can be referred to, but the reference number(s) must always be given.

List: Number the references (numbers in square brackets) in the list in the order in which they appear in the text.

Examples:

Reference to a journal publication:

[1] M.S. Mohsen, B.A. Akash, “Evaluation of domestic solar water heating system in Jordan using analytic hierarchy process”. Energy Conversion & Management, Vol. 38, No. 9, 1997, 1815-1822.

Reference to a book:

[2] Strunk Jr W, White EB. The elements of style. 3rd ed. New York: Macmillan; 1979.

Reference to a conference proceeding:

[3] B. Akash, S. Odeh, S. Nijmeh, “Modeling of solar-assisted double-tube evaporator heat pump system under local climate conditions”. 5th Jordanian International Mechanical Engineering Conference, Amman, Jordan, 2004.

Reference to a chapter in an edited book:

[4] Mettam GR, Adams LB. How to prepare an electronic version of your article. In: Jones BS, Smith RZ, editors. Introduction to the electronic age, New York: E-Publishing Inc; 1999, p. 281-304

Free Online Color: If, together with your accepted article, you submit usable color and black/white figures then the journal will ensure that these figures will appear in color on the journal website electronic version.

Tables: Tables should be numbered consecutively and given suitable captions and each table should begin on a new page. No vertical rules should be used. Tables should not unnecessarily duplicate results presented elsewhere in the manuscript (for example, in graphs). Footnotes to tables should be typed below the table and should be referred to by superscript lowercase letters.

JJMIE
Jordan Journal of Mechanical and Industrial Engineering

JJMIE

Volume 3, Number 2, June. 2009
ISSN 1995-6665
Pages 89 - 96

Jordan Journal of Mechanical and Industrial Engineering

Development of Multi-Point Micro-Punch: The Effects of Gold Plating on Discharge Time and Punch Surface.

Mark Broomfield *, Toshihiko Mori, Teruaki Mikuriya, Kazushi Tachibana

Graduate School of Information Science, Nagoya University

Furo-cho, Chikusa-ku, Nagoya 464-8603, Japan

Abstract

The continued demand for micro-hole and slots is one of the driving forces behind this research. Coupled with this are successes gained in developing a single-point micro-punching unit. In this paper a multi-point micro punch and die were developed using tungsten and tool-steel as the punch material. The process of electric discharge machining (EDM) was used to produce the punch and die. The punches were machined from tungsten and tool-steel rods by wire electric discharge machining (WEDM) and the die holes were made using the punch as the electrode. The punch and die were set on a micro die-set and the holes were machined on a newly developed desktop EDM machine. The die-set was then transferred to a micro-press and the punching process was conducted. Experiments to produce 50-69 μm square micro-holes on 50 μm thick aluminum, 30 μm thick copper and 20 μm thick stainless steel foils were conducted and tungsten was chosen as the best material for making the punch. After the EDM process it was discovered that the surfaces of the punch were round and had to be flattened by reverse EDM. The effects of gold plating the micro-punches were examined as a means of reducing the discharge processing time and the rounding of the punch surface. With the aid of microscopes the holes produced were confirmed as clean and the sheared surfaces smooth. The holes produced by the gold plated punches were much cleaner than those produced by the non-gold plated punches. Consequently, the process of flattening after machining the die holes was eliminated and processing time was significantly reduced. The punch tools showed no signs of defect or deformation even after repeated punching.

Keywords: Multi-Point Punch; Gold Plating; Micro-Die Set; EDM; Clearance

1. Introduction*

The ongoing development in micro and high density products has led to continued research and development in the field of micro-hole technology. Some of the more popular research fields include EDM machining, vibration EDM machining [1], micro-punching using SiC fiber and laser micro-hole machining processes [2-4]. EDM and laser processes, which are currently the leading manufacturing methods of producing micro-holes and slots, are limited because of production cost, lengthy processing time and limitations with the materials that can be used in these processes. In addition, these methods have faced some amount of difficulties in applying them across various industries because they are not suited for mass production of micro-holes [2]. On the other hand, punching which is a deformation process has remained the most preferred method of mass production [5-6].

Although Chern and Wang [4] have developed a micro-forming and micro-punching system, alignment devices to ensure precise centering are needed because both punch and die were made separately. This can result in increases in production time and processing cost, and the possibility of miss alignment still remains a cause for concern. In this research the development of a multi-point punch and die set was examined. Tungsten and tool-steel were used as the material for making the punch and steel (S45C in JIS) for making the die. Tungsten was chosen as the preferred material because of its availability, its properties, mechanical as well as electrical, and its ability to punch various materials successfully. Table 1 shows the mechanical properties of tungsten. It is well documented that tungsten is widely used successfully across various manufacturing industries and in many researched and developed processes as micro rods to produce micro holes and for micro-hole drilling [7-8]. Not only is tungsten the most popular material of choice for micro rods and drills, but also in the other researches that have sought to develop micro punching systems[18 Chern and Chaung]. Lim, Lim and Kim [9] using electrochemical etching have developed a tungsten micro-punch for micro nozzles. Electrochemical etching is traditionally used to produce very sharp probes for atomic force microscopy or in the scanning of tunneling microscopy [10-11]. By using this process they were able to produce multiple punches cheaply and simultaneously. However, there is no evidence that this method can be employed to mechanical micro punching. Other researchers such as Joo, Rhim and Oh [12] developed a micro-hole mechanical punching process but

* Corresponding author. mabroomfield@yahoo.com

again expensive alignment devices were also needed with this process. In this case a machine vision system was developed and used to achieve accuracy within 1 µm. In addition to increased cost, addition time was also required to obtain proper alignment between punch and die, and misalignment is still possible.

Table I. Mechanical properties of tungsten.

Property	Value
Atomic weight	183.85 g/g atom
Density	19.25 g/cm^3
Melting Point	3410ºC
Ultimate strength	1510 MPa
Young's modulus	411 GPa

The multi-point punch is a development of the micro-punching system developed by Mori [2], one of the authors of this paper, using SiC fiber as the material for the punching tool. In that research it was possible to conquer some of the difficulties of alignment, however, continued research was necessary to make the system applicable to the industry. The decision to develop a multi-point punch was based on the success of developing a single point punch using similar methodologies, systems and processes in earlier experiments. This multi-point punching system will be better able to meet the ongoing demand for mass production of micro holes and slots in the various manufacturing sectors. Areas of demand include the miniaturization of electronic components for micro-systems technologies (MST) and micro-electromechanical systems (MEMS). Pins for IC-carriers, fasteners, micro-screws and contact springs, are some of the typical parts. Other areas of application include medical equipments, sensor technology, telecommunications and high-tech security systems [4], [13-14].

2. Experiment Method

2.1. Making of Punch

The multi-point micro-punch was made by wire EDM (WEDM) using the Mitsubishi DIAX FX10 EDM machine. Figure 1 shows the machining process of the punch. Before the punch points were machined one end of the round bar was machined by WEDM into a square prism of height 2.5 mm and square edges of 1.5 mm x 1.5 mm, as shown in Figure 1(a). Next, using the wire electrode the four point punch was machined in two stages as shown in Figure 1. In Figure 1(c to f), the center gutter was machined by the 200µm wire with a discharge gap of 20µm between the wire and inner punch walls. The wire electrode was then off-centered a distance of 600µm from the center and machined as shown in Figure 1(d).

The work was then rotated 90º and the processes of (c) and (d) were repeated. The work was then returned to its original position. This is the rough machining stage. The electrode wire was again off-centered by 80µm as shown in Figure 1(e), and machining done on the inner portions of the punch walls as shown. In Figure 1(f) finish machining of the outer sections of the punch points was done by off-centering the electrode wire by a distance of 370µm. The work was then rotated by 90ºand the processes of (e) and (f) repeated. The direction of machining is indicated by the arrows affixed to each drawing. Careful machining was done to ensure even distribution and parallelism between the punch-points. This is of extreme importance because the punch was also used as the electrode for making the die holes and unevenness would increase the discharge processing time, which leads to unequal material removal from the punch point surfaces.

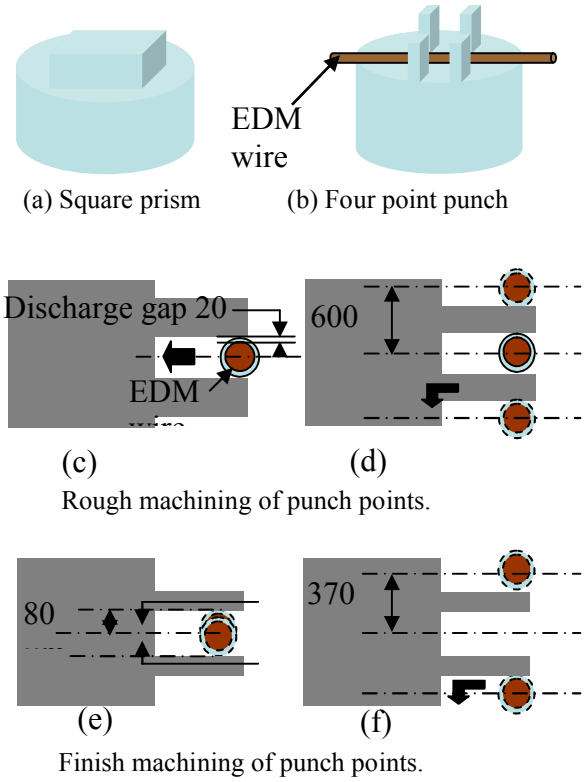

Figure 1. Punch making process.

2.2. Making of Die

Figure 2 shows the die making process. First a gutter of about 1.5 mm depth and 2 mm wide was cut in a plane machined from hard steel in the shape shown in (a). The tip of the gutter was machined by end mill to a width of 1 mm. The die surface was then polished to obtained a thickness of 20~30µm across the thinnest portion of the face where the hole was machined in (b), using # 2000 emery paper and 0.05µm aluminum powder. The die finished without making the hole was fastened to a micro die-set together with the prescribed micro punch as shown in Figure3. Next the micro die-set was placed into a specially made desktop EDM machine as shown in Figure 4. In this machine the process of Figure 2 (c) in which a die hole was made by electric discharge machining using the micro punch as the electrode was carried out. The holes were machined on the thinnest part of the die and the other portion provided support for the hole. A resistor-capacitor (R-C) circuit was used for the EDM process. This is because the R-C circuit works well for applications that require a low ampere-sparking output and is best for creating fine surface finishes or drilling small precision holes [15]. In order to prevent a large current from flowing through the circuit during short-circuit a large resistance

(resistor) was used. This reduced the short-circuit current to acceptable levels. Table 2 shows the discharge processing condition for machining the die holes. During the polishing process of the die surface, care was taken to ensure that it was polished evenly and flat to ensure simultaneous machining of the die holes and material removal from the punch points during the EDM process.

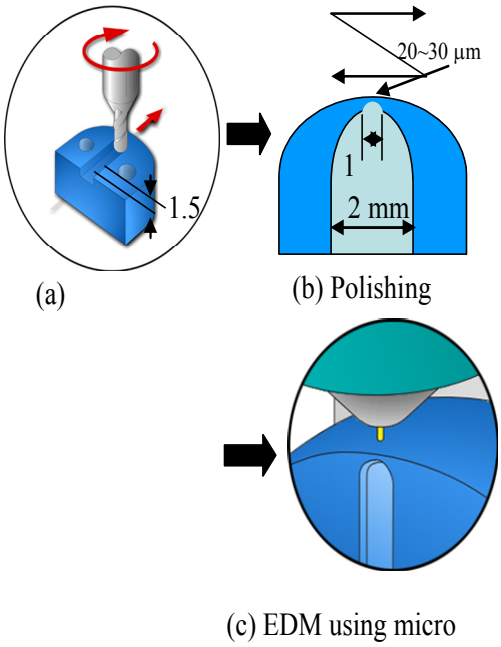

Figure 2. Die making process.

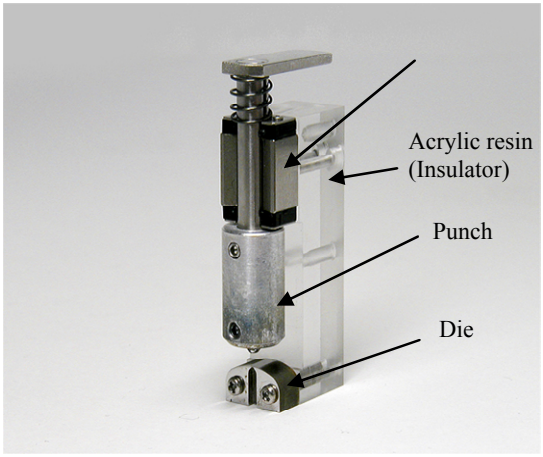

Figure 3. Micro-die set.

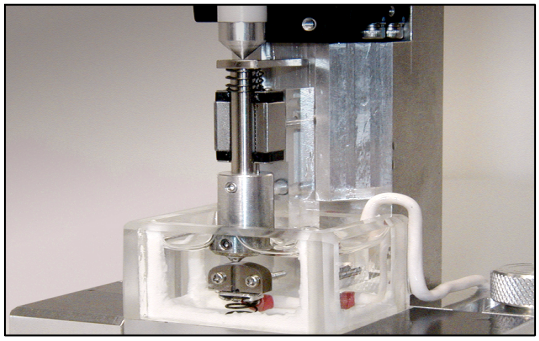

Figure 4. Desk top EDM machine.

Table 2. Electric discharge conditions.

Parameter	Quantity
Capacitance	1000~2000 pF
Voltage	40~45 V
Resistance	200 kΩ
Current	6.15 A
Electric discharge time	14 ~18 hr
Punch diameter	50µm (SK3)/64 µm(W)
Clearance	7.8-8.35µm

2.3. Flattening of Punch Surface

Flattening of the punch tool tip surface was done twice, before and after the EDM process of the die hole. Flattening before the EDM process was done to ensure that all four die holes were made simultaneously. This reduced the discharge processing time and the electrode consumption rate. The second flattening was necessary because after the die holes were machined the edges of the four-point punch appeared slightly round and uneven. However, the surfaces of the punch must be even, flat and acute to ensure that the punch surface satisfies the degree of demand of the cutting surface of a punch tool. If this was not done successful punching would not have been possible and the punch tool would have been adversely affected, as was observed on some occasion during the punching process. Also, if the punching surface of the tool was dull it would lead to unfavorable conditions, for example, long burr formation on the die side of the stock [16]. Flattening was done by reversing the polarity of the work and punch. A piece of 40µm thick copper and a piece of 20µm thick hard steel laminated foil was placed between the die surface and the punch. This increased the rate of material removal from the tool surface, while preventing material removal from the die surface. This process was carried out without separation of punch and die. Therefore the die set was designed so that this operation was possible without affecting the alignment of the punch and die unit. Figure 5 shows the micro-punch tool tip surface before and after the second flattening process.

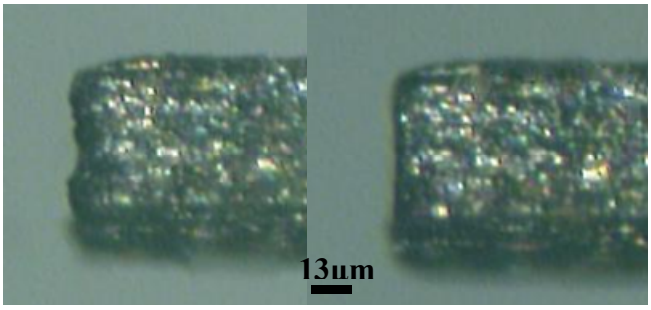

After EDM After flattening

Figure 5. Micrographs of punch before and after flattening.

2.4. Control and Measurement

The entire punching operation was controlled from a computer. The movement of the punch was controlled by the use of a piezoelectric actuator, connecting the micro punching system to the computer, and the movement of the material to be punched by stepping motor. The laminating

  - Volume 3, Number 2 (ISSN 1995-6665)

piezoelectric actuator used provided a maximum displacement of 68µm, and a generating force of 800 N was used for the primary drive. Figure 6 shows the linear relation between direct current voltage (V) and displacement (µm). The punching speed and movement were also controlled by the computer, which was connected to the piezo driver via D/A converter. Three highly precise miniature bearings were used for the guide of the punch. A microscope was used for positioning of the punch and observation of the punching operation.

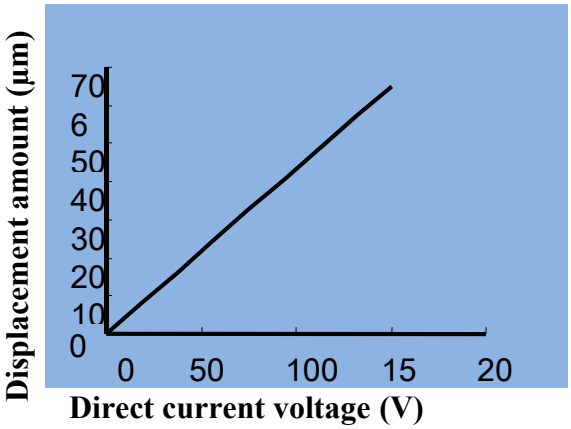

Figure 6. Displacement Vs. Direct Current Voltage.

The movement of the punch agreed with that of the piezoelectric actuator. The coefficient of conversion from piezoelectric driver voltage to punch stroke was 0.45µm /V and the punch movement signals were 10 V (punch stroke of 4.5µm) for a rough feed, and 1 V (0.45µm) for a fine feed. The punch speed was controlled by a change of the piezoelectric drive voltage, and varied from 6.4µm/sec to 3.8 mm/sec. The punching process was carried out at a punch speed of 6.4µm/sec without lubricant. The material feed was set and controlled by stepping motors for both the X and Y axis (movement of 0.1 mm). The material to be punched was secured by way of clamps attached to the X axis.

For this research a direct current voltage of 140V was used, which gave a vertical displacement of approximately 60µm of the punch. This was sufficient as the materials punched were 20µm to 50µm thick and the thickness of the section of the die where the hole was machined is between 20µm to 30µm thick. According to Tarkany [17] over entry of the punch creates excessive wear and can cause slug pulling. The farther a punch enters the more vacuum it creates at withdrawal. This vacuum can pull slugs. If a larger displacement is required this can be achieved by simply increasing the voltage on the piezo controller as illustrated in Figure 6.

2.5. Trial Punching

Punching was done using punches made from tool-steel (SK3) and tungsten (W). Figure 7 shows the average dimension of the tool steel and tungsten punches used in this experiment. Punching was conducted on 20µm and 30µm thick copper, 25µm and 50µm thick aluminum and 20µm thick stainless steel foils. For the tool-steel, punching of the copper and aluminum foils was successful but unsuccessful for the stainless steel foil. Repeated attempts to punch the stainless steel foil resulted in buckling of the punch tool. Figure 8 shows the punched holes of the copper and aluminum foils. After punching of over 500 heats on both the aluminum foils and copper foils, there were no noticeable signs of defects on the punch tool surface that indicated that the tool was breaking down, nor in the shape of the punched holes. From the micrographs, the holes produced appeared free of burrs, cracks and other forms of deformation that would denote poor hole production. The failure in punching the stainless steel foil implied that the result would be the same for materials of similar hardness.

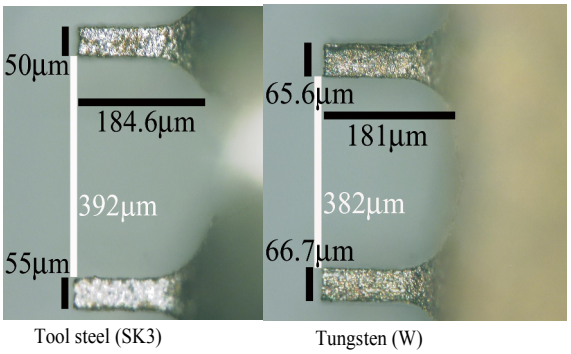

Figure 7. Dimension of punches.

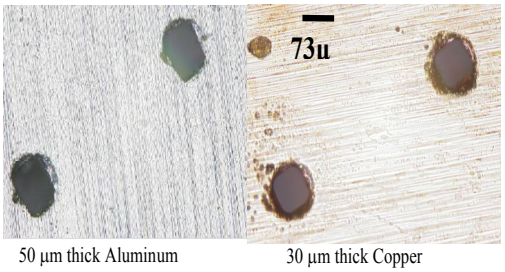

Figure 8. Holes punched by tool-steel punch

For the tungsten punch, trial punching was conducted on the same three materials, as well as on 20µm thick copper and 25µm thick aluminum foils. Except for the 25µm aluminum foil, and the 20µm thick copper foil the punching operation was successful. The holes produced were free of deformation, cracks and long burrs. Figure 9 shows the holes produced by the tungsten punch.

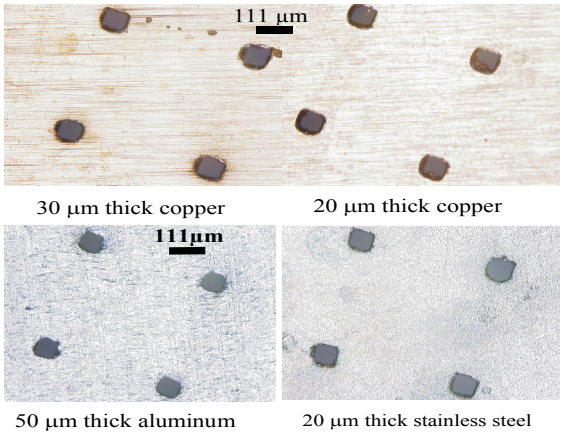

Figure 9. Micrographs of holes by tungsten punch.

The 25µm thick aluminum posed some difficulties during set up and punching. It was difficult to keep it flat on the die surface or from bending or warping. After the punching operation the holes were not clean. Burrs and other forms of deformation were visible on the sheared surfaces. This was believed to be as a result of incorrect clearance between the punch and die. Another reason was that the 25µm thick aluminum foil was too thin, and as of such movement might have occurred during the punching operation.

In addition the holes of the 20µm thick copper foil were not as clean as that of the 30µm copper foil. Small portion of the waste chips were not totally removed and some burrs could be seen on one or two of the holes. It was concluded that this was a result of using the same clearance as that used in punching the 30µm copper foil. This clearance was a little too large and resulted in the minor defects observed. This was not considered a major concern, as the necessary adjustments were made and the problem solved. A small vacuum pump was also attached to the die side of the hole to aid chip removal, as well as, to help keep the material flat on the die face. Figure 10 shows the holes produced on the 25µm thick aluminum foil.

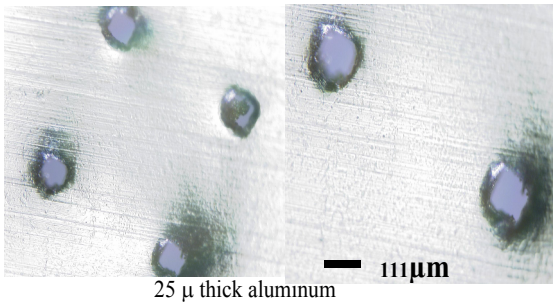

Figure 10. Micrograph of 25µm thick aluminum foil holes with too much clearance.

3. Results and Discussion

From the experiments it was concluded that different materials can be used as the punch tool, as long as they are conductive. However, there will be limitations as to the type of materials that can be punched, as in the case of the tool-steel punch. This was because of the hardness of the material. The tungsten punch was able to punch all the tested materials. After over 900 heats on the punches used for the aluminum foil, copper foil and the stainless steel foil, the punch showed no signs of cracks, wear or any other forms of deformation. Also the punched holes showed no signs of irregularities in shape or smoothness. Based on these results, tungsten has been confirmed as the best material for making the multi-point micro-punch. Although tungsten is usually a very difficult material to machine, using the processes of wire EDM negates such difficulties and makes the production of various shapes, length and sizes possible, depending on the capabilities of the WEDM machine. The effect of clearance and gold plating the punch tools were extremely important to the success and effectiveness of the punch tool and the punching operation and as such, are discussed separately below.

3.1. The Effects of Clearance

During the trial punching it was discovered that the normal practice of using 5 percentage of stock thickness per side for the clearance as a standard was not applicable. This was due to the size of the parts. Near optimum clearance was necessary to produce holes that were free from long burrs and other forms of deformations. With insufficient clearance the defect known as "secondary shear" was produced. This is when the fracture of the punch cutting edge misses the fracture of the die cutting edge. This effect was observed after punching the 25 µm aluminum foil shown in Figure 10. Although the punching was successful, secondary shearing occurred, evident in the formation of long burrs seen on the sheared surfaces of the holes. For the stainless steel, insufficient clearance resulted in "spring back". In this case the punched holes became smaller and gripped to the punch tool, often causing bending and breaking of the tool. Additional problems observed includes, increase in desired punching pressure and large stripping force which caused part distortion, extra punch wear and reduction in tool life. These defects decreased as the percentage clearance increases towards optimum clearance. In cases where the clearance was too large, extreme plastic deformation occurred [18]. Increase in burr formation and burr height and excess roll-in at the punch side of the holes were also noticed. Gripping of the punch tool to the material was also observed with excessive clearance, which was a result of tapered holes formed during the punching process.

It is therefore imperative for effective punching to obtain clearance that is near optimum, as too small or too large a clearance will result in undesirable deformations and conditions. With the correct clearance the angle of fracture permits a clean break below the cut band because the upper and lower fractures extend toward one another. As such, correct or proper clearance is one which does not cause secondary shear and result in only a minimum degree of plastic deformation [18].

The desired clearance was achieved by varying the EDM processing parameters during the machining of the die holes, depending on the material thickness and the kind of material. For the copper and aluminum foils a capacitance of 1000 pF was used and a capacitance of 2000 pF for the stainless steel foil. This provided the clearances necessary to punch quality holes in the various materials. Based on the results of the trial punching, it was concluded that a clearance of 18% to 21% is best for the 20µm thick stainless steel foil, 9% to 14% for the 30µm copper foil and 7% to 9% for the 50µm thick aluminum foil. Even with optimum clearance, burr formation can still occur, especially when punching thinner and softer materials. The small vacuum pump that was added to the punching unit help ensured continuous punching without the problem of unwanted chips. It also helped reduced burr formation and with preventing the material from sticking to the punch tool after the punching process was completed. The experiments also confirmed that clearance between punch and die also depends on the tensile strength and yield strength of the material, and on material thickness. As tensile strength, and yield strength increase the required clearance increases. In the case of material thickness, required clearance increases as thickness increases.

  - Volume 3, Number 2 (ISSN 1995-6665)

3.2. Effects of Gold Plating

Tungsten is one of the best and most used material for electrodes employed in the production of micro holes by micro-EDM, micro-drilling or other forms of micro-hole or micro-slot manufacturing. This is because of the low machining energy involved when compared with other processes. However, one of the major disadvantages is the low material removal rate, which translates into lengthy processing time. In other researches ultrasonic machining and vibration assisted EDM machining have been investigated and used to improve the efficiency of the machining process [1, 19].

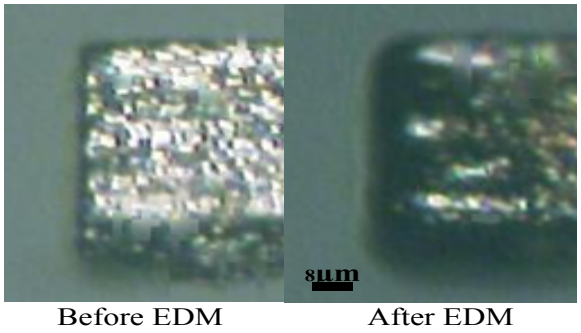

Figure 11. Gold plated punch before and after EDM process.

In this research the problem of lengthy discharge process time led to an additional disadvantage. Due to the lengthy discharge process the surface of the punch became rounded and uneven. This made punching almost impossible, as the punch tool surface must be flat and acute for effective punching. In order for punching to be possible the surface of the punch was flattened by reverse EDM, as explained earlier. Although the process of flattening the punch tool after the EDM process of the die hole resulted in successful punching the problem of lengthy processing time still remained and the process was made longer by the additional reverse EDM process. The effect of gold plating was examined based on the success in a previous research [2]. A thin gold film of 20 nanometer was added to the surfaces of the punch-points of both the tool-steel punch and the tungsten punch using the process of vapor evaporation. The process of gold plating was done by a gold plating company. The punches were then used to machine the die holes and then as the punch for the test materials, using the same parameters as before. The use of the gold plated punches resulted in a drastic reduction in the discharge processing time and the process of flattening after the EDM process of the die holes was no longer necessary because the problem of rounding of punch-points and unevenness of punch surfaces no longer existed. Figure 11 shows the surface of the punch before and after the EDM process of the die holes. In addition to the reduction in discharge processing time and punch surface roughness, the sheared surfaces of the holes produced by the gold plated punch were much cleaner. They were free from burrs and the sheared surfaces appeared to be much smoother and in general, of better quality than the holes produced with the non-gold plated punches. Figure 12 shows the holes produced using the gold plated tungsten punch.

4. Conclusion

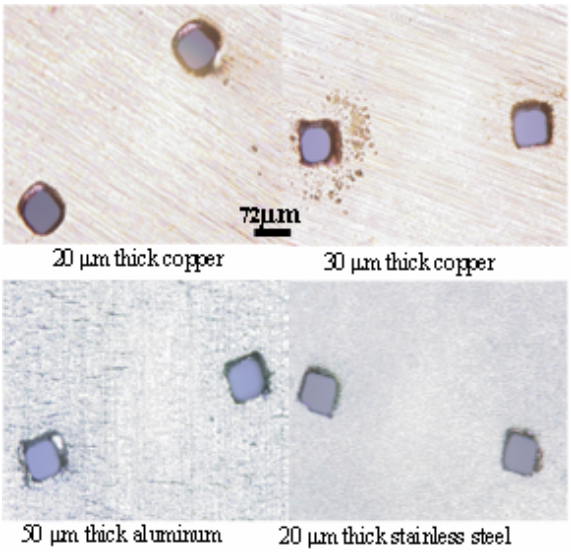

Figure 12. Micrographs of holes punched by gold plated tungsten punch.

In this paper a multi-point punch and die set was developed using the processes of EDM. The punch-points were gold plated in order to reduce the discharge processing time, surface roughness and the rounding of the punch-points during the machining of the die holes. The results obtained from the trial punching are summarized as follows:

1. Tungsten (W) is a good material for making the punch tool because it can be used effectively as the electrode for the die holes and as the punch tool for all three tested materials.
2. Remarkable reduction in the die holes discharge processing time, surface roughness of punch- points and rounding of punch surface was achieved by gold plating the punch.
3. The problem of proper punch and die alignment is eliminated with the use of the die-set.
4. The punching of various materials (copper, stainless steel and aluminum) was possible without damages to the punch cutting surfaces or changes in the dimensions of the punched holes.
5. It was demonstrated that movement of the work piece during the punching operation, flatness of the die and punch surface could affect the quality of the punched holes. Therefore, care must be taken to ensure that this movement is eliminated and flatness of both surfaces is achieved.
6. It was confirmed that if the diameter of the punch, and the material type and thickness changes, the processing condition for the EDM process of the die hole must also be changed to maintain proper clearance between the punch and die holes.
7. Achieving near optimum clearance between punch and die is essential to successful punching. This is possible by controlling the processing parameters during the EDM process of the die holes.

The results obtained so far by the micro punching system using tungsten and other materials for making the multi-point micro-punch, are evidence that this system can

be successfully applied to various manufacturing industries to mass produce micro-holes.

References

[1] T. G. Endo, T. Tsujimoto, K. Mitsui, "Study of vibration-assisted micro-EDM-The effect of vibration on machining time and stability of discharge". Precision Engineering, Vol. 32, No. 4, 2008, 269-277.

[2] T. Mori, "Development of ultra-fine piercing by SiC fiber punch". Transaction of ASME Journal of Manufacturing Science and Engineering, Vol. 126, 2004, 659-665.

[3] M. Fujino, M. Yamamoto, T. Masuzawa, "Micro-punching system as an application of WEDG". Institute of Industrial Science, University, Tokyo, SEISAN-KENKYU, Vol. 39, 1987, 277-280 (in Japanese).

[4] G. Chern, S. Wang, "Punching of noncircular micro-holes and development of micro-forming". Precision Engineering, Vol. 3, 2007, 210-217.

[5] Schonberger RJ. World class manufacturing: The Next Decade. New York: The Free Press; 1996.

[6] Martellucci S, Chester AN, Scheggi AM. Laser applications for mechanical industry, NATO ASI Series. Boston and London: Kluwer Academic; 1993.

[7] T. Masuzawa, HK. Tonshoff, "Three-dimensional micromachining by machine tools". Ann CIRP 46. 1997, 621-628.

[8] M. Yamazaki, T. Suzuki, N. Mori, M. Kunieda, "EDM of micro-rods by self-drilled holes". Journal of Materials Processing Technology, Vol. 149, 2004, 134-138.

[9] H. Lim, Y. Lim, S. Kim, "Fabrication of tungsten micro-punch for micro-nozzles". Review of Scientific Instruments, Vol. 72, 2001, Number 8.

[10] P.J. Bryant, H.S. Kim, Y.C. Zheng, R. Yang, "Technique for shaping scanning tunneling microscope tips". Review of Scientific Instrument, Vol. 58, 1987, 1115.

[11] M. Fotino, "Tip sharpening by normal and reverse electrochemical". Review of Scientific Instrument, Vol. 64, 1993, 159.

[12] B. Joo, S. Rhim, S. Oh, "Micro-hole fabrication by mechanical punching process". Journal of Material Processing Technology, Vol. 170, 2005, 593-601.

[13] F. Vollertsen, Z. Hu, H. S. Niehoff, C. Theiler, "State of the art in micro forming and investigations into micro deep drawing". Journal of Materials Processing Technology, Vol. 151, 2004, 70-79.

[14] K. Hanada, L. Zhang, T. Sano, "Fabrication of diamond dies for micro forming". Diamond Related Materials, Vol. 12, 2003, 757-761.

[15] Jameson EC. Electrical discharge machining. Dearborn, Michigan: Society of Manufacturing Engineers; 2001.

[16] Wilson WW, Harvey PD, Gump Jr CB. Die design handbook. 2nd ed. New York: McGraw-Hill Book Company; 1965.

[17] N. Tarkany, "Improving perforated die performance: The effects of stress, clearance, material". Stamping Journal, 2003. Visit Also: http://www.thefabricator.com/ToolandDie/ToolandDie_Article.cfm?ID=549.

[18] Eary DF, Reed EA. Techniques of pressworking sheet metal. Englewood Cliffs New Jersey: Prentice-Hall, INC; 1958, 10-33.

[19] G. Chern, Y. Chaung, "Study on vibration-EDM and mass punching of micro-holes". Journal of Materials Processing Technology, Vol. 180, 2006, 151-160.

JJMIE

Volume 3, Number 2, June. 2009
ISSN 1995-6665
Pages 97 - 104

Jordan Journal of Mechanical and Industrial Engineering

Strain-Concentration Factor of Cylindrical Bars with Double Circumferential U-Notches under Static Tension

Hitham M. Tlilan*, Ali M. Jawarneh, Ahmad S. Al-Shyyab

Department of Mechanical Engineering, Faculty of Engineering, The Hashemite University
P.O. Box 150459, Zarqa 13115, Jordan

Abstract

The interference effect on the new strain concentration factor (SNCF), which has been defined under triaxial stress state; is studied using the Finite Element Method (FEM).To this end, cylindrical bars with double circumferentially U-notches under static tension are employed. he new SNCF is constant in the elastic deformation and the range of this constant value increases with increasing notch pitch (lo) in the range 0.0 <lo≤ 0.5 mm, then it decreases with increasing lo, and reaches a value nearly equal to that of the single circumferential U-notch. This becomes prominent with decreasing notch radius. As plastic deformation develops from the notch root; the new SNCF increases from its elastic value to a maximum value. On further plastic deformation, the new SNCF decreases with plastic deformation. The current results indicate that the notch pitch, where the interference effect is more pronounced on the new SNCF, is $0.0 \le l_o \le 5$ mm.

Keywords: Finite Element Method; Interference Effect, Notch; Tension; Strain-Concentration Factor

Nomenclature

A	net-section area
d_o	initial net-section diameter
D_o	initial gross diameter
E	Young's modulus
K_ε^{con}	conventional strain-concentration factor
K_ε^{new}	new strain-concentration factor
P	tensile load
P_Y	tensile load at yielding at the notch root
r	current distance from the center of the net-section ($0 \le r \le r_n$)
r_n	current net-section radius = $d/2$
s	$= r/r_n$ ($0 \le s \le 1.0$)
$2\ln(d_o / d)$	deformation parameter
$[2\ln(d_o / d)]_Y$	deformation parameter at yielding at notch root
η	the ratio of deformation parameter to that at yielding at the notch root $= \dfrac{2\ln(d_o / d)}{[2\ln(d_o / d)]_Y}$
ε_z	axial strain
$(\varepsilon_z)_{av}^{con}$	conventional average axial strain
$(\varepsilon_z)_{av}^{new}$	new average axial strain
$(\varepsilon_z)_{max}$	maximum axial strain
ν	Poisson's ratio
ρ_o	initial notch radius
σ_{eq}	equivalent stress
equivalent stress	$=\left\{(\sigma_z-\sigma_\theta)^2+(\sigma_\theta-\sigma_r)^2+(\sigma_r-\sigma_z)^2\right\}^{1/2}/\sqrt{2}$
$(\sigma_{eq})_{max}$	equivalent stress at the notch root
σ_r , σ_z , σ_θ	radial , axial and tangential stresses
σ_Y	yield stress
$(\sigma_z)_{av}$	average axial stress at the net section = P/A
$(\sigma_z)_{max}$	axial stress at the notch root in elastic deformation
$(\sigma_\theta)_{max}$	tangential stress at the notch root in elastic deformation

* Corresponding author. hitham@hu.edu.jo.

  - Volume 3, Number 2 (ISSN 1995-6665)

Abbreviations

SNCF	strain concentration factor
SSCF	stress concentration factor

1. Introduction

Stress and strain concentrations in any type of loading arise when uniformity of geometry is disrupted. Particularly, geometrical irregularities such as notches, grooves, holes, or defects are acting as local stress and strain raisers. They alter the lines of the principal stress; and bring about the stress and strain concentrations at the notch tip. Moreover, biaxial or triaxial stress state is produced at the net section even if the single loading, like axial tension, is applied to the notched bars. This single loading generates the uniaxial stress state in the unnotched part with the gross section. It should be noted that the net section is subjected simultaneously to the stress and strain concentrations and the multiaxial stress state.

Many numerical analyses and theoretical studies have been conducted to obtain the elastic stress-concentration factor (SSCF); the results have been published and used for engineering design [1- 6]. The Neuber's approximate analytical solutions are the main source, concerning the notch depth effect on the elastic SSCF [3-7]. Neuber's rule predicts that the plastic SNCF increases, and the plastic SSCF decreases from their elastic values as plastic deformation develops from the notch root [7]. Many experimental or analytical studies under static axial tension have confirmed this prediction [7-13]. These results indicate that the SNCF is more important than the SSCF [14-15]. This is because the plastic SNCF maintains a value much greater than unity while the plastic SSCF decreases towards unity.

There have been many studies used to calculate the stress and strain at the notch root under static and cyclic tensile loading using Neuber's rule [13, 16-21], Glinka's method [18-19, 21-22], and linear rule [13, 17, 19, 23]. The predicted values have been compared with finite element and experimental ones. The results of these comparisons indicate that there is no rule which can accurately predict the magnitude of the axial strain at the notch root. Particularly, in notched rectangular bars, the accuracy of the prediction decreases with increasing thickness. This is because the conventional strain-concentration factor (= maximum axial strain/average or nominal strain) is defined under uniaxial stress state while axial strain at the notch root occurs under triaxial stress state [14, 15]. Strain-concentration factor should thus be defined under triaxial stress state at the net section [14-15].

A new SNCF has been proposed under the axial tension [14]. This new SNCF has been defined under triaxial stress state at the net section. This has enabled new SNCF to provide reasonable values consistent with the concave distributions of the axial strain on the net section [14-15].

Moreover, this new SNCF has removed the contradiction in conventional SNCF having values less than unity in spite of the concave distributions of the axial strain under elastic-plastic deformation. The nominal strain of the conventional SNCF, as described above, has been defined under the uniaxial stress state. The uniaxial stress state is completely different from the stress state at the net section, namely, the triaxial stress state [14-15]. This causes the above contradiction of the conventional SNCF. This means that the SNCF for any type of loading must therefore be defined under the triaxial stress state at the net section. This is because the axial strain at the notch root occurs under the triaxial stress state.

The effect of notch depth on the SNCF and SSCF under static tension and under pure bending has been studied by [15,24,25-26].

The specimens employed are circumferentially U-notch cylindrical bars for static tension and rectangular bars with single-edge U-notch for pure bending. The results indicate that the new SNCF is more reasonable than the conventional SNCF and SSCF. Therefore, this newly defined SNCF must be applied to different types of notches or geometries and different types of loading.

Some studies examined the interference effect on the elastic SSCF of the flat bars with double U- or semicircular notches under tension. The obtained relations between the elastic SSCF and the notch pitch have been published and used for engineering design [3]. These studies show that SSCF subjected to interference effect is less than the SSCF of a single notch. Few studies have been carried out on the interference effect on the elastic SSCF of cylindrical bars with double U- or semicircular notches under tension. Moreover, only two studies have been performed on the interference effect on strength such as yield point load, ultimate tensile strength, and deformation properties of notched bars under tension [27-28]. In these studies, the interference effect has also been discussed on the elastic SSCF of cylindrical bars with double U-notches under tension.

Unfortunately, the interference effect on elastic and elastic-plastic new SNCF has not been evaluated. In this paper, the cylindrical bar double circumferential U-notches is employed to study the interference effect on the elastic-plastic new SNCF.

2. Strain-Concentration Factor under Static Tension

For tensile loading, the new strain-concentration factor (SNCF) has been defined as the ratio of the maximum axial strain at the notch root $(\varepsilon_z)_{max}$ to the new average axial or new nominal strain $(\varepsilon_z)_{av}^{new}$[14] .

$$K_{\varepsilon}^{new} = \frac{(\varepsilon_z)_{max}}{(\varepsilon_z)_{av}^{new}} \quad (1)$$

Since the maximum axial strain at the notch root is independent of definition, then the new SNCF is introduced by a new definition of the average axial strain $(\varepsilon_z)_{av}^{new}$. For circumferentially notched cylindrical bars $(\varepsilon_z)_{av}^{new}$ is defined as follows [14]:

$$(\varepsilon_z)_{av}^{new} = \frac{1}{\pi r_n^2}\int_0^{r_n} \varepsilon_z(r)\, 2\pi\, r\, dr = 2\int_0^1 \varepsilon_z(s)\, s\, ds \quad (2)$$

where $s = r/r_n$. In the elastic level of deformation, $(\varepsilon_z)_{av}^{new}$ can be transformed into the following equation:

$$\begin{aligned}(\varepsilon z)_{av}^{new} &= \frac{1}{\pi r_n^2}\int_0^{r_n}\left[\frac{\sigma_z}{E}-\frac{\nu}{E}(\sigma_\theta+\sigma_r)\right]2\pi\, r\, dr \\ &= \frac{1}{E}\cdot\frac{1}{\pi r_n^2}\int_0^{r_n}\sigma_z\, 2\pi\, r\, dr-\frac{\nu}{E}\cdot\frac{1}{\pi r_n^2}\int_0^{r_n}(\sigma_\theta+\sigma_r)\,2\pi\, r\, dr \\ &= \frac{1}{E}\cdot\frac{P}{\pi r_n^2}-\frac{\nu}{E}\cdot\frac{1}{\pi r_n^2}\int_0^{r_n}(\sigma_\theta+\sigma_r)\,2\pi\, r\, dr \\ &= \frac{(\sigma z)_{av}}{E}-\frac{\nu}{E}\cdot\frac{1}{\pi r_n^2}\int_0^{r_n}(\sigma_\theta+\sigma_r)\,2\pi\, r\, dr\end{aligned} \quad (3)$$

Where E and ν are the Young's modulus and Poisson's ratio, respectively. Equation (3) can be rewritten as follows:

$$(\varepsilon_z)_{av}^{new} = \frac{(\sigma_z)_{av}}{E}-\frac{2\nu}{E}\int_0^1\{\sigma_\theta(s)+\sigma_r(s)\}\, s\, ds \quad (4)$$

This equation indicates that $(\varepsilon_z)_{av}^{new}$ is defined under the triaxial stress state at the net section.

It should be noted that $(\varepsilon_z)_{av}^{new}$, given by Eq. (2), is defined under the triaxial stress state also in plastically deformed area at the net section.

This is because of the fact that plastic component of the axial strain is directly related to the triaxial stress state, as is indicated by the theory of plasticity. Since the plastic deformation develops from the notch root; i.e. $\sigma_{eq} > \sigma_Y$, the newly defined average axial strain has been calculated using the incremental or flow theory, which relates the stresses to the plastic strain increments. In the plastic deformation, the strains in general are not uniquely determined by the stresses but depend on the entire history of loading. The definition under the triaxial stress state gives reasonable results consistent with the concave distribution of the axial strain at any deformation level [14-15, 24-25].

The conventional SNCF under static tension has been defined as follows

$$K_\varepsilon^{con} = \frac{(\varepsilon_z)_{max}}{(\varepsilon_z)_{av}^{con}} \quad (5)$$

Where $(\varepsilon_z)_{max}$ is the maximum axial strain at the notch root and $(\varepsilon_z)_{av}^{con}$ is the conventional average axial strain. This conventional SNCF has been defined under uniaxial stress state at the net section. This is because the conventional average axial strain $(\varepsilon_z)_{av}^{con}$ has been defined under uniaxial stress state [13-14]. In elastic deformation, the axial stress σ_z at the notch root $(\sigma_z)_{max}$ is much greater than $(\sigma_z)_{av}$, and the equivalent stress at the notch root $(\sigma_{eq})_{max}$ is a little lower than $(\sigma_z)_{max}$ under the biaxial tensile stress state. This indicates that the small plastic deformation occurs around the notch root even in the range $(\sigma_z)_{av} \le \sigma_Y$ when $(\sigma_z)_{av}$ approaches σ_Y. Even in this range $(\varepsilon_z)_{av}^{con}$ is given by

$$(\varepsilon_z)_{av}^{con} = \frac{(\sigma_z)_{av}}{E} \quad (6)$$

This equation indicates that the conventional definition has neglected the effect of tangential σ_θ and radial stresses σ_r. On further development of plastic deformation, i.e. in the range $(\sigma_z)_{av} > \sigma_Y$, $(\varepsilon_z)_{av}^{con}$ is determined using the uniaxial true stress–total strain curve $\sigma = f(\varepsilon)$. The reason for using this curve is that $(\varepsilon_z)_{av}^{con}$ is defined under the uniaxial stress state, and $(\sigma_z)_{av}$ is based on the instantaneous area of the net section. The conventional average axial strain is therefore given by

$$(\varepsilon_z)_{av}^{con} = f^{-1}\{(\sigma_z)_{av}\} \quad (7)$$

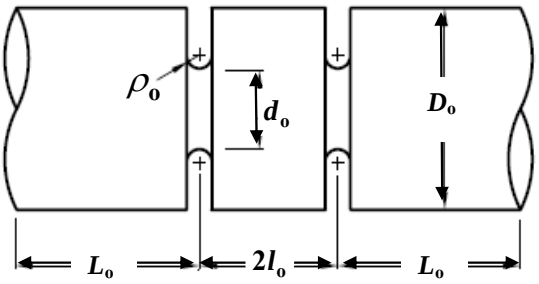

Figure 1. Specimen geometries.

3. Specimen Geometries

The employed cylindrical bar with double circumferential U-notches is shown in Fig.1. The net-section diameter d_o of 3.34 mm, and the gross diameter D_o of 16.7 mm were selected to give the net-to-gross diameter ratio d_o/D_o of 0.2. Figure 1 shows that the specimen length is expressed as $(2L_o+2l_o)$, where $2L_o$ is the unnotched length from the notch center to the loaded end, and $2l_o$ is the notch pitch or the distance between the centers of the two notches. The unnotched length is held constant, while the half notch pitch l_o is varied from 0.0 to 25 mm to examine the interference effect of the double circumferential U-notches. It should be noted that the notch pitch l_o= 0.0 mm represents the cylindrical bar with a circumferential U-notch, perpendicular to the axial direction. Two notch radii ρ_o of 0.5 and 2.0 mm are employed to vary the notch sharpness $d_o/2\rho_o$.

4. Finite Element Mesh for Double Circumferential U-Notches

Figure 2 shows a finite element mesh of one quarter of a notched specimen with double circumferential U-notches. An eight-node axisymmetric isoparametric quadrilateral ring element, with biquadratic interpolation and full integration - type 28 in MARC classifications, is

employed. This type of element uses the nine integration points, i.e. Gauss points.

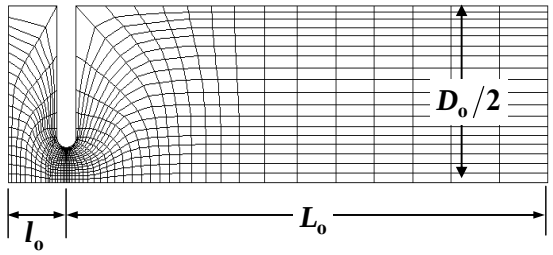

Figure 2. Finite element model.

The FEM calculations were performed under the axisymmetric deformation. This deformation was given under the condition that the axial displacement at the gross section in the center of the notch pitch and the radial displacement at the central axis are zero. The increments of the axial displacement were applied at the right end of the unnotched part. The magnitude of the increment was small enough to provide an elastic solution for the first few increments in each notched specimen.

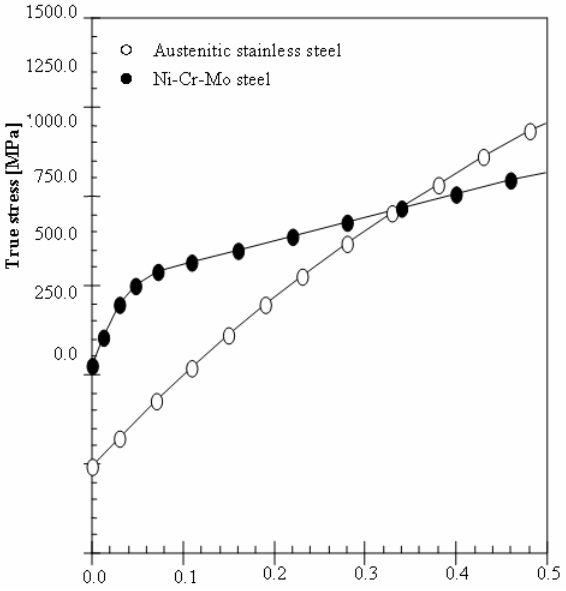

Figure 3. True stress – plastic strain curves.

All of the current calculations were carried out using MSC. Marc software. In elastic deformation, the stress-strain relationship is linear while it is nonlinear in plastic deformation. The program was developed on the basis of displacement method. After the start of plastic deformation, the nonlinear relations are used, and hence equations should be solved incrementally. Iterations are performed within each increment to satisfy the equilibrium and convergence at the end of each stage. In order to ensure the accuracy of the results and their independence with respect to the number of nodes used in the discretization process, several meshes were tested. A grid independent solution study was made by performing the simulations for different meshes.

5. Material Properties

The materials employed are an Austenitic stainless steel and an Ni-Cr-Mo steel. Young's modulus E, Poisson's ratio ν and the tensile yield stress σ_Y are listed in Table 1. The true stress-plastic strain curves were obtained from tension tests. In order to express the stress-strain curve accurately, the obtained relation was divided into a few ranges of plastic strain, and in each range the following fifth-degree polynomial was fitted:

$$\sigma = C_o + C_1\varepsilon_p + C_2\varepsilon_p^2 + C_3\varepsilon_p^3 + C_4\varepsilon_p^4 + C_5\varepsilon_p^5 \quad (8)$$

The values of these coefficients in the plastic strain ranges used are also listed in Table 1. Figure 3 shows the true stress-plastic strain curves given by these polynomials.

6. The Deformation Parameter $2\ln(d_o/d)$

The measure of deformation is required when comparison is made among distributions of stress and strain between different deformation levels, different materials, and different notch geometries, i.e. pitches. The degree of deformation $2\ln(d_o/d)$ of notched cylindrical specimens can be expressed by the magnitude of the deformation at the net section. This is because fracture always occurs at the net section. This measure of deformation is obtained from the assumptions of the uniform deformation in the immediate vicinity of the net section and the volume constancy in this part. The assumption of the volume constancy can be applied only to plastic strain.

The elastic strain component of the axial strain is thus assumed to be negligible compared t the plastic strain component in the immediate vicinity of the net section. This means that the element $A_o \times \delta l_o$ deforms to the element $A \times \delta l$ under the conditions of the volume constancy and the uniaxial stress state, where A_o, A, δl_o, δl are the initial and current areas and the initial and current lengths of the element. The volume constancy, $A_o \times \delta l_o = A \times \delta l$, gives the engineering axial strain of this element e_z

$$e_z + 1 = \frac{\delta l}{\delta l_o} = \frac{A_o}{A} = (d_o/d)^2 \quad (9)$$

The logarithmic axial strain is thus given by

$$\varepsilon_t = \ln(e_z + 1) = \ln(d_o/d)^2 = 2\ln(d_o/d) \quad (10)$$

This obtained variable $2\ln(d_o/d)$ can be a measure of the deformation parameter at the deformation levels where the elastic strain component is much less than the plastic one. It also plays the role of an average axial strain because a uniform deformation or uniaxial stress state is assumed. Moreover, the ratio d_o / d represents the magnitude of the decrease in the net diameter under tensile deformation at any deformation level. This means that $2\ln(d_o/d)$ can be used as a measure of deformation from infinitesimal to large deformation [14-15].

Table 1. Mechanical properties and polynomial coefficient.

Material ν, E [GPa], σ_Y [MPa]	Plastic strain range	C_o	C_1	C_2	C_3	C_4	C_5
Austenitic stainless steel 0.30, 206, 245.9	$\varepsilon_p \le 0.2$	2.459×10^2	4.389×10^3	-3.265×10^4	2.402×10^5	-8.899×10^5	1.258×10^6
	$0.2< \varepsilon_p \le 0.5$	3.789×10^2	1.535×10^3	1.173×10^3	-1.874×10^3	0.0	0.0
Ni-Cr-Mo steel 0.30, 206, 525	$\varepsilon_p \le 0.1$	5.250×10^2	7.644×10^3	-7.377×10^4	2.596×10^5	0.0	0.0
	$0.1<\varepsilon_p$	7.426×10^2	6.945×10^2	-8.143×10	0.0	0.0	0.0

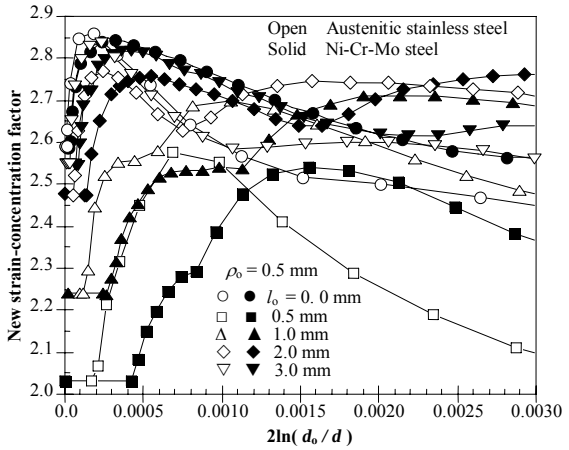

Figure 4. Variations of the new SNCF with deformation for ρ_o = 0.5 mm

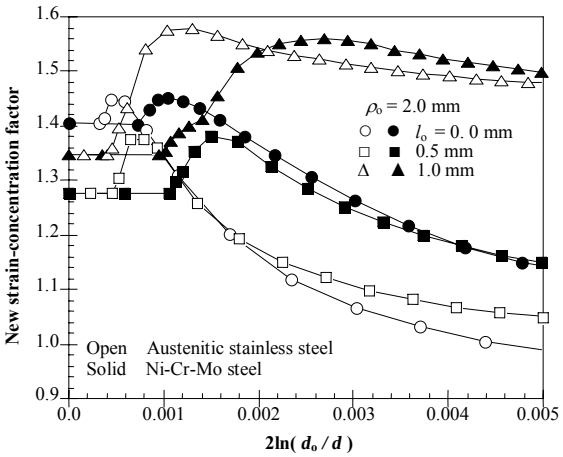

Figure 5. Variations of the new SNCF with deformation for ρ_o = 2.0 mm.

7. Interference Effect on the New SNCF(K_ε^{new})

The variations in the new SNCF K_ε^{new} with $2\ln(d_o/d)$ are given in Figures 4 and 5. The new SNCF is constant inelastic deformation, and the range of $2\ln(d_o/d)$ for this constant value increases with increasing notch radius. It also increases with increasing notch pitch up to $l_o \approx 0.5$ mm. On further increase in the notch pitch, this range decreases and becomes nearly the same as that of the single circumferential U-notch. As plastic deformation develops from the notch root, the new SNCF increases from its elastic value to its maximum, and then decreases on further plastic deformation. Figures 6(a) and (b) show the relation of the elastic K_ε^{new} with half notch pitch l_o and with the ratio (l_o/ L_o). The elastic K_ε^{new} rapidly decreases from its value at l_o = 0.0 mm and reaches its minimum at $l_o \approx 0.5$ mm. On further increase in l_o, the elastic K_ε^{new} gradually increases and finally reaches the value of the circumferential U-notch (l_o = 0.0 mm) at l_o = 5 mm and 2 mm for ρ_o= 0.5 and 2 mm, respectively. Beyond this value of l_o, the elastic K_ε^{new} is nearly constant up to l_o = 25 mm, the maximum half notch pitch in the FEM calculations. The elastic K_ε^{new} in the range $5 \le l_o \le 25$ mm are nearly equal to the elastic K_ε^{new} of the circumferential U-notch. This indicates that the interference effect on the elastic K_ε^{new} is extremely strong in a small range of l_o and nearly vanishes beyond $l_o \approx 5.0$ mm. It should be noted that the same results have been obtained for ρ_o= 2.0mm. However, the interference effects disappears in the range l_o >2.0 mm.

Figure 7 shows the variation of the new average axial strain or new nominal strain $(\varepsilon_z)_{av}^{new}$ and the maximum axial strain $(\varepsilon_z)_{max}$ with deformation. It is clear that the values of $(\varepsilon_z)_{av}^{new}$ and $(\varepsilon_z)_{max}$ for at any level of deformation for l_o = 0.5 mm are less than that for l_o > 0.5mm. Figures 8 and 9 show that the axial strain has concave distribution on the net section for all notch pitches employed. Particularly, the rate of the increase in the axial strain through the net section increases with increasing notch pitch. The axial strain value at the notch root; i.e. the maximum axial strain, increases from it minimum value for l_o = 0.5 mm and reaches maximum value for l_o = 0.0 mm. This indicates that the severe interference effect is more pronounced in the range $0.0 < l_o \le 5.0$ mm.

The tensile load P is calculated using the following equation:

$$P = \int_A \sigma_z \, dA = (\sigma_z)_{av} \, A \tag{11}$$

Where A (= π/4 d^2) is the current net-section area. Therefore, the tensile load P can be related to the deformation parameter $2\ln(d_o/d)$ by

$$P = (\sigma_z)_{av} \, A = \frac{\pi}{4} \frac{d_o^2}{e^{2ln(d_o/d)}} (\sigma_z)_{av} \tag{12}$$

The variation in the tensile load with deformation is shown in Fig. 10. The current results indicate that the rates of increase in the tensile increase with increasing notch pitch. This indicates that the severity of the notch increases with increasing notch pitch. As a result, the single circumferential notch gives more strain concentration than the double circumferential U-notches, especially when the notch pitch is less than 5 mm. This essentially attributed to rate and direction of development of deformation from the notch root. That is, when the double notches are closed to each other, the deformation spreads in inclined direction from the notch root to the pitch center, as shown in Figures

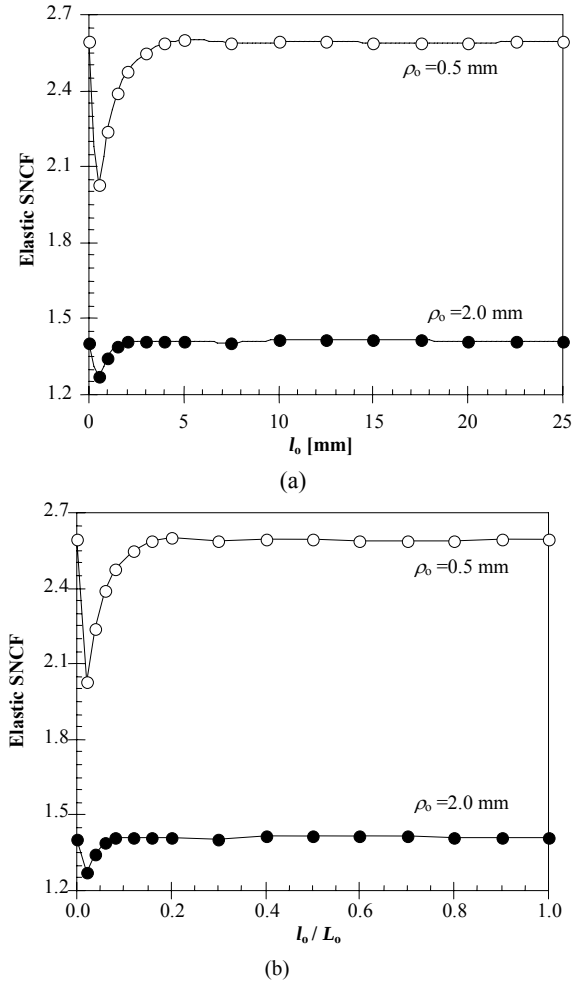

Figure 6. (**a**) .Variations in elastic new SNCF half notch pitch l_o, **(b)**. Variations in elastic new SNCF with the ratio (l_o/L_o).

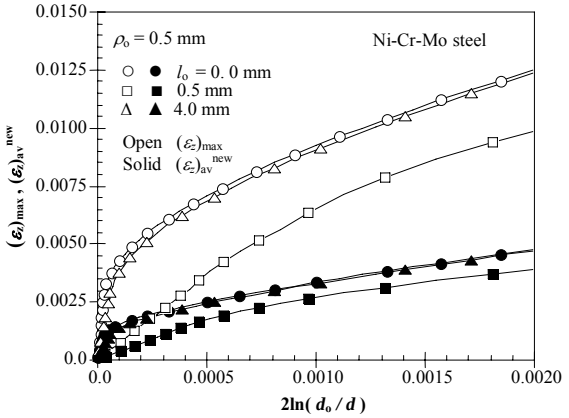

Figure 7. Variations of $(\varepsilon_z)_{max}$ and $(\varepsilon_z)_{av}^{new}$ with deformation.

11, 12 and 13. It is evident from these figures that the severest interference effect occurs when the notch pitch is nearly equal to less than 5 mm. A severe notch is usually understood as a notch having a large strain concentration. This occurs when the deformation is localized at and around the notch tips. This localization of deformation at the notch root is prominent for notch pitches greater than 5 mm; i.e. for notches that can be considered as single circumferential U-notch.

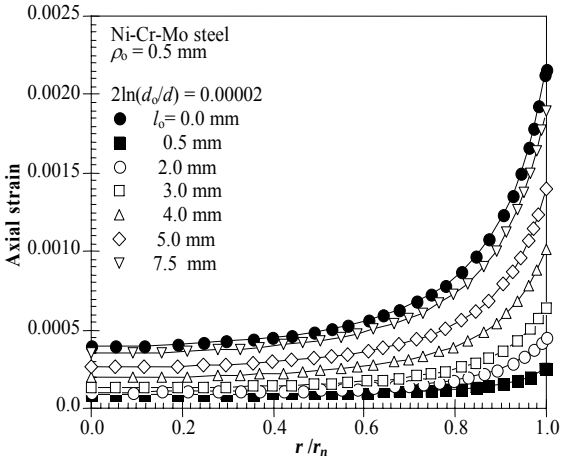

Figure 8. Distributions of the axial strain on the net section for Ni-Cr-Mo steel

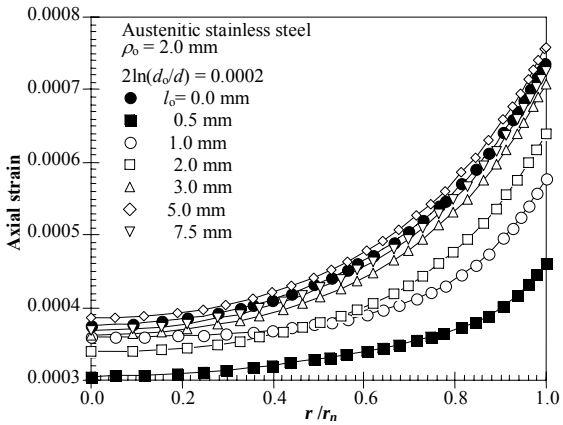

Figure 9. Distributions of the axial strain on the net section for Austenitic stainless steel.

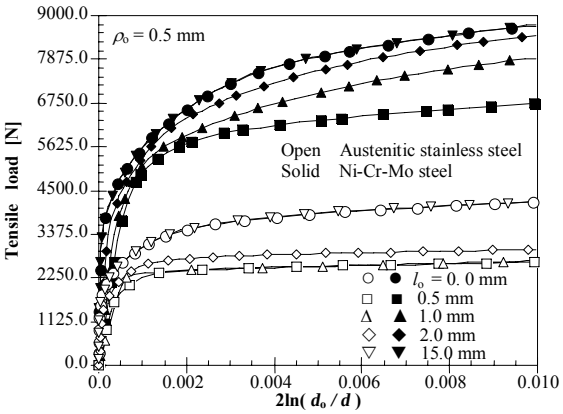

Figure 10. Variations of the tensile load with deformation for ρ_o = 0.5 mm.

It has been proved by the author in previous article that the relations between K_ε^{new} with P/P_Y are independent of the stress – strain curves [29]. Basically, the deformation parameter is related to the tensile load. Therefore, the parameter □; the ratio of deformation parameter to that at yielding at the notch root)is introduced here to eliminate the effect of stress – strain curves.

Figure 14 shows that the relationships of K_ε^{new} versus η are nearly independent of the stress-strain curve.

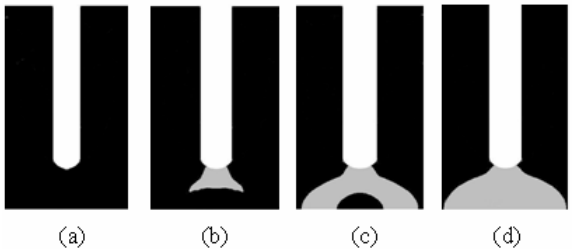

Figure 11. Distributions of axial strain on the net section of a single circumferential U-notch with ρ_o = 0.5 mm, **(a)**.Initial yielding at the notch root $2\ln(d_o/d)$ = 0.0000485, **(b)** . $2\ln(d_o/d)$ = 0.000376 , **(c)**. $2\ln(d_o/d)$ = 0.000645,**(d)**. $2\ln(d_o/d)$ =0.00121 .

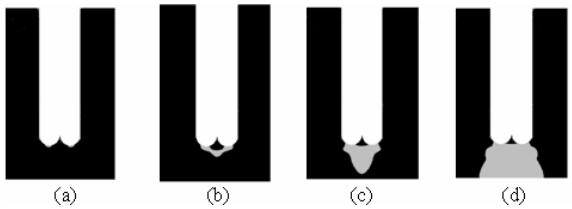

Figure 12. Distributions of axial strain on the net section of double circumferential U-notch with ρ_o = 0.5 mm and l_o = 0.5 mm **(a).** Initial yielding at the notch root $2\ln(d_o/d)$ = 0.00046,

(b). $2\ln(d_o/d)$ = 0.00074,**(c).** $2\ln(d_o/d)$ = 0.00181, **(d).** $2\ln(d_o/d)$ = 0.00413.

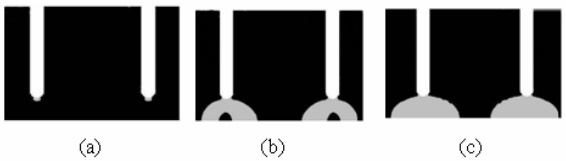

Figure 13. Distributions of axial strain on the net section of a double circumferential U-notch with ρ_o = 0.5 mm and l_o = 4.0 mm **(a)** Initial yielding at the notch root $2\ln(d_o/d)$ = 0.00018274, **(b)** $2\ln(d_o/d)$ = 0.0023982, **(c)** $2\ln(d_o/d)$ = 0.012380.

As a result, the effect of the rate of strain hardening is thus almost negligible on the variation of K_ε^{new} with $2\ln(d_o/d)$. This indicates that the main factor affecting the variation of K_ε^{new} with $2\ln(d_o/d)$ is the magnitude of yield stress. The only factor that affects the shape of K_ε^{new} with η curve is the notch geometry. On the other hand, the stress-strain curves of the ferrous materials used here are very different from each other. This suggests that any ferrous material should have the same variation of K_ε^{new} with η.

8. Conclusions

The interference effect on the new SNCF has been studied for notched cylindrical bars with double circumferential U-notches. The following conclusions can be drawn:

1. The interference effect on the elastic SNCF is prominent in the range $0.0 < l_o < 5.0$ mm for notch radius of 0.5 mm while it is prominent in the range $0.0 < l_o < 2.0$ mm for notch radius of 2.0 mm.
2. The direction of development of deformation from the notch radius is strongly affected by the notch pitch. Particularly, the deformation develops in inclined direction from the notch root to the center of the pitch. On the other hand, the deformation development is symmetric about the center of the net section for single circumferential U-notch (l_o = 0.0 mm) and double circumferential U-notch with $l_o > 5.0$ mm.
3. The new SNCF increases from its elastic value to its maximum as the plastic deformation develops from the notch root. The rate of increase in the new SNCF from its elastic to the maximum value decreases with decreasing notch pitch. The current results indicate that plastic deformation capacity of the notched bars is more pronounced as the notch pitch decreases.

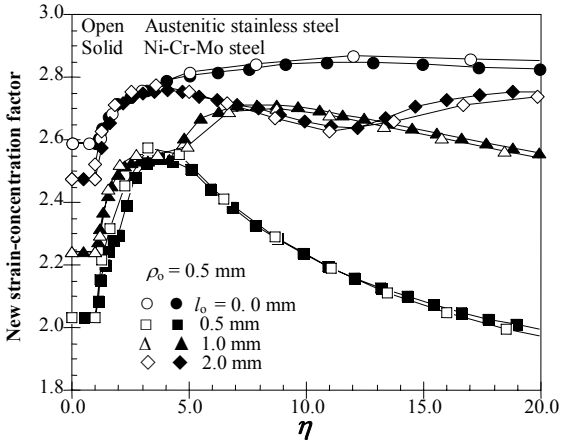

Figure 14. Variation in the new SNCF with non-dimensional parameter η for ρ_o = 0.5 mm.

References

[1] M.M. Leven, M.M. Frocht, "Stress-concentration factors for single notch in flat bar in pure and central bending". J. Appl. Mechanics, Vol. 74, 1952, 560-56.

[2] H.F. Hardrath, L. Ohman, "A study of elastic and plastic stress concentration factors due to notches and fillets in flat plates". National Advisory Committee Aeronautics, NACA Report 1117, 1953.Pilkey W.D. Peterson's stress concentration factors. New York: Wiley; 1997.

[3] Nishida K. Stress concentration. (In Japanese). Tokyo: Morikita Shuppan; 1974.

[4] N.A. Noda, M. Sera, Y. Takase, "Stress concentration factors for round and flat test specimens with notches". Int. J. Fatigue, Vol. 17, No. 3, 1995, 163-178.

[5] A. Kato, "Design equation for stress concentration factors of notched strips and grooved shafts". J. strain analysis, Vol 26, 1991, 21-28.

[6] H. Neuber, "Theory of stress concentration factor for shear-strained prismatical bodies with arbitrary nonlinear stress-strain law". J. Appl. Mechanics, Vol. 28, 1961, 544-550.

[7] P.S. Theocaris, "Experimental solution of elastic-plastic plane stress problems". J. Appl. Mechanics, Vol. 29, 1962, 735-743.

[8] [9] P.S. Theocaris, E. Marketos, "Elastic-plastic strain and stress distribution in notched plates under plane stress". J. Mech. Phys. Solids, Vol. 11, 1963, 411-428.

[9] A. J. Durelli, C.A. Sciammarella, "Elastoplastic stress and strain distribution in a finite plate with a circular hole subjected to unidimensional load". J. Appl. Mechanics, Vol. 30, 1963,115-121.

[10] P.S. Theocaris, "The effect of plasticity on the stress-distribution of thin notched plates in tension". J. Franklin Inst., Vol. 279, 1965, 22-38.

[11] K. Ogura, N. Miki, K. Ohji, "Finite element analysis of elastic-plastic stress and strain concentration factors under plane strain and axisymmetric conditions". (In Japanese).Trans. Japan Soc. Mech. Engrs., Vol. 47, 1981, 55-62.

[12] S.J. Hardy, M.K. Pipelzadeh, "An assessment of the notch stress-strain conversion rules for short flat bars with projections subjected to axial and shear loading". J. Strain Analysis, Vol. 31, No. 2, 1996, 91-110.

[13] T. Majima, "Strain-concentration factor of circumferentially notched cylindrical bars under static tension". J. Strain Analysis, Vol. 34, No. 5, 1999, 347-360.

[14] H.M Tlilan, S. Yousuke, T. Majima, "Effect of notch depth on strain-concentration factor of notched cylindrical bars under static tension". European Journal of Mechanics A / Solids, Vol. 24, No. 3, 2005, 406-416.

[15] W.N.Jr. Sharp, M. Ward, "Benchmark cyclic plastic notch strain measurements". Trans. ASME, J. Engg Mater. Technol., Vol. 105, 1983, 235-241.

[16] A.R. Gowhari-anaraki, S.J. Hardy, "Low cycle fatigue life predictions for hollow tubes with axially loaded axisymmetric internal projections". J. Strain Analysis, Vol. 26, 1991, 133-146.

[17] W.N.Jr. Sharp, "ASME 1993 Nadai Lecture-Elastoplastic stress and strain concentrations". Trans. ASME, J. Engng Mater. Technol., Vol. 117, 1995, 1-7.

[18] Z. Zeng, A. Fatemi, "Elasto-plastic stress and strain behaviour at notch roots under monotonic and cyclic loadings". J. Strain Analysis, Vol. 36, 2001, 287-288.

[19] G. Harkegard, T. Mann, "Neuber prediction of elastic-plastic strain concentration in notched tensile specimens under large-scale yielding". J. Strain Analysis, Vol. 38, 2003, 79-94.

[20] P. Livieri, G. Nicoletto, "Elastoplastic strain concentration factors in finite thickness plates". J. Strain Analysis, Vol. 38, 2003, 31-36.

[21] G. Glinka, "Energy density approach to calculation of inelastic strain-stress near notches and cracks". Engng. Fracture Mechanics, Vol. 22, 1985, 485-508.

[22] [23] Fuchs, H.O., Stephens, R.L. Metal Fatigue in Engineering. New York: John Wiley and Sons; 1980.

[23] [24] H.M. Tlilan, N. Sakai, T. Majima, "Strain-concentration factor of a single-edge notch under pure bending. (In Japanese)". Yamanashi District Conference, No. 40-4, Japan, October 10th 2004.

[24] H.M. Tlilan, N. Sakai, T. Majima, "Strain-concentration factor of rectangular bars with a single-edge notch under pure bending, (In Japanese)". J. Soc. Mat. Science, Vol. 54, No. 7, 2005, 724-729.

[25] [26] H.M. Tlilan, N. Sakai, T. Majima, "Effect of notch depth on strain-concentration factor of rectangular bars with a single-edge notch under pure bending". Int. J. Solids and Structures, Vol. 43, 2006, 459–474.

[26] T. Majima, "Interference effect of notches (1st report, evaluation of interference effect of notches on yield point load of double U-shaped notches by upper and lower bound theorems)". Trans. Japan Soc. Mech. Engrs., Vol. 48, No. 430, 1982, 719-728.

[27] T. Majima, K. Watanabe, "Interference effect of notches (2nd report, an experimental investigation of interference effect on strength and deformation properties of notched bars with double symmetrical u-notches". Trans. Japan Soc. Mech. Engrs., Vol. 48. No.433, 1982, 1186-1194.

[28] H.M. Tlilan, A.S. Al-Shyyab, A.M. Jawarneh, A.K. Ababneh, "Strain-concentration factor of circumferentially v-notched cylindrical bars under static tension". Journal of Mechanics, Vol. 24, No. 4, 2008, 419-428.

JJMIE

Volume 3, Number 2, June. 2009
ISSN 1995-6665
Pages 105 - 110

Jordan Journal of Mechanical and Industrial Engineering

Performance, Emission and Combustion of LPG Diesel Dual Fuel Engine using Glow Plug

P.Vijayabalan [a,*] , G. Nagarajan [b]

[a] *Dept. of Mechanical Engineering, Hindustan College of Engineering, Chennai, India*

[b] *Dept. of Mechanical Engineering, Anna university, Chennai, India*

Abstract

A single cylinder vertical air-cooled diesel engine was modified to use LPG in dual fuel mode to study the performance, emission, and combustion characteristics. The primary fuel, liquefied petroleum gas (LPG), was mixed with air, compressed, and ignited by a small pilot spray of diesel. Dual fuel engine showed a reduction in oxides of Nitrogen and smoke in the entire load range. However, it suffers from the problem of poor brake thermal efficiency and high hydrocarbon and carbon monoxide emissions, particularly at lower loads due to poor ignition. In order to improve the performance at lower loads, a glow plug was introduced inside the combustion chamber. The brake thermal efficiency improved by 3% in the glow plug assisted dual fuel mode, especially at low load, and also reduced the hydrocarbon, carbon monoxide, and smoke emissions by 69%, 50% & 9% respectively. The presence of glow plug had no effect on oxides of Nitrogen.

Keywords: Liquefied Petroleum Gas; Glow Plug; Performance; Emission; Combustion

1. Introduction

LPG vehicles are being rapidly developed as economical and low-pollution cars [1-2] .The potential benefits of using LPG in diesel engines are both economical and environmental [3]. In the dual fuel gas engines, the gaseous fuel is inducted along with the air, and this mixture of air and gas is compressed like in conventional diesel engines. A small amount of diesel, usually called the pilot, is sprayed near the end of the compression stroke to initiate the combustion of the inducted gas air mixture [4-5]. With reduced energy consumption, the dual fuel engine shows a significant reduction in smoke density, oxides of nitrogen emission, and improved brake thermal efficiency [6]. The combustion of this pilot diesel leads to flame propagation and combustion of the gaseous fuel. The engine can be run in the dual fuel mode without any major modification, but is usually associated with poor brake thermal efficiency and high HC & CO emissions at low loads [7].

The increase in pilot diesel improves the brake thermal efficiency at low loads. At higher loads, it reduces efficiency due to rapid combustion [8-9]. Low efficiency and poor emissions at light loads can be improved significantly by advancing injection timing of the pilot fuel [10-11]. Any measures that lower the effective lean flammability limit of charge and promote flame propagation will improve part load performance [12]. The gas concentration is low at lower loads, thus ignition delay period of pilot fuel increases, and some of the homogeneously dispersed gaseous fuel remains unburned which results in poor performance. A concentrated ignition source is needed for combustion of the inducted fuel at low loads [13]. Poor combustion of the gaseous fuel at low loads results in higher emission of carbon monoxide and unburned hydrocarbons.

The hot surface assisted ignition concept is commonly applied to overcome the low temperature-starting problem in diesel engine. Introducing low cetane fuel such as alcohol and natural gas requires an extended application of the hot surface as continuous ignition assistance. The function of the hot surface is to provide favourable local ignition condition, followed by combustion propagating through the fuel air mixture to establish a stable diffusion flame [14-16].

The objective of the present work is to improve part load efficiency, which is the main drawback in dual fuel operation. In the present experimental work, the effect of introducing glow plug inside combustion chamber, which was not attempted earlier in the dual fuel operation, was studied. Pilot fuel quantity of 8.5 mg/cycle was introduced. It preheats the gas air mixture; and reduces the delay period of the pilot diesel. This results in improvement in the performance and in reduced emissions at low loads.

2. Experimental Setup and Experimentation

A single cylinder, 3.7 kW, four strokes, direct injection, and air-cooled diesel engine coupled to an electrical

* Corresponding author . pvbalan72@gmail.com

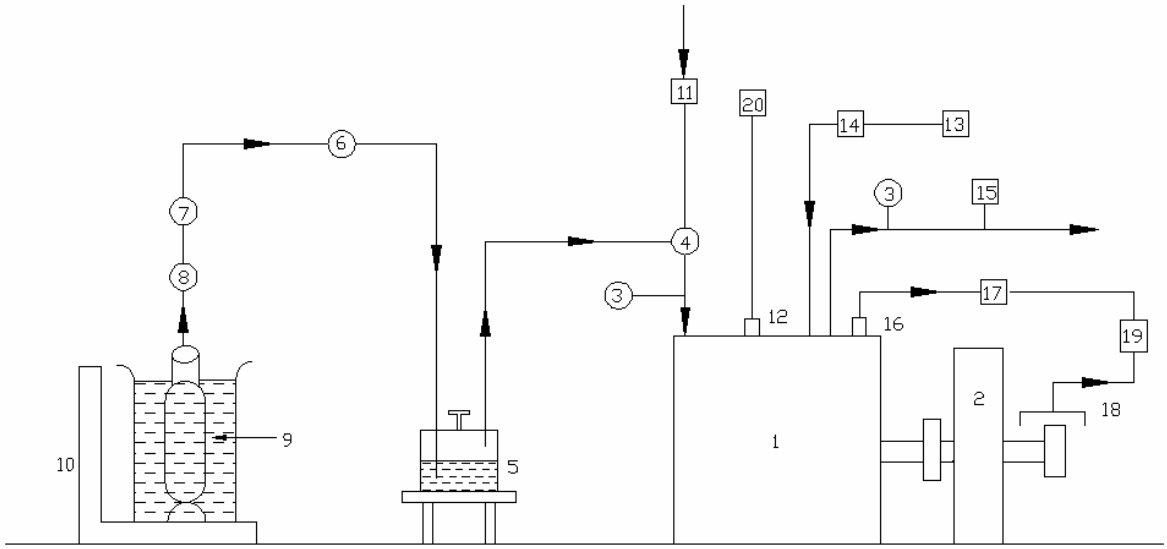

Figure 1. Schematic of the experimental set up.
* 1 Engine, 2 Dynamometer, 3 Temperature measurement, 4 Gas –air mixture, 5 Flame trap, 6 Gas flow meter, 7 Pressure regulator, 8 Control valve, 9 LPG cylinder, 10 Weighing machine, 11 Air flow surge tank, 12 Glow plug, 13 Diesel tank, 14 Diesel flow measurement, 15 Exhaust gas analyser, 16 Pressure pick up, 17 Charge amplifier, 18 Shaft position encoder, 19 CRO, 20 Battery

dynamometer were used for the experiments.The specifications of the DI diesel engine are shown in Table 1.

Table 1. Specifications of the test engine.

General detail	Single cylinder, four stroke, compression ignition, constant speed, vertical, air cooled, direct injection
Bore	80mm
Stroke	110mm
Compression ratio	16.5:1
Rated output	3.7kW at 1500 rpm
Rated speed	1500 rpm
Injection pressure	200 bar

The engine was modified to work in the dual fuel mode by connecting LPG line to the intake manifold with a flame trap, non-return valve, needle valve, and mixing unit [17]. A digital type platform weighing machine having an accuracy of 2 mg was used to measure the LPG fuel flow by weight difference method with an uncertainty of 1.8 %. A Kistler make piezo electric transducer with a sensitivity of 14.2 pC/bar was installed with a Kistler charge amplifier for monitoring the cylinder pressure. This was recorded in a personal computer. Using analog to digital converter, the average pressure was obtained from 100 consecutive cycles. Carbon monoxide and unburned hydrocarbons emissions were measured using a NDIR gas analyser with an uncertainty of 5%. Smoke emissions were measured by means of a Bosch smoke meter with an uncertainty of 6%. NOx emissions from the engine were measured using a Crypton make analyser with an uncertainty of 6%. Chromel – alumel (K – type) thermocouple was used to measure the exhaust gas temperature with an uncertainty of 0.5 º C. The brake thermal efficiency was calculated by considering the calorific value and mass flow rate of both fuels.

$$\textit{Brake thermal efficiency} = \textit{brake power} / ((m_f x\ CV)_{LPG} + (m_f x\ CV)_{Diesel}) \quad (1)$$

The schematic of the experimental setup is shown in Fig 1.

The experimental procedure consists of the following steps:

- Initially, engine was tested using the base fuel diesel at all loads to determine the engine operating characteristics and pollutant emissions. The engine speed was maintained constant through out the entire engine operation at 1500 RPM.
- The same procedure was repeated in dual fuel mode with 8.5 mg/cycle pilot diesel, with and without glow plug .The glow plug was powered by12V battery, and it was maintained at a maximum temperature of 850º C throughout the engine operation. The pilot diesel quantity was maintained constantly for the entire load range by varying the flow rate of LPG for each load condition. The mass fraction of LPG in the blend (Z) is shown in Table 2.

$$Z = (\dot{m}_{LPG} / (\dot{m}_{Diesel} + \dot{m}_{LPG})) \times 100\ \% \quad (2)$$

Table 2. Mass fraction of LPG in the blend .

Load in %	0	20	40	60	80	100
DF with GP (Z)	13.4	18.9	38.1	49.1	57.0	63.4
DF without GP (Z)	23.1	34.7	45.2	49.6	55.9	62.3

During the engine test conditions, the cylinder pressure, exhaust gas temperature, fuel consumption, exhaust

smoke, and exhaust gas emissions were recorded at all the loads.

3. Results and Discussion

The results obtained in the dual fuel operation with and without the assistance of glow plug are compared to diesel; and are presented.

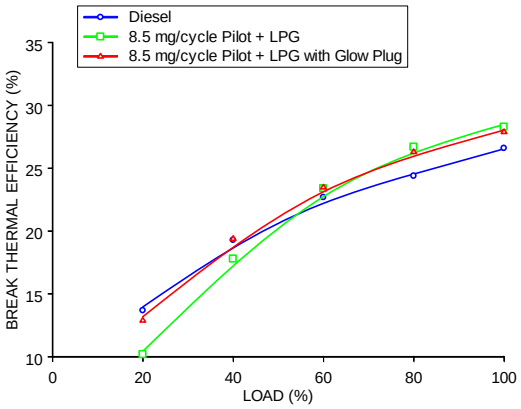

Figure 2 .Variation of Brake Thermal Efficiency with Load.

3.1. Brake Thermal Efficiency

The variation of brake thermal efficiency against load is shown in Figure 2. The glow plug assisted dual fuel mode of operation improves the efficiency by 2% up to 80% load, but there is no significant variation at full load operation. Brake thermal efficiency ranges from 12.9 % to 27.9 % with glow plug operation whereas in the case of dual fuel mode of operation without glow plug, it varies from 10.2 % to 28.3 %. This may due to the reduction in delay period of pilot diesel and an increase in the mixture temperature around the glow plug. The brake thermal efficiency for diesel varies from 13.7 % to 26.6 %.

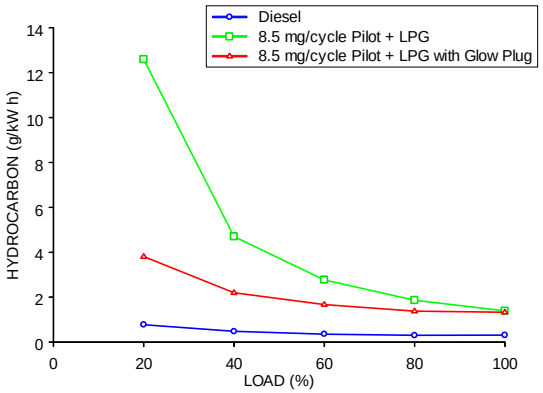

Figure 3. Variation of Hydrocarbon with Load.

3.2. HC and CO Emissions

Figure 3 shows the variation of hydrocarbon emission against load. The hydrocarbon emission is reduced throughout the engine operation in glow plug assisted dual fuel mode in comparison to dual fuel mode of operation. It ranges from 3.81 g/kW h to 1.33 g/kW h whereas in the case of dual fuel mode of operation without glow plug, it ranges from12.6 g/kW h to 1.4 g/kW h, and for diesel from 0.78 g/kW h to 0.31 g/kW h.

Reduction in delay period of pilot diesel, increase in pre flame reaction near the injector due to glow plug temperature, and high temperature of gas air mixture around the glow plug are the reasons for lower emissions in the case of glow plug assisted dual fuel operation.

The variation of CO emissions against load is shown in Figure 4. The CO emission is reduced throughout the engine operation in the glow plug assisted dual fuel mode in comparison to dual fuel mode of operation. It ranges from 0.49 g/kW h to 0.13 g/kW h whereas in the case of dual fuel mode of operation without glow plug, it ranges from 0.99 g/kW h to 0.14 g/kW h. The reason for lower emission is the increased mixture temperature by the glow plug temperature, which creates local turbulence and increase in flame velocity. The CO emission for diesel varies from 0.24 g/kW h to 0.11 g/kW h.

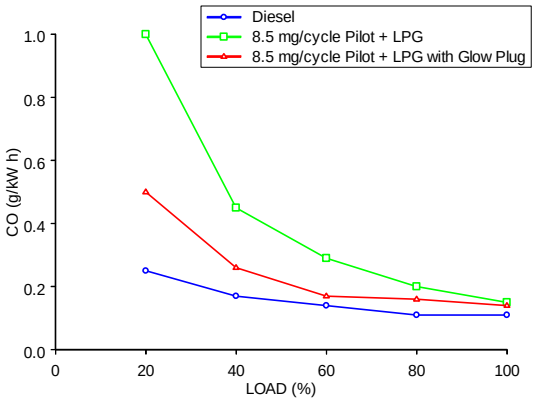

Figure 4 .Variation of CO with Load.

3.3. NOx Emission

The variation of NOx emission with load is shown in Figure 5. It increases marginally in the case of glow plug assisted dual fuel mode in comparison to dual fuel mode of operation. It ranges from 3.7 g/kW h to 3.1 g/kW h, whereas in the case of dual fuel mode of operation without glow plug, it varies from 3.28 g/kW h to 2.82 g/kWh, and for diesel from 7.77 g/kW h to 6.28 g/kW h. The primary fuel forms a homogeneous mixture, and it leads to complete combustion and rise in the peak pressure resulting in high temperature inside the engine during combustion, and it increases the possibility of NOx formation.

3.4. Smoke

The variation of smoke emissions against load is shown in Figure 6. A marginal reduction in smoke emission throughout the engine operation can be noticed in the glow plug assisted dual fuel mode in comparison to dual fuel mode of operation without glow plug. It ranges from 0.2 to 0.92 BSU whereas in the case of dual fuel mode of operation without glow plug, it ranges from 0.2 to 1.2 BSU. The reduction of smoke may be due do lower carbon/hydrogen ratio of LPG. The smoke emission for diesel varies from 0.2 to 0.92 BSU

  - Volume 3, Number 2 (ISSN 1995-6665)

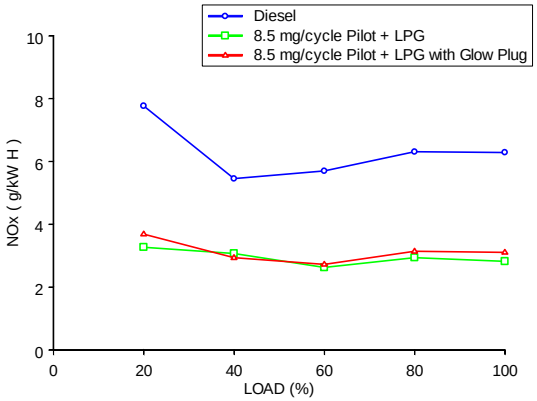

Figure 5. Variation of NOx with Load .

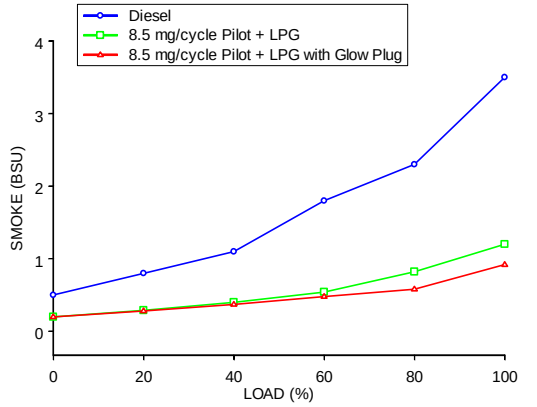

Figure 6. Variation of Smoke with Load.

3.5. Exhaust Gas Temperature

Figure 7 shows the variation of exhaust gas temperature against load. A marginal increase in exhaust gas temperature is noticed throughout engine operation in the glow plug assisted dual fuel mode due to high combustion temperature. It ranges from 215°C to 535°C, whereas in the case of duel fuel operation without glow plug it varies from 201°C to 531°C. The diesel mode of operation shows a variation from 224°C to 571°C.

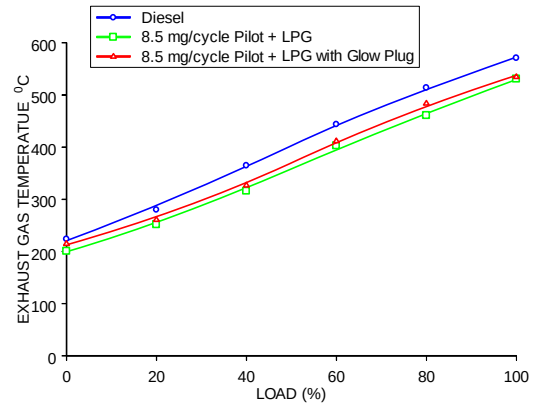

Figure 7 .Variation of Exhaust gas temperature with Load .

3.6. Combustion Parameters

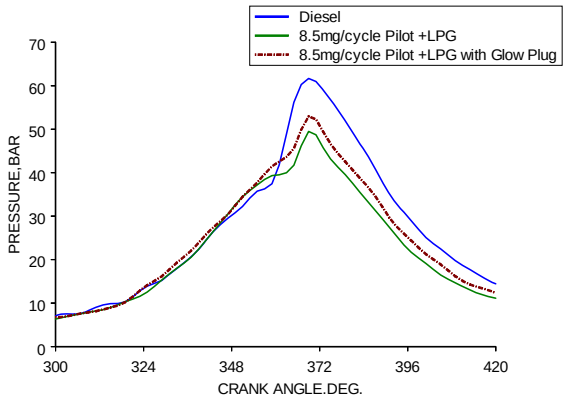

Figure 8. Variation of Pressure with Crank angle at 20 % Load.

3.6.1. Pressure Crank Angle Diagram

Figure 8 shows the cylinder pressure with crank angle for diesel, dual fuel mode, and glow plug assisted dual fuel mode at 20% of full load. The peak pressure in dual fuel mode without glow plug is 50 bars, and in glow plug assisted dual fuel mode it is 53 bars whereas in the case of diesel it is 61 bars. At low loads, pilot diesel initiates the combustion followed by LPG combustion due to high self-ignition temperature of LPG. It leads to a retardation in the peak pressure by 3˚ CA .The glow plug temperature reduces the delay period resulting in an increase in peak pressure.

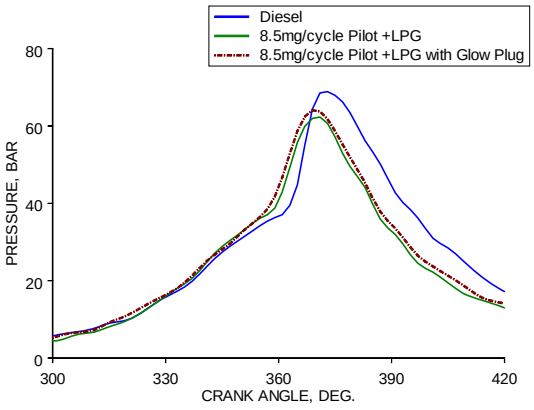

Figure 9. Variation of Pressure with Crank angle at Full Load

Figure 9 shows the cylinder pressure with crank angle at full load. The cylinder pressure obtained in dual fuel mode is less than the base diesel. The peak pressure obtained in the dual fuel mode of operation without glow plug is 62 bars, and in glow plug assisted dual fuel mode it is 64 bars whereas in diesel it is 68.7 bars. The peak pressure in the dual fuel mode is advanced by 2˚CA when compared to diesel. It is due to pre combustion of LPG followed by diesel combustion.

3.6.2. Heat Release Rate

The rate of heat release curves are drawn using pressure and crank angle value in the existing software. Figure10 shows the rate of heat release for glow plug assisted dual fuel mode, dual fuel mode, and diesel mode

at 20% of full load. The combustion starts at the same crank angle of about 5° CA BTDC for both glow plug assisted dual fuel operation and diesel. But the combustion starts 5° CA after the glow plug assisted dual fuel operation in dual fuel operation without glow plug. The peak heat release rate of glow plug assisted dual fuel mode is 41 J /° CA, dual fuel mode is 34.9 J / ° CA, and for diesel mode it is 52 J / ° CA. Figure 11 shows the rate of heat release at full load. The peak heat release rate of glow plug assisted dual fuel mode is 59.7 J / ° CA, dual fuel mode is 48.4 J / ° CA, and for diesel mode it is 82.7 J / ° CA. The combustion in glow plug assisted dual fuel operation starts 2° CA before diesel. The combustion may be initiated by the glow plug before the pilot injection of diesel in the glow plug assisted dual fuel operation.

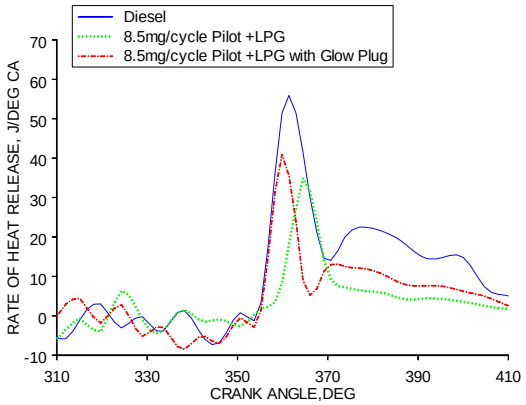

Figure 10. Variation of Heat Release Rate with Crank angle at 20 % Load.

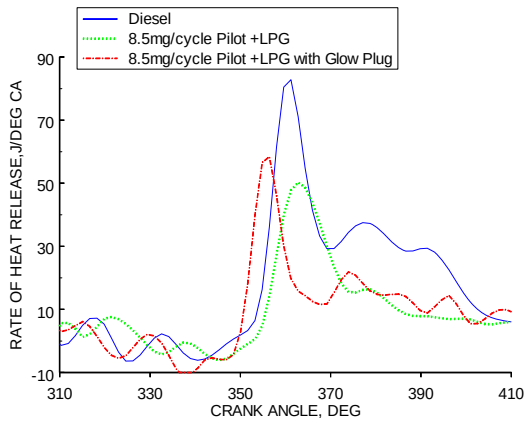

Figure 11. Variation of Heat Release Rate with Crank angle at Full Load.

4. Conclusions

The following conclusions are drawn based on the experimental investigation

- The glow plug assisted dual fuel mode shows an improvement of 3% in brake thermal efficiency at low loads compared to dual fuel mode of operation, with no appreciable change at high loads.
- HC and CO emissions are reduced by 69% and 50% in the glow plug assisted dual fuel mode of operation compared to dual fuel mode of operation without glow plug, but marginally higher than in diesel.
- The emission of smoke is reduced by 9% in the glow plug assisted dual fuel mode of operation compared to dual fuel mode of operation. Compared to diesel, it reduces by 69%.
- The glow plug assisted dual fuel operation improves the combustion. It shows higher peak heat release rate, compared to dual fuel operation without glow plug.
- The peak pressures are higher in glow plug assisted dual fuel operation in the entire load range when compared to dual fuel operation without glow plug.

In general glow plug assistance improves the part load performance in dual fuel engine with a significant reduction in emissions.

REFERENCES

[1] B. Stanislav, “The development of gas (CNG, LPG and H_2) engines for buses and trucks and their emission and cycle variability characteristics”. SAE Transactions, 2001-01-0144, 2001.

[2] H.E. Saleh, “Effect of variation in LPG composition on emissions and performance in a dual fuel diesel engine". Fuels, Vol. 87, No.13-14, 2008, 3031-3039.

[3] D.H. Qi, Y.ZH. Bian, ZH.Y. Ma, CH.H. Zhang, SH.Q. Liu, “Combustion and exhaust emission characteristics of a compression ignition engine using liquefied petroleum gas-Diesel blended fuel". Energy Conversion and Management, Vol. 48, No.2, 2007, 500 -509.

[4] D.T. Hountalas, R.G. Papagiannakis, “Development of a simulation model for direct injuction dual fuel Diesel-natural gas engine”. SAE Transactions, 2000-01-0286, 2000.

[5] R.G. Papagiannakis, D.T. Hountalas, “Experimental investigation concerning the effect of natural gas percentage on performance and emissions of a DI dual fuel Diesel engine”. Applied Thermal Engineering, Vol. 23, No. 3, 2003, 353-365.

[6] C.V. Sudhir, H. Vijay, S. Desai, Y. Kumar, P. Mohanan, “Performance and emission studies on the injection timing and diesel replacement on a 4-S LPG-Diesel-fuel engine ”. SAE Transactions, 2003-01-3087, 2003.

[7] Y.E. Mohamed, M.S. Selim, H.E. Radwan, H.E. Saleh, “Improving the performance of dual fuel engines running on natural gas/LPG by using pilot fuel derived from jojoba seeds”. Renewable Energy, Vol. 33, No. 6, 2008, 1173-1185.

[8] M.P. Poonia, “Experimental investigation of the factors affecting the performance of a LPG-Diesel dual fuel mode”. SAE Transactions, 1999-01-1123, 1999.

[9] M.P. Poonia, “Experimental investigation on the performance of a LPG-Diesel dual fuel engine”. XV National Conference on I.C Engines and Combustion, Vol.1, 1997, 117 -122.

[10] G.H. AbdAlla, H.A. Soliman, O.A. Badr, M.F. Abd.Rabbo, “Effect of injection timing on the performance of a dual fuel engine ”, Energy Conversion and Management, Vol. 43, No.2, 2002, 269-277.

[11] G.H. AbdAlla, H.A. Soliman, O.A. Badr, M.F. AbdRabbo, “Effect of pilot fuel quantity on the performance of a dual fuel engine”, Energy Conversion and Manageement, Vol. 41, No.6, 2000, 559-572.

[12] Karim GA. The dual fuel engine. In: Evans, L.Robert, editors. Automotive Engine Alternatives, New York: Plenum Press, 1987, p. 83 - 104.

[13] G. A. Karim, "An Examination of some measures for improving the performance of gas fuelled diesel engine at light load". SAE Transactions, 912366, 1991.

[14] W.A Goetz. "Utilizing neat methanol and glow plug ignition in DI Diesels: Laboratory testing of a single and multi-cylinder engine". SAE Transactions, 941044, 1994.

[15] H. Valland, "Hot surface assisted compression ignition of natural gas in a direct injection of diesel engine". SAE Transactions, 960767, 1996.

[16] T. Fukama, T. Fujitha, P. Pichainarong, S. Furuhama, "Hydrogen combustion study in direct injection hot surface engine". SAE transactions, 861579, 1986.

[17] N.K. Miller, G. Nagarajan, S. Renganarayanan, "LPG fueled diesel engine using diethyl ether with exhaust gas recirculation", International Journal of Thermal sciences, Vol. 47, No. 4, 2008, 450 - 457.

JJMIE

Volume 3, Number 2, June. 2009
ISSN 1995-6665
Pages 111 - 118

Jordan Journal of Mechanical and Industrial Engineering

Carbonyls Emission Comparison of a Turbocharged Diesel Engine Fuelled with Diesel, Biodiesel, and Biodiesel-Diesel Blend

Asad Naeem Shah [a, b,*], Ge Yun-shan [a], Tan Jian-wei [a]

[a] School of Mechanical and Vehicular Engineering, Beijing Institute of Technology, Beijing 100081, P.R China

[b] Department of Mechanical Engineering, University of Engineering and Technology, Lahore 54000, Pakistan

Abstract

In order to characterize the carbonyls emissions from a turbocharged, direct injection, and intercooled compression ignition engine, an experimental study was conducted using diesel, biodiesel, and 20% biodiesel-diesel blend as test fuels. Fourteen carbonyls were identified and quantified from the engine exhaust at four different engine conditions. Experimental results show that formaldehyde and total carbonyls from the test fuels exhibit maximum BSE at low load, which decreases with the increase in load. Carbonyls such as formaldehyde, acetaldehyde, acrolein + acetone, propionaldehyde, crotonaldehyde, and methyl ethyl ketone show higher, but aromatic aldehydes (benzaldehyde and tolualdehyde) reflect lower BSE from B20 and B100 as compared to diesel fuel. Total carbonyls emissions from B20 and B100 are 8% and 32% higher respectively than those from diesel fuel. Formaldehyde is the most abundant carbonyl of the test fuels with 56.5%, 53.9%, and 52.7% contribution to total carbonyls in case of diesel, B20, and B100 respectively. Specific reactivity of carbonyls from the test fuels follow the order as B20 < D < B100.

Keywords: Turbocharged Engine; Direct Injection; Biodiesel; Unregulated Emissions; Carbonyls

NOMENCLATURE

CC	carbonyl compound or carbonyls
SR	specific reactivity
MIR	maximum incremental reactivity
BSE	brake specific emission
NO_x	oxides of nitrogen
SO_x	oxides of sulfur
CO	carbon monoxide
THC	total hydrocarbons
PM	particulate matter
CO_2	carbon dioxide
EPA	environment protection agency

1. Introduction *

Internal combustion engines (both compression ignition and spark ignition) at the present time are facing the dual challenges of exhausting fossil fuels and ever-tighter emission standards. Because of their superiority in fuel economy, output power, and lower emissions of hydrocarbons (HC) and carbon- monoxide (CO), diesel engines rule over the fields of commercial transportation, construction, and agriculture. However, diesel engines are responsible for higher amount of particulate matter (PM), oxides of nitrogen (NO_x), carbon dioxide (CO_2), and oxides of sulphur (SO_x) which cause acid rain [1]. In this menace, biodiesel has not only resolved the issue of energy security but also proved its friendliness to the environment.

When a new fuel is introduced into the market, a prerequisite is that emissions are not to be more toxic than the emissions obtained when running on the standard market fuel [2]. Biodiesel, derived from vegetable oils or animal fats, consists of alkyl monoesters of fatty acids; and has received great attention as a substitute fuel in many countries because of its potential to reduce air pollutants like PM, THC, CO and SO_x [3-5]. It is well established that blends of biodiesel with conventional fossil fuel can be used in an unmodified diesel engine [6-7]. Biodiesel also reduces the polycyclic aromatic hydrocarbons (PAHs) and carcinogenicity [8], mutagenicity [9]; and has less adverse effect on human health as compared to diesel [10]. The performance of the engine remains unaffected when the biodiesel and diesel are compared on the basis of relative equivalence ratio [11]. Some studies have revealed an increase in rated power or torque when using biodiesel [12-13]. It has also been proved that biodiesel can reduce the extent of damage, coefficient of friction, wear of engine, and it improves the life of its vital moving parts [14].

In urban, atmospheric carbonyl compounds are mainly emitted from vehicular exhaust; and are an important class of vehicular total hydrocarbon (THC) emissions [15]. They are well known to participate in photochemical smog formation; and are important precursors of ozone and other

* Corresponding author. naeem_138@hotmail.com

hazardous substances such as peroxylacylnitrate (PAN) [16]. Some carbonyls such as formaldehyde, acetaldehyde, acrolein, and methyl ethyl ketone are toxic, mutagenic, and even carcinogenic to human body [17].

Although a lot of studies have been carried out on biodiesel for regulated and unregulated emissions, a limited and discordant literature is available on carbonyl compounds (CC). Literature data for carbonyls are somewhat conflicting due to biodiesel origin, engine type, engine conditions, and modes of operation [18]. In this study, an effort has been made to investigate the carbonyls, to analyze their behavior to different engine loads, and to make their comparison on the basis of used test fuels. In the end, ozone forming potential of these pollutants has been discussed in term of their specific reactivity (SR).

2. Material and Methods

2.1. Engine, Test Fuels and Experimental Conditions

The experiments were performed on a 4CK Diesel Engine (4-cylinder, turbocharged, direct injection, and intercooled). An electrical dynamometer (SCHENCK HT 350) was coupled to the engine to measure its power. No modification or alteration was made in the engine, and it was warmed up before starting the experiments. The schematic diagram of the experimental setup is given in figure 1, and the parameters of the engine are listed in Table 1. The engine was operated at constant speed (2300 r/min) for varying loads (10%, 20%, 50% and 100%).

The main properties of commercial diesel (D), biodiesel (B100), and its 20% blend (by volume) with diesel (B20) used in this study are given in Table 2. A 20% biodiesel-diesel blend (B20) has been taken in this study because B20 has become the most popular biodiesel fuel blend used, and this blend level has been studied in different countries [19, and references therein]. Biodiesel was produced from waste cooking oil.

Table.1 Engine specifications.

Items	Value
Number of cylinders	4
Bore (mm)	110
Stroke (mm)	125
Displacement (Liter)	4.752
Compression Ratio	16.8
Rated Power (kW@ r/min)	117/2300
Maximum Torque (Nm@ r/min)	580/1400
Nozzle hole diameter (mm)	0.23
Number of nozzle holes	6

2.2. Sampling Methodology

The sampling scheme is shown in figure 1. An ejector-diluter (Dekati Ltd. Finland) was used to obtain the emission directly from the exhaust pipe by inserting a J-shaped stainless- steel sample probe into the exhaust pipe as shown in figure 1. The exhaust gas from the engine was diluted by using dilution ratio of about 8. The real dilution ratio was determined by using the two concentrations of CO_2 which were measured before and after the dilution instrument. In order to get constant flow, a calibrated constant volume sampling (CVS) pumps (SKC USA, AirChek2000) shown in figure 2 (b), were used. The sampling rate was 260 ml/min, and it took 30 minutes to sample at every mode. Three samples of each diesel, B20, and B100 were taken for the four modes of operation. Carbonyls were sampled using 2, 4-dinitrophenylhydrazine (DNPH) coated silica gel cartridges (Accustandard® Inc) at 1 m away from the outlet of exhaust emission of the engine. The cartridges are shown in figure 2 (a). The DNPH inside the cartridges trapped the carbonyls to react with them and to form the corresponding stable 2, 4-dinitrophenylhydrazone derivatives. All the samples were collected at a temperature less than 60˚C, which is well below the melting points of the DNPH and DNPH-hydrazones. After sampling, the cartridges were sealed with aluminum foil and were refrigerated at -10˚C for the next process.

2.3. Sample Extraction

For the extraction of samples, solid phase extraction (SPE) was used. It is a column chromatography separation process in which 2, 4-DNPH sampling cartridges were placed on solid phase extractor (USA Supelco Inc.) and sampled material was eluted from the cartridges by washing it with 3 ml acetonitrile (USA Fisher Company). The extract was collected in a small test tube; and was filtered through a micro-pore filter of 0.45 μm membrane. The filtered elute was then poured into a 5 ml volumetric flask to get a constant volume solution with acetonitrile. Air bubbles were removed from the sample using ultrasonic degasser for 3 to 5 minutes, and final sample was then refrigerated in labeled sampling tube for the analysis within seven days.

2.4. Qualitative and Quantitative Analysis of Carbonyls

After the sampling and extracting, the sampled material was analyzed in the laboratory for the carbonyl compounds according to the environment protection agency (EPA) standard method TO-11A [20], using high performance liquid chromatography (HPLC) (USA Agilent 1200LC) system with an automatic injector and an ultraviolet detector. The radiant point of ultraviolet detector is a deuterium arc discharge lamp capable of launching wavelength of 190 nm to 600 nm ultraviolet. The HPLC system is shown in the figure 2 (c). A C18 column (Agilent Eclipse XDB-C18, 4.6 mm x 150 mm, 5μm) was used to elute the formed carbonyls-DNPH derivatives. Acetonitrile and distilled water were used as mobile phases according to a volume ratio of 60% acetonitrile/40% water (v/v). The flow rate and injection volume were 1.0 mL/min and 25 μL respectively, the temperature gradient was 25˚C, and carbonyl-DNPHs were detected at 360 nm.

Compounds were identified by matching the HPLC retention time with those of authentic standards (USA Supelco). The purchased standard solution was containing 14 kinds of carbonyl derivatives such as formaldehyde,

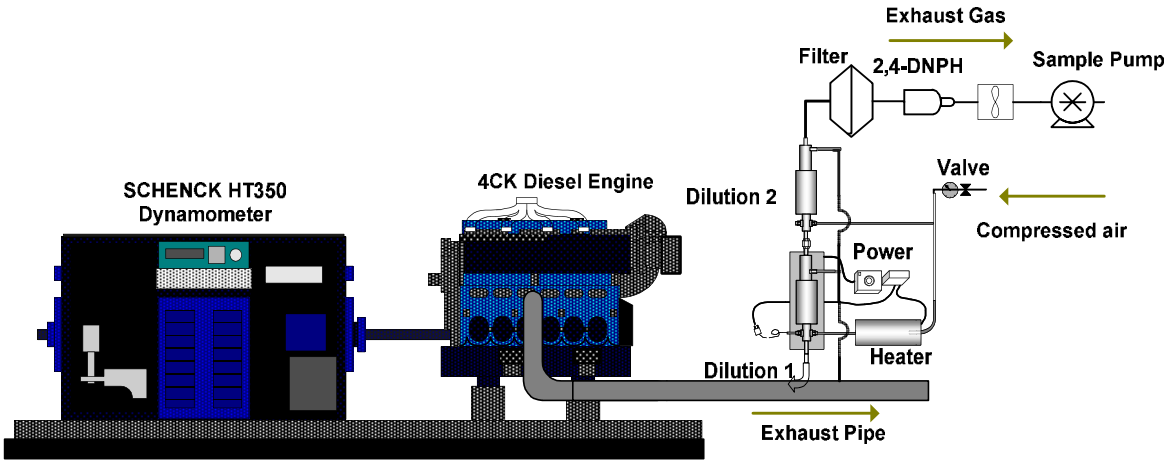

Figure 1. Experimental setup.

Table 2. Properties of fuels.

Properties	B100	B20	D	Standards
Density (kg/m^3)	886.4	845.1	834.8	SH/T 0604
Viscosity (mm^2/s) at 20 ºC	8.067	4.020	3.393	GB/T 265
Lower heating value (MJ/kg)	37.3	41.57	42.8	GB/T 384
Sulfur content (mg/L)	25	n/a	264	SH/T 0253-92
Cetane number	60.1	n/a	51.1	GB/T 386-91
Carbon content (wt %)	76.83	n/a	86.92	SH/T 0656-98
Hydrogen content (wt %)	11.91	n/a	13.08	SH/T 0656-98
Oxygen content (wt %)	11.33	n/a	0	Element analysis

acetaldehyde, acrolein, acetone, propionaldehyde, crotonaldehyde, methyl ethyl ketone, methacrolein, butyraldehyde, benzeldehyde, valeraldehyde,tolualdehyde, cyclohexanone, and hexanal. Because of their same retention time (almost same), it was difficult to separate acrolein and acetone in the column.

After the qualitative analysis, compounds were quantified using the external standard method to make the linear standard curves. The purchased standard solution was taken in 0.5 µL, 1µL, 2 µL, 5 µL, 10 µL, and 20 µL respectively with the help of micro- sampler. They were analyzed under a given chromatographic conditions, and the peak areas were recorded. According to these standard curves, the target compounds were quantified by the regression method of their peak areas. The curve equation, the correlation coefficient, and relative standard deviation (RSD) of each compound are given in Table 3.

3. Results and Discussion

3.1. Effect of Load on Brake Specific Emission of Major Carbonyls

Brake specific emission (BSE) is defined as the mass of the pollutants emitted per kilo-watt power developed in the engine in one hour. From Table 4, it is clear that there is a positive correlation between load and brake specific emission (BSE) of total carbonyl compounds (CC) and between load and BSE of formaldehyde and acetaldehyde which are two major carbonyls from the test fuels. At low load (10%), total CC show maximum BSE for all the test fuels. The BSE of total CC decreases as the load increases. This trend is more uniform for B100. However, both B20 and diesel show an increase in BSE at full load (100%) with their minimum BSE at 75% load. This anomaly may be ascribed to the different stoichiometric air/fuel ratio of biodiesel (12.6) and fossil diesel (14.6) [21]. The possible reason for maximum BSE of total CC at low load may be the incomplete combustion of the fuels due to the large excessive air/fuel ratio and increase in over-lean mixture area, which results in high carbonyl compounds and other pollutants. The reason for the increase in BSE of diesel and B20 at full load may again be the incomplete combustion, but this time is due to the decrease in excessive air/fuel ratio resulting in rich mixture formation in the combustion chamber, and hence reducing the oxidation rate. It has also been reported that load level (air/fuel ratio) of engine significantly affects the carbonyl compounds [22]. The minimum BSE of carbonyls at 75% load in the cases of diesel and B20 indicate that at this load level optimum air/fuel ratio occurs, so both of the fuels combust completely with minimum carbonyls emissions.

The BSE of formaldehyde shows maximum value at 10% load, and then decreases with the increase in load for all the test fuels. However, it displays its minimum value at full load for diesel and B100, and at 75% load for B20.

(a)

(b)

(c)

Figure 2. (**a).** 2, 4-DNPH sampling cartridges (**b).** CVS pumps (**c**). High-performance liquid chromatographic (HPLC) system.

Table 3. Curve equations, correlation coefficients, and RSD of carbonyl compound (n=5; where n is number of replicates).

Carbonyls	Standard curve	Correlation coefficient	RSD (%)
Formaldehyde	Y=39.5831554x+0.0945798	0.9999	0.31%
Acetaldehyde	Y=29.4118202x+0.311986	0.9999	0.27%
Acrolein+Acetone	Y=50.5652502x-0.1692096	0.9999	0.22%
Propionaldehyde	Y=23.0412714x-0.2702525	0.9999	0.23%
Crotonaldehyde	Y=20.9908197x+0.1257449	0.9999	0.19%
Methyl ethyl ketone	Y=22.2728907x-2.2690313	0.9991	0.28%
Methacrolein	Y=16.895953x+1.4477462	0.9995	0.29%
Butyraldehyde	Y=18.9919747x+0.6199411	0.9999	0.84%
Benzeldehyde	Y=13.3801106x-0.1091313	0.9999	0.14%
Valeraldehyde	Y=35.8235502x-0.0072466	0.9999	0.19%
Tolualdehyde	Y=12.9693126x-0.2582609	0.9999	0.31%
Cyclohexanone	Y=4.86750669x-0.0144752	0.9998	0.26%
hexanal	Y=13.1505299x-0.0447244	0.9999	0.16%

This discrepancy may be attributed to the different physiochemical properties of the test fuels. Above finding is consistent with that of Takada et al. [23] who reported the higher formaldehyde emissions at lower engine loads.

Although acetaldehyde shows a positive correlation with load in case of biodiesel and exhibits a decreasing trend with the increase in load, B20 and diesel on the other hand do not show a clear trend of brake specific emission of acetaldehyde. However, BSE of acetaldehyde shows maximum value at low load for all the test fuels. Above

Table 4. BSE of carbonyls from test fuels at different loads.

Carbonyles	D				B20				B100			
	Load (%)											
	10	50	75	100	10	50	75	100	10	50	75	100
Formaldehyde	48.36	41.53	34.14	28.18	59.15	38.99	27.66	30.73	62.21	48.36	40.72	35.94
Acetaldehyde	26.61	9.06	5.43	14.30	20.26	5.38	11.90	19.24	27.18	18.00	10.83	9.04
Acrolein+Acetone	6.93	8.64	2.51	4.53	10.42	4.15	5.70	3.31	1.22	6.16	12.63	10.11
Propionaldehyde	1.94	3.50	2.21	1.99	4.04	1.11	1.23	3.38	9.15	6.08	8.71	12.06
Crotonaldehyde	0.79	0.92	0.29	0.85	0.19	0.37	0.13	2.39	2.54	0.01	0.06	1.04
Methyl ethyl ketone	2.07	1.77	0.94	0.93	1.27	2.30	0.00	2.40	0.12	3.39	4.01	2.02
Methacrolein	1.70	1.20	1.65	0.31	0.05	0.02	0.08	0.38	4.69	3.05	3.00	5.06
Butyraldehyde	0.02	1.70	0.06	1.26	9.01	6.46	8.02	5.53	2.29	1.76	3.04	0.02
Benzeldehyde	0.41	0.70	0.61	0.40	0.00	0.20	0.01	0.99	0.16	0.00	0.00	0.01
Valeraldehyde	0.54	1.26	0.11	1.02	0.93	0.72	0.58	0.86	0.01	0.01	0.06	0.00
Tolualdehyde	1.34	0.80	0.29	0.45	0.03	0.00	0.01	0.00	0.00	0.08	0.00	0.04
Cyclohexanone	1.20	0.91	1.01	1.23	0.00	0.00	0.00	0.02	0.00	0.00	0.00	0.00
hexanal	0.00	0.58	0.00	0.35	0.14	0.32	0.12	0.41	0.03	0.44	0.15	0.06
Total	91.91	72.57	49.25	55.80	105.49	60.02	55.44	69.64	109.60	86.90	83.21	75.40
∑ Total	269.53				290.59				355.11			

finding is similar to that of Cheung et al. [24] who showed that acetaldehyde emissions were more at low load as compared to high loads. Similar kind of result was also reported by Pang et al. [17].

3.2. Effect of Biodiesel on BSE of Carbonyls

As listed in Tables 4 and 5, the BSE of formaldehyde, acetaldehyde, (acrolein + acetone), propionaldehyde, crotonaldehyde, Methyl ethyl ketone, and total carbonyls exhibit a strong correlation with the biodiesel content; and increase in the cases of B20 and B100. These results are not surprising and were expected because of the two main reasons. First, biodiesel used in the tests was produced from waste cooking oil; and was expected to contain appreciable amount of carbonyls because of oxidation during the frying of the meats. Second, biodiesel inheriting oxygen atoms is basically an ester mixture of saturated and non-saturated fatty acids which may include secondary oxidation products such as volatile and non-volatile carbonyl compounds, cyclic fatty acid monomers, and polymerization products [16].

The increase in formaldehyde and acetaldehyde is 2.8% and 2.5% respectively in case of B20, and 23% and 17% respectively in case of B100 as compared to commercial diesel. The increase in acetaldehyde from B20 compared with diesel is also supported by other literature [25-26]. Similarly, it has also been reported that formaldehyde, acetaldehyde, acetone, propionaldehyde, crotonaldehyde increase from B20, compared with diesel [4]. The increase in BSE of acrolein + acetone may be attributed to acrolein, which has mostly been produced by the oxidation of glycerol residues and other fatty acid residues present in the biodiesel, so its BSE increases in the cases of B100 and B20 as compared to diesel [16]. The BSE of total carbonyls from B20 and B100 is 8% and 32 % higher respectively than that of diesel fuel. This result is in good agreement with that of previous study [15].

The BSE of aromatic aldehydes (benzaldehyde and tolualdehyde) decreases in the cases of B100 and B20 as compared to diesel as shown in Tables 4 and 5 which is understandable because aromatic content in biodiesel is less than that of diesel. Corrêa and Arbilla [25] have also reported the decrease in benzaldehyde from biodiesel-diesel blend, compared with diesel.

3.3. Comparative Analysis of Different Carbonyls from Test Fuels

According to the experimental results listed in Tables 4 and 5, formaldehyde is the most abundant carbonyl of the test fuels. The BSE of the formaldehyde is 56.5%, 53.9%, and 52.7% in case of diesel, B20, and B100 respectively. After formaldehyde, the second largest percentage contributor to the total carbonyls is acetaldehyde with 20.6%, 19.5%, and 18.3% in case of diesel, B20, and B100 respectively. This finding is in consistent with that of previous study that formaldehyde and acetaldehyde are two major aldehydes species in the exhaust from vehicles [27].

It is interesting to note that BSE of formaldehyde and acetaldehyde are more from B20 and B100 compared with diesel as discussed earlier in section 3.2, however their percentage contribution to the total CC from the test fuels follow the order as D > B20 > B100. This enigma comes to an end very soon when brake specific emissions of total Mean carbonyls of the test fuels are viewed from their respective columns in the table 5, which are following the order as D < B20 < B100.

Acrolein+Acetone and propionaldehyde are the next major contributors to the total carbonyls, each of them contributing less than 10% of the total carbonyls. Other

carbonyls are minor contributors to the total carbonyls, and each of them is accounted for less than 4% in total carbonyls from the test fuels. Formaldehyde, acetaldehyde, acrolein + acetone, and propionaldehyde contribute 89%, 85%, and 89.6% of total carbonyls in case of diesel, B20, and B100 respectively. This result is similar to those of previous studies that 90% of aldehydes and ketones are made up of formaldehyde, acetaldehyde, acrolein, and propionaldehyde [4]. According to Grosjean et al. [27] formaldehyde, acetaldehyde, propionaldehyde, and acetone are the four largest emission factors of carbonyl emissions from vehicles.

3.4. Specific Reactivity of Carbonyls

Specific reactivity (SR) is defined as the milligram (mg) ozone potential per milligram non-methane organic gases (NMOG) emanated from the exhaust and can be evaluated as under [28]:

$$SR = \sum (NMOG_k \bullet MIR_k) / \sum NMOG_k \quad (1)$$

The subscript k represents the certain carbonyl specie; NMOG is the sum of non-methane hydrocarbons and oxygenates, including aldehydes; and MIR is the maximum incremental reactivity. Carter and Lowi [28] examined air modeling based on ozone forming reactivates of species and proposed the MIR factor as an index for ozone formation. This index indicates the maximum increase in ozone formation.

Table 5. Mean BSE of carbonyls from test fuels with their corresponding MIR values.

Carbonyls	Mean Brake Specific Emission (mg/kW•h)			MIR
	D	B20	B100	
Formaldehyde	38.05	39.13	46.81	7.15
Acetaldehyde	13.85	14.20	16.26	5.52
Acrolein+Acetone	5.65	5.90	7.53	6.77*, 0.56**
Propionaldehyde	2.41	2.44	9.00	6.53
Crotonaldehyde	0.71	0.77	0.91	5.41
Methyl ethyl ketone	1.43	1.49	2.39	1.18
Methacrolein	1.22	0.13	3.95	6.77
Butyraldehyde	0.76	7.26	1.78	5.26
Benzeldehyde	0.53	0.30	0.04	-0.56
Valeraldehyde	0.73	0.77	0.02	4.41
Tolualdehyde	0.72	0.01	0.03	-0.56
Cyclohexanone	1.09	0.01	0.00	6.53
hexanal	0.23	0.25	0.17	3.79
Total Mean BSE	*67.38*	*72.65*	*88.89*	
SR	6.39	6.38	6.51	

6.77* for Acrolein and 0.56** for Acetone

Table 5 shows the mean BSE of carbonyls from the three test fuels with their corresponding MIR values. It is elucidated from the table that the specific reactivity of carbonyls from the test fuels follow the order as B20 < D < B100. This result advocates the use of B20 as a promising alternative fuel in an unmodified diesel engine because its use reduces the ozone formation in the lower atmosphere. This reduction in ozone formation in the lower atmosphere is beneficial in reducing the respiratory problems. However, further research is required to fully understand the behavior of neat biodiesel for photochemical smog formation, especially when engine is unmodified.

4. Conclusions

The brake specific emissions of carbonyl compounds from diesel, neat biodiesel, and 20% biodiesel-diesel blend have been investigated in the present work. The followings are the main findings:

- At low load, formaldehyde and total carbonyls show maximum BSE from all the test fuels. This BSE decreases as the load increases. The BSE of acetaldehyde shows maximum value at low load for all the test fuels.
- The BSE of formaldehyde, acetaldehyde, acrolein + acetone, propionaldehyde, crotonaldehyde, Methyl ethyl ketone, and total carbonyls increase from B20 and B100, compared with diesel fuel. However, the BSE of aromatic aldehydes decreases in the cases of B100 and B20 as compared to commercial diesel.
- Formaldehyde is the most abundant carbonyl among the test fuels followed by acetaldehyde, Acrolein+Acetone, and propionaldehyde in the same order of magnitude and their sum contributes 89%, 85%, and 89.6% of the total carbonyls in the case of diesel, B20, and B100 respectively.
- Specific reactivity of carbonyl compounds from the test fuels follow the order B20 < D < B100.

Acknowledgements

The authors acknowledge the financial support of National key laboratory of Auto- performance and Emission Test, Beijing Institute of Technology (BIT)

Beijing, P.R China under National Natural Science Foundation Project No. 50576063.

References

[1] M.A. Kalam, M. Husnawan, H.H. Masjuki, "Exhaust emission and combustion evaluation of coconut oil-powered indirect injection diesel engine". Renewable Energy, Vol. 28, No. 15, 2003, 2405-2415.

[2] D. Haupt, K. Nord, K. Egeback, P. Ahlvic, "Hydrocarbons and aldehydes from a diesel engine running on ethanol and equipped with EGR, catalyst and DPF". Society of Auto motive Engineering (SAE) Technical Paper Series No. 2004-01-1882, 2004.

[3] J. Senda, N. Okui, T. Tsukamoto, H. Fujimoto, "On board measurement of engine performance and emissions in diesel vehicle operated with biodiesel fuel". Society of Auto motive Engineering (SAE) Technical Paper Series No. 2004-01-0083, 2004.

[4] L. Turrio-Baldassarri, C.L. Battistelli, L. Conti, R. Crebelli, B.D. Beradis, A.L. Iamiceli, M. Gambino, S. Iannaccone, "Emission comparison of urban bus engine fueled with diesel oil and biodiesel blend". Science of the Total Environment, Vol. 327, 2004, 147–162.

[5] A. Monyem, J.H. Gerpen, "The effect of biodiesel oxidation on engine performance and emission. Biomass Energy, Vol. 20, 2001, 317–325.

[6] L.C. Meher, D.V. Sagar, S.N. Naik, "Technical aspects of biodiesel production by transesterification -a review". Renewable and Sustainable Energy Reviews, Vol. 10, No. 3, 2006, 248–268.

[7] A.S. Ramadhas, S. Jayaraj, C. Muraleedharan, "Characterization and effect of using rubber seed oil as fuel in the compression ignition engines". Renewable Energy, Vol. 30, 2005, 795-803.

[8] Y.C. Lin, W.J. Lee, T.S. Wu, C.T. Wang, "Comparison of PAH and regulated harmful matter emissions from biodiesel blends and paraffinic fuel blends on engine accumulated mileage test". Fuel, Vol. 85, 2006, 2516-2523.

[9] J.F. McDonald, D.L. Purcell, B.T. McClure, D.B. Kittleson, "Emission characteristics of soy methyl ester fuels in an IDI compression ignition engine". Society of Auto motive Engineering (SAE) Technical Paper Series No. 950400, 1995.

[10] O. Schroder, J. Krahl, A. Munack, J. Bunger, "Environmental and health effects caused by the use of biodiesel". Society of Auto motive Engineering (SAE) Technical Paper Series No. 1999-1901-3561, 1999.

[11] A. Senatore, M. Cardone, V. Rocco, M.V. Prati, "A comparative analysis of combustion process in D.I. diesel engine fuelled with biodiesel and diesel fuel". Society of Auto motive Engineering (SAE) Technical Paper Series No. 2000-01-0691, 2000.

[12] D. Altiparmak, A. Deskin, A. Koca, M. Guru, "Alternative fuel properties of tall oil fatty acid methyl ester-diesel fuel blends". Bioresource Technology, Vol. 98, 2007, 241–246.

[13] N. Usta, "An experimental study on performance and exhaust emissions of a diesel engine fuelled with tobacco seed oil methyl ester". Energy Conversion and Management, Vol. 46, 2005, 2373–2386.

[14] H. Chao, G. Yunashan, T. Jianwei, H. Xiukun, "Spray properties of alternative fuels: A comparative analysis of biodiesel and diesel". International Journal of Energy Research, Vol. 32, 2008, 1329-1338.

[15] X. Pang, Y. Mu, J. Yuan, H. He, "Carbonyls emission from ethanol-diesel used in engines". Atmospheric Environment, Vol. 42, 2008, 1349-1358.

[16] L.L.N. Guarieiro, P.A.P. Pereira, E.A. Torres, G.O. Rocha, J.B. Andrade, "Carbonyl compounds emitted by a diesel engine fuelled with diesel and biodiesel-diesel blends: Sampling optimization and emissions profiles". Atmospheric Environment, Vol. 42, 2008, 8211-8218.

[17] X. Pang, X. Shi, Y. Mu, H. He, S. Shuai, H. Chen, R. Li, "Characteristics of carbonyl compounds emission from a diesel-engine using biodiesel-ethanol-diesel as fuel". Atmospheric Environment, Vol. 40, 2006, 7057-7065.

[18] [Y. Di, C.S. Cheung, Z. Huang, "Experimental investigation on regulated and unregulated emissions of a diesel engine fueled with ultra-low sulfur diesel fuel blended with biodiesel from waste cooking oil". Science of the Total Environment, Vol. 407, 2009, 835-846.

[19] X. Shi, X. Pang, Y. Mu, H. He, S. Shuai, J. Wang, H. Chen, R. Li, "Emission reduction potential of using ethanol-biodiesel-diesel fuel blend on a heavy duty diesel engine". Atmospheric Environment, Vol. 40, 2006, 2567-2574.

[20] US. Environment Protection Agency (US EPA), "Determination of formaldehyde in ambient air using adsorbent cartridge followed by high performance liquid chromatography (HPLC)". Compendium method TO-11A, 1999.

[21] M. Cardone, M.V. Prati, V. Rocco, M. Seggiani, A. Senatore, S. Vitolo, "Brassica carinata as an alternative oil crop for the production of biodiesel in Italy: engine performance and regulated and unregulated exhaust emissions". Environmental Science and Technology, Vol. 36, 2002, 4656-4662.

[22] R. Magnusson, C. Nilsson, B. Andersson, "Emissions of aldehydes and ketones from a two stroke engine using ethanol and ethanol-blended gasoline as fuel". Environmental Science and Technology, Vol. 36, 2002, 1656-1664.

[23] K. Takada, F. Yoshimura, Y. Ohga, J. Kusaka, Y. Daisho, "Experimental study on unregulated emission characteristics of turbocharged DI diesel engine with common rail fuel injection system". Society of Auto motive Engineering (SAE) Technical Paper Series No. 2003-01-3158, 2003.

[24] C.S. Cheung, Y. Di, Z. Huang, "Experimental investigation of regulated and unregulated emissions from a diesel engine fueled with ultralow-sulfur diesel fuel blended with ethanol and dodecanol". Atmospheric Environment, Vol. 42, 2008, 8843-8851.

[25] S.M. Corrêa, G. Arbilla, "Carbonyl emissions in diesel and biodiesel exhaust". Atmospheric Environment, Vol. 42, 2008, 769-775.

[26] N. Arapaki, E. Bakeas, G. Karavalakis, E. Tzirakis, S. Stournas, F. Zannikos, "Regulated and unregulated emissions characteristics of a diesel vehicle operating with diesel/biodiesel blends". Society of Auto motive Engineering (SAE) Technical Paper Series No. 2007-01-0071, 2007.

[27] D. Grosjean, E. Grosjean, A.W. Gertler, "On-road emissions of carbonyls from light-duty and heavy-duty vehicles". Environmental Science and Technology, Vol. 35, 2001, 45-53.

[28] W.P.L. Carte, A. Lowi, "A Method for Evaluating the Atmospheric Ozone Impact of Actual Vehicle Emissions". Society of Auto motive Engineering (SAE) Technical Paper Series No. 900710, 1990.

JJMIE

Volume 3, Number 2, January. 2009
ISSN 1995-6665
Pages 119 - 124

Jordan Journal of Mechanical and Industrial Engineering

Tire Skid Resistance on Contaminated Wet Pavements

W. R. Tyfour*

Department of Mechanical Engineering, Mu'tah University, Jordan

Abstract

An experimental test rig has been designed, fabricated, and used to study the effect of wet pavement contamination on the tire-pavement skid resistance. Results showed that although precipitation water reduces tire-pavement skid resistance, the presence of other contaminants plays a major role in further loss of this resistance. It has also been shown that the fractional constituents of pavement contaminants vary according to the vertical profile of the same road under the same traffic density. Traffic signal areas showed the lowest skid resistance when compared to other locations of the same road. Also, the skid resistance on a contaminated up-gradient was found to be lower than that of a contaminated down-gradient of the same traffic density. Among other contaminants, rubber particulates produced by tire wear appear to have minimal effect on the loss of tire-pavement skid resistance.

Keywords: Tire Skid Resistance; Pavement Contamination; Wet Pavement; Slippery Roads.

1. Introduction

Among other road surface conditions, slippery pavement during precipitation is of great concern to road safety authorities. Some statistics indicate that the number of accidents increases by up to two folds during rainy conditions [1-2].

Loss of skid resistance affects driver's ability to control vehicle. In addition to increasing the stopping distance while braking, lower skid resistance reduces steering controllability since both braking and steering depend on tire-pavement friction. This means that drivers need to change their driving habits when facing wet driving conditions. Some countries have realized the importance of educating drivers on how to act when facing slippery road conditions, such that they introduced the topic as a compulsory training course for new drivers [3]. It has been also realized that identifying spots with low skid resistance may help in reducing accidents [4].

Skid resistance is known to be a function of pavement construction materials [5-6], pavement roughness [7], and surface conditions [8]. As far as surface conditions are concerned, most of the work on wet pavement skid resistance appears to be dealing with the effect of the presence of precipitation water as a lubricant regardless of the other contaminants [9-11].

Pavement contaminants are expected to constitute of wear debris from pavement materials, pollutants from the surrounding environment, hydrocarbons leaking from motor vehicles, carbon particles, other vapors from the exhaust products, tire rubber wear particles, brake pads wear products, and metal wear debris produced by moving vehicle parts. Such diversity in the sources of pavement contaminants may lead to the assumption that the fractional amounts of these contaminants on any location is expected to vary according to the operating conditions. Vehicle speed, vehicle type, traffic density, surrounding environment, vehicle maintenance,etc are among the most influential in this regard.

In places where there are long periods between precipitations, the number of accidents increases during the first precipitation after a dry period. Then, with more precipitation, the number of accidents falls again. Eisenberg [11] has found that", if it rained a lot yesterday, then on average, today there are fewer crashes". His analysis also showed that " the risk imposed by precipitation increases dramatically as the time since last precipitation". These findings may indicate that the accumulation of pavement contaminants could be a suspect in loss of skid resistance.

The accumulation of pavement contaminants appears to be controlled mainly by the amount and repetition of precipitations. Many of these contaminants can be washed away during heavy rain.

The question which this work is trying to address is: What role do the pavement contaminants play in the tire-pavement skid resistance during precipitation? Also, do fractional amounts of these contaminants vary along vertical profile of the road such that it alters skid resistance?

2. Methodology

2.1. Experimental Set-Up

Since the aim of the work presented here is to compare the tire-pavement skid resistance under different wet contaminated pavement conditions, one may not be interested in obtaining absolute skid resistance numbers. In this case, comparison of the skid resistance under different contaminated contact conditions with the cases under dry

* *Corresponding author. tyfour@mutah.edu.jo*

.

contact may serve the purpose and give a good idea about the effect of different pavement contaminants.

A number of skid resistance evaluation devices can be used for this purpose. The British pendulum, which uses the loss of the potential energy of a swing pendulum as a skid resistance measure, is among the most widely used. However, for the experimental work presented here, and by use of the concept of the kinetic energy stored in a flywheel, a machine was proposed. If a flywheel is given a certain rotational speed via a power source, it stores a certain amount of kinetic energy depending on its mass, dimensions, geometry, and rotational speed. When the power is cut-off and the flywheel is kept rotating freely, its deceleration will totally depend on the frictional resistive torque. If this frictional torque is made to be that between the tire material and pavement, then deceleration of the flywheel will be a good measure for the skid resistance.

The proposed machine consisted of a flywheel connected via a shaft with a splined sliding joint to a variable speed gear box powered by an AC motor. Two sprockets and a drive chain connect the gear box output shaft to the top of the flywheel shaft. A unidirectional clutch fitted on the flywheel shaft ensures that the fly wheel is driven by the motor in such a way that when the power is cut off, the flywheel continues rotating due to its inertia only. The sliding joints ensure continuous contact between the flywheel and the pavement, and at the same time it guarantees that the normal force on the flywheel is constant, and it is limited to the weights of the flywheel itself and the lower part of the sliding joint. Three 5x5 cm ungrooved rubber pads, cut from tire material, are equally spaced and are secured to outer most radius of the bottom surface of the flywheel to form the contact between the tire material and the pavement.. Figure 1 is a schematic illustration of the machine.

The rotational speed of the flywheel is measured using a tachometer, whose signal is stored in a storage oscilloscope. The stored signal represents the velocity history of the flywheel speed from start to stop, from which deceleration of the flywheel during the free rotation is caused by the resistive frictional torque, and it can be calculated.

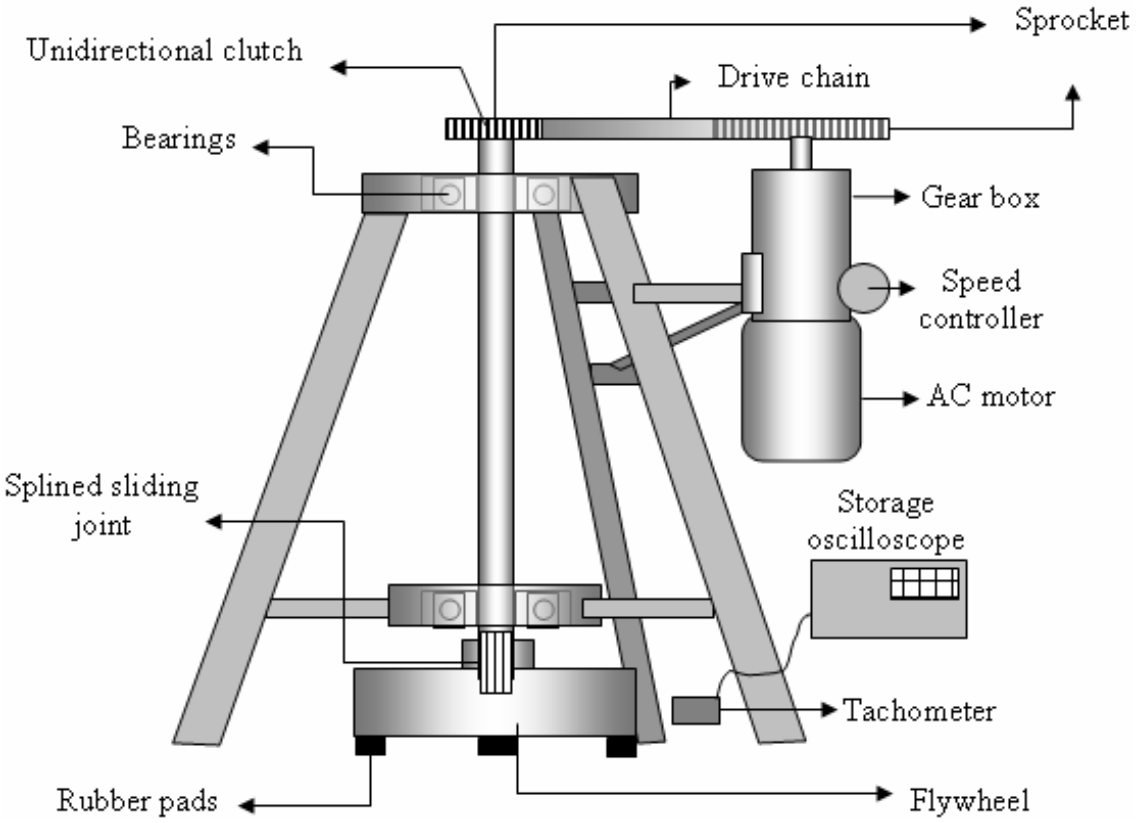

Figure 1. Schematic illustration of the skid resistance testing machine.

2.2. Test Procedure

A pavement of around one squared meter is vacuum-cleaned, washed, and dried before each test. Since all tests are carried out on this same spot of the pavement. Pavement material and surface parameters of the pavement will not be of importance as results are comparative. The flywheel is placed on the pavement such that the three rubber pads are in contact with the cleaned area. Motor is started, and fly wheel is given the required rotational speed using the speed controller. Once the required speed is reached, the motor is stopped to allow the flywheel to decelerate, driven by its inertia and resisted mainly by the frictional torque between the pavement and the rubber pads. The contribution of bearing friction in this case can be considered negligible compared to pad-pavement friction Tests with different contact contamination conditions are performed by applying the contaminants to the contact area as described later.

2.3. Samples of Contaminants

During first precipitation of winter season, after a dry period of five months, and before roads are washed by rain water. A vacuum cleaner is used to collect wet samples

from a certain paved road. The samples are kept in sealed glass containers for further testing. No attempt has been made to know the exact composition of the samples.

For the purpose of this study and to ensure the same traffic density, amount of rain, operating conditions, and three different locations on the same one-way road were selected. The selected road profile consisted of a 3% down gradient length, followed by a level stretch with a traffic signal, then a 3% up gradient stretch. Since it is a one way road, the same amount of traffic passes the three locations. Figure 2 is a schematic illustration of the three sample collection locations.

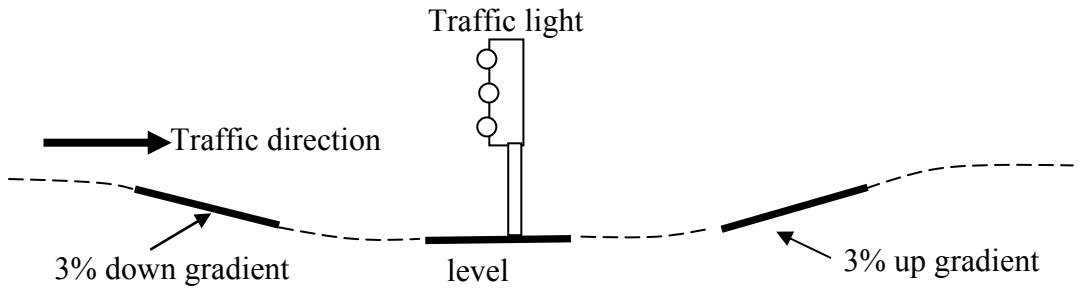

Figure 2.The vertical profile of the contaminated sample collection locations.

2.4. Test Schedule

In addition to clean dry pavement contact condition, testes were carried out on three other categories according to the contaminant type as tabulated in table (1)

Table 1. Test schedule.

Category	Contact contaminant
A	None (clean and dry)
B	Tap water on clean pavement
C	Wet contaminants collected from the three location described above
D	Artificial wet contaminants

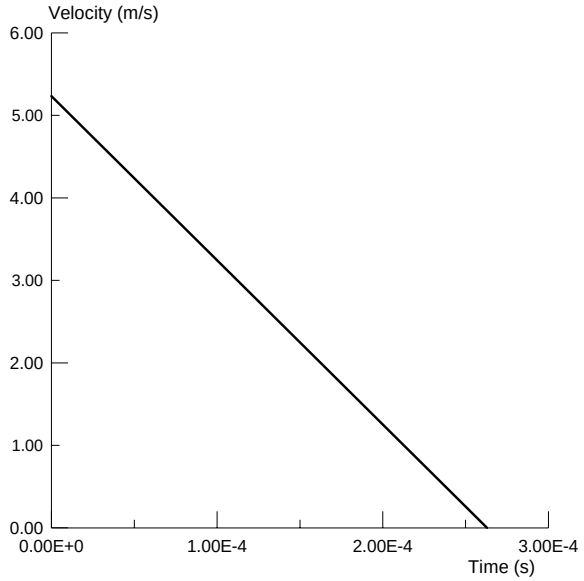

Figure 3. Time- velocity relationship for the dry contact condition.

The amount of contaminant used in this case is classified according to the quantity supplied to the contact area as mist, drizzle, and flood. Mist means that the amount of contaminant is just enough to wet the pavement surface without filling the pavement rough cavities whereas drizzle supply fills many of the cavities, but not enough to leak out. Finally, the flood contact floods the contact area to levels above the pavement cavities.

3. Test Results

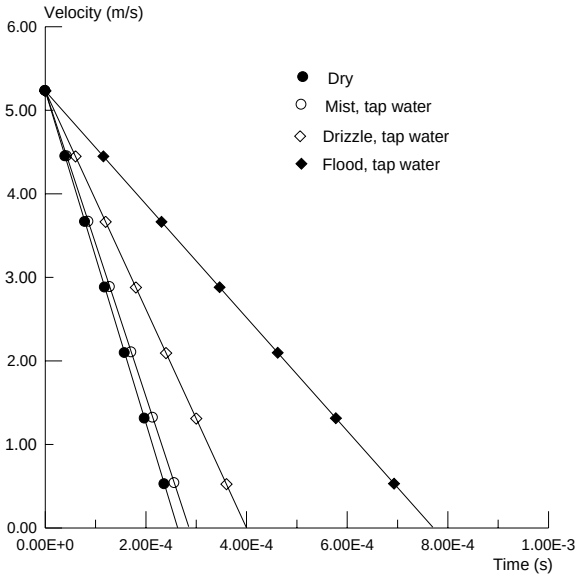

Figure 4.Time-velocity relationship for dry and wet contact conditions.

3.1. Dry, Clean Pavement

The time-velocity relationship under0 dry clean pavement condition is shown in Figure (3). The initial free rotational speed of the flywheel was 5.334 m/s. In this case, the slope of the plot represents the deceleration in m/s^2. This deceleration will be used as a measure of skid resistance. Since this test represents a non-contaminated condition, its results will be used as a reference for comparison purposes.

3.2. Tap Water on Clean Pavement

Figure 4 shows the time-velocity relationship for three cases in which tap water was used as the only contaminant. The only variable in the three tests is the

amount of tap water supplied to the contact area as described earlier. For comparison purposes, the dry pavement test results are also shown on the same plot.

It is evident that all the three water contaminated conditions show a lower skid resistance (higher deceleration compared to the dry contact). The lowest skid resistance is the one under flooded pavement contact condition, whereas mist contamination shows minimal effect on skid resistance when compared to the dry contact.

The decelerations for the three cases are related to that of the dry case, i.e. normalized, and shown in the bar chart of Figure 5. If this normalized deceleration is termed Normalized Skid Resistance (NSR), then the NSR becomes unity for the dry contact, 0.86 and 0.66 for mist and drizzle contamination conditions, respectively, whereas NSR is drastically reduced to only around 0.34 for the flooded contact condition.

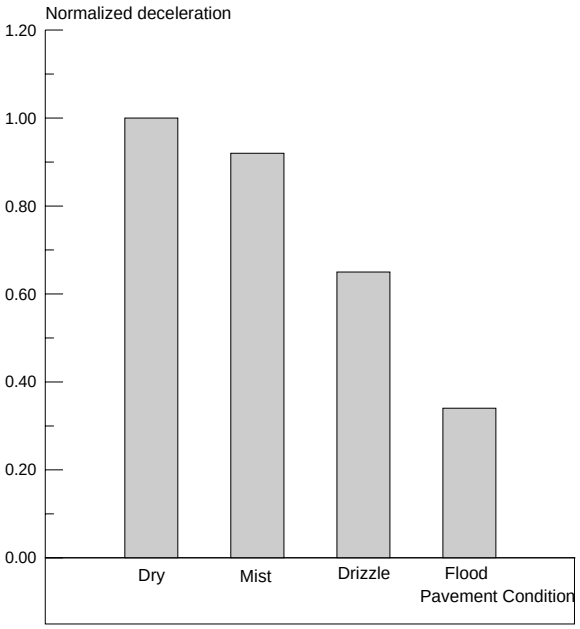

Figure 5. Normalized skid resistance as a function of different wet contact conditions.

3.3. Naturally Wet Contaminated Pavement

Three tests, using the three wet contaminated sample collected from the three locations, as described earlier, were conducted under drizzle supply. The drizzle supply was selected since it represents the operating conditions on the road, where the contaminants are neither washed out by flood, nor fully mixed with water during mist rain. Test results for this category are shown in Figure 6 as a time-velocity relationships along with that for the dry pavement condition.

The figure reveals different decelerations depending on the location where the contaminant sample was collected. The lowest skid resistance is obtained for the contact contaminant collected from traffic signal area. Also, the skid resistance for the up-gradient sample is much higher than that for the sample collected from the down-gradient area. These differences are better illustrated in figure 7, which shows the normalized skid resistance (NSR) for the three cases, and compared to that of the dry contact case.

The above figure shows that the NSR drops from unity for the dry contact to near 0.58 for the down-gradient

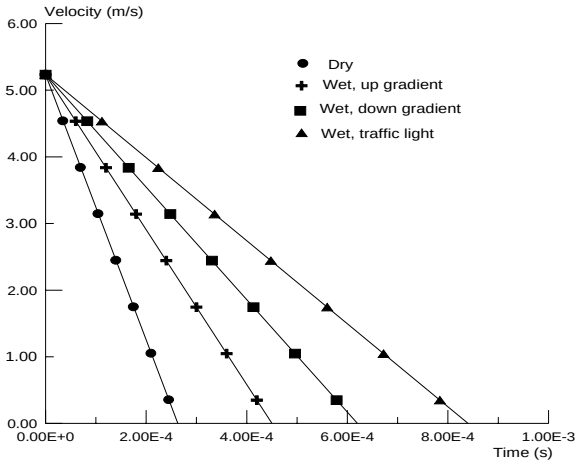

Figure 6. Time-velocity relationship for the different wet contamination contact conditions

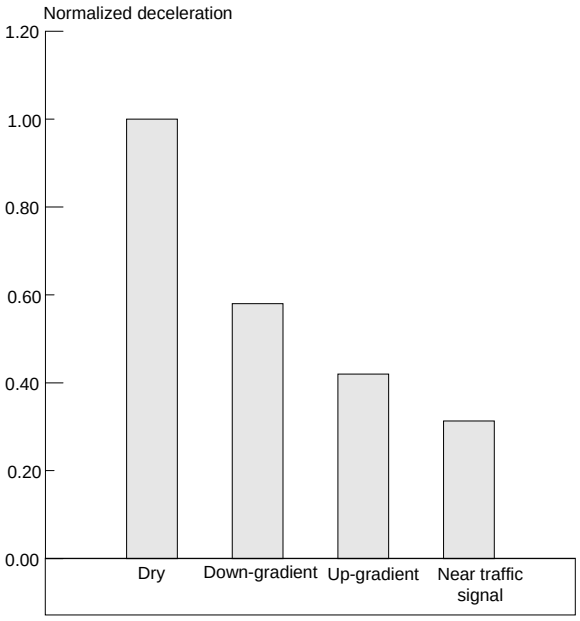

Figure 7. Normalized skid resistance under contact conditions of road contaminants collected from different locations.

contaminant contact, and to 0.42 for the up-gradient contaminant. The minimum NSR is obtained for the contaminant collected from the area near the traffic signal. These differences will be discussed in the sections to follow.

3.4. Pavement with Artificial Contaminants

Although the exact composition of the samples collected from the road is not known, it is expected that these samples may contain dust, fine particles of brake pads, rubber dust from tires, oil and other hydrocarbons, and fine metallic particles from wearing mechanical parts. In this case, the contribution these constituents in the loss of skid resistance may need to be known. Therefore, this effect could be better investigated by mixing one artificially prepared contaminant with water. Three artificially contaminated samples, containing silica dust, rubber dust, and cutting fluid, were prepared. The volumetric concentration of the two slid contaminants in the clean tap water was selected arbitrarily at 3%. The size of the silica dust and rubber dust particles was greater than

0 and less than 200 microns. The cutting fluid used was the mineral oil based type emulsion with 3:100 oil to water ratio. All the artificially contaminated samples were supplied as drizzle to the contact area.

Time- velocity relationships under the three artificially contaminated samples are shown in Figure 8. For comparison, the figure also includes the results for dry contact as well as that with uncontaminated tap water condition.

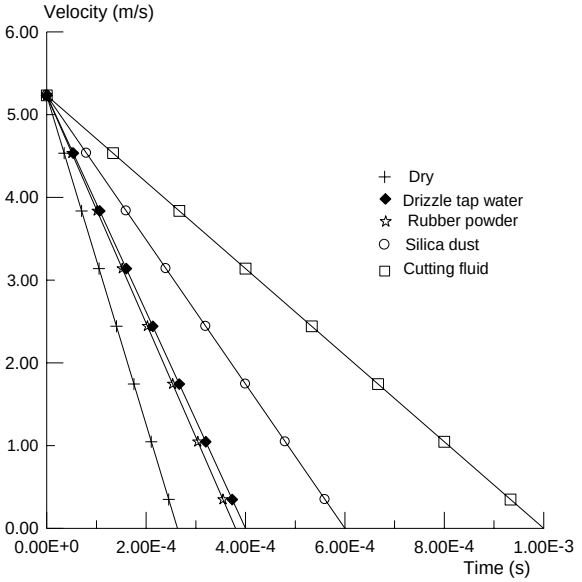

Figure 8. Time-velocity relationship under conditions of different artificially prepared contaminants.

The same results are shown in Figure 9 in the form of a bar chart where NSR is shown as a function of the type of the artificial contaminant.

The bar chart reveals that the pavement contamination with only rubber powder has almost no effect on the NSR. The NSR is 0.650 for uncontaminated tap water contact and 0.657 for rubber powder contaminated contact. But, a significant drop in the NSR is associated with the contact contaminated with oil-water mixture. Furthermore, the effect of dust, as a contaminant, in reducing the skid resistance is noticeable.

4. Discussion

The test program used in this study compares the normalized skid resistance NSR for different contaminated pavement conditions. The NSR of the dry pavement contact condition has been used as a reference since it represents the favorable contact condition.

The effect of other factors on the skid resistance is neutralized by conducting the experiments on the same spot of the pavement. In this case, the effect of pavement construction material and pavement surface roughness is isolated. Cleaning and drying of the test spot before each test guarantees that no residual contaminants remained from previous tests.

4.1. Tap Water On Clean Pavement

As expected, all wet contact conditions gave lower skid resistance when compared to the dry contact. However, the difference in skid resistance of the three tests under tap water contact of different supplies can be explained by

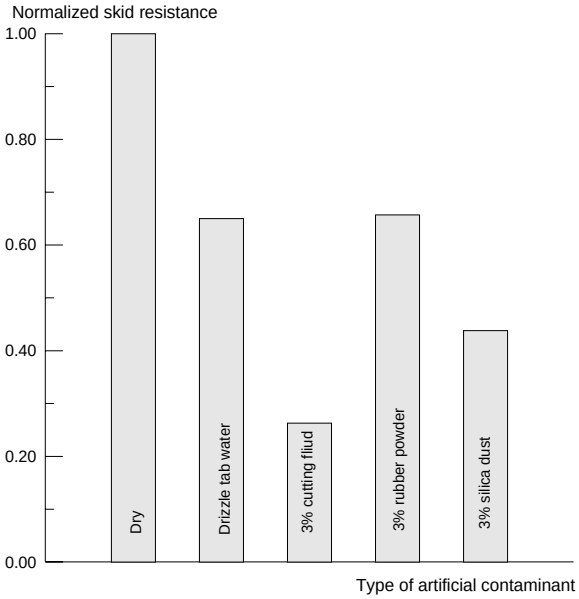

Figure 9. Normalized skid resistance for artificially prepared contaminants .

arguing that mist supply can not provide a thick lubrication film compared to the pavement roughness. In this case, no hydrodynamic action is possible. This may explain why the NSR for the mist contact does not drop significantly but rather recorded 86% of that of the dry contact. On the other hand, it can be noticed that the flood supply has a drastic effect on the skid resistance, where the NSR has dropped to 26% of that of the dry contact. This can be explained by arguing that the amount of water was enough to cause hydrodynamic lubrication. However, the result may appear contradictory to what drivers experience on flooded roads. The difference is the absence of other pavement contaminant, and that the rubber pads used during the tests were not grooved. Tire grooving allows water to escape from the tire-pavement contact area, and as a result prevents the hydrodynamic action between real vehicle tires and flooded pavements [12]. Furthermore, most of pavement contaminants are washed away by flood rain.

4.2. Naturally Wet Contaminated Pavement

The samples in this case were collected from three locations on the same road as described in section 3.3. Time of sample collection was during the first precipitation following a 5-month-dry period. To ensure same water content, the three samples were collected simultaneously but before flooding pavement.. As mentioned earlier, flood rain may washout the contaminants such that the samples may end up containing water only. Furthermore, accidents rates and severity are known to be higher during the first precipitation following a dry period [11]. This may explain why the three tests of this category were conducted under drizzle contact conditions.

The results described in section 3.3 and Figures 7 and Figure 8 indicate three different skid resistances. The sample collected from the traffic signal area caused maximum drop in the NSR, from 1 for dry contact to 0.31 for the contaminated sample. The samples collected from the up and down gradients showed 0.58 and 0.42 NSR, respectively. It can be concluded that contaminant content

in the three samples may be different. The area near the traffic signal is expected to have higher contamination contents, mainly hydrocarbon, since many cars stop at the red signal for awhile. If there are leaks of fuel, oils and/or other materials, the share of a unit area of these leaks will be higher on the stop area. Whereas the same amount of leaks is distributed on a much larger area if the vehicle is traveling, depending on the vehicle speed. Furthermore, brake pads and tire rubber residuals are also expected to be higher near traffic signal due to the high number of start-stops in such locations. In addition, some internal combustion engine faults like worn intake and exhaust valves are known to produce oil vapor and oil combustion products during the first acceleration following an idle stop.

As far as the up and down gradient samples are concerned, the NSRs, as seen in Figure (7), are 0.42 and 0.58, respectively. The difference in this case may indicate different contaminants, attributed to the different operating conditions. On down gradient, speed is controlled by lower gear ratios and/or brake applications. In this case, engine is not loaded. Whereas in up-gradient, vehicles climb on throttle causing more exhaust residuals. Furthermore, speed is expected to be lower on the up gradient. This means that contaminants related to lower speed and higher engine loading are higher on the up gradient, whereas brake pad residuals are less.

4.3. Artificially Contaminated Wet Pavement

The set of tests described in section 3.4 aimed at examining the effect of the different contaminants in lowering skid resistance. Being wet tests, all gave lower NSR compared to the dry contact. However, if the effect of the contaminant is to be assessed, it is the comparison between the wet-uncontaminated and the wet-contaminated which is significant.

The test with 3% cutting fluid in water gave the lowest NSR. This finding is in agreement with the argument that the area near traffic signal contains higher concentration of oily products. The result of the test of rubber–water contamination is in an agreement with the finding of Chiu [6] despite the fact that his findings are for rubber mixed in the pavement construction materials rather than being a contaminant on the pavement surface as in the case of this study.

5. Conclusions

- Although pavement contamination with water alone reduces tire-pavement skid resistance, other pavement contaminants play an important rule in further deterioration of this resistance
- The fractional content of the different pavement contaminants on a certain road having same traffic density changes according to the vertical profile (up gradient or down gradient). As a result, the skid resistance along this profile changes accordingly
- Traffic signal areas are the most dangerous spots with regard to loss of skid resistance, when compared to up and down gradient spots of the same road and traffic density.
- Tire wear debris (rubber particulates), as a pavement contaminant, has no significant effect on the loss of tire-wet pavement skid resistance
- Pavement contaminated with dust particulates mixed with rain water has a lower tire-pavement skid resistance when compared to pavement contaminated with water only

Acknowledgement

The author would like to thank Traffic Department /Jordan for their support and for helping in securing sites for sample collection.

References

[1] H. Brodsky, A.S. Hakkert, “Risk of a road accident in rainy weather”. Crash Anal. Prev., Vol. 202, 1988, 161–176.
[2] M. Andreescu, D.B. Frost, “Weather and traffic accidents in Montreal, Canada”. Climate Res., Vol. 9, 1998, 225–230.
[3] K. Ari, K. Esko, H. Mika, L. Sirkku, “Does increased confidence among novice drivers imply a decrease in safety? The effects of skid training on slippery road accidents”. Accident Analysis & Prevention, Vol. 36, No. 4, 2004, 543-550.
[4] H.P. Lindenmann, “New findings regarding the significance of pavement skid resistance for road safety on Swiss freeways”. Journal of Safety Research, Vol. 37, No. 4, 2006, 395-400.
[5] I.M. Asi, “Evaluating skid resistance of different asphalt concrete mixes”. Building and Environment, Vol. 42, No 1, 2007, 325-329.
[6] C. Chiu, “Use of ground tire rubber in asphalt pavements: Field trial and evaluation in Taiwan”. Resources, Conservation and Recycling, Vol. 52, No 3, 2008, 522-532.
[7] A. Slimane, M. Khoudeir, J. Brochard, M. Tan, “Do Characterization of road microtexture by means of image analysis”. Wear, Vol. 264, No 5-6, 2008, 464-468.
[8] G. Alexandros, O.K. Panagouli, “Fractal evaluation of pavement skid resistance variations”. I: Surface Wetting, Chaos, Solitons, & Fractals, Vol. 9, No. 11, 1998, 1875-1890.
[9] D. L. Ivey, L.I. Griffin, T.M. Newton, R.L. Lytton, K.C. Hankins, “Predicting wet weather accidents”. Accident Analysis & Prevention, Vol. 13, No. 2, 1981, 83-99.
[10] J. Andrey, S. Yagar, “A temporal analysis of rain-related crash risk”. Crash Anal. Prev. Vol. 254, 1993, 465–472.
[11] D. Eisenberg, “The mixed effects of precipitation on traffic crashes”. Accident Analysis & Prevention, Vol.36, No.4, 2004, 637-647.
[12] K.B. Wallace, D.H. Trollope, “Water pressure beneath a skidding tyre”. Wear, Vol.13, No. 2, 1969, 109-118.

JJMIE

Volume 3, Number 2, June. 2009
ISSN 1995-6665
Pages 125 - 130

Jordan Journal of Mechanical and Industrial Engineering

Performance and Emission of Acetylene-Aspirated Diesel Engine

T.Lakshmanan [a,*], G.Nagarajan [b]

[a] Department of Mechanical Engineering, Rajarajeswari Engineering College, Adayalampattu, Chennai – 600095, 91 09840154392,

[b] Internal combustion engineering Division College of Engineering, Anna University, Chennai – 600025 India

Abstract

Studies reveal that acetylene gas produced from lime stone ($CaCO_3$) is renewable in nature and exhibits similar properties to those of hydrogen. In the present work, experimental investigation has been carried out on a single cylinder, direct injection, and compression ignition engine run on dual fuel mode with diesel as an injected primary fuel and acetylene inducted as secondary gaseous fuel to obtain data on engine performance and exhaust emissions. Fixed quantity of acetylene was aspirated, and readings were taken at various loads. Dual fuel operation resulted in lesser thermal efficiency when compared to neat diesel operation. Acetylene aspiration reduces smoke, soot formation, and exhaust temperature; and increases NOx emission. The emission of carbon mono oxide and carbon dioxide was lower under all operating conditions when compared to diesel operation.

Keywords: Dual Fuel Engine; Aspiration; Ignition Delay

1. Introduuction

In the present context, the world is confronted with the twin crisis of fossil fuel depletion and environmental degradation. Conventional hydrocarbon fuels used by internal combustion engines, which continue to dominate many fields like transportation, agriculture, and power generation leads to pollutants like HC (hydrocarbons), SOx (sulphur oxides), and particulates which are highly harmful to human health [1-2]. CO_2 from Greenhouse gas increases global warming. This crisis has stimulated active research interest in non-petroleum, a renewable and non-polluting fuel, which has to promise a harmonious correlation with sustainable development, energy conservation, efficiency, and environmental preservation.

Promising alternate fuels for internal combustion engines are natural gas, liquefied petroleum gas (LPG), hydrogen, acetylene, producer gas, alcohols, and vegetable oils. Among these fuels, there has been a considerable effort in the world to develop and introduce alternative gaseous fuels to replace conventional fuel by partial replacement or by total replacement. Many of the gaseous fuels can be obtained from renewable sources. They have a high self-ignition temperature; and hence are excellent spark ignition engine fuels. They cannot be used directly in diesel engines.

However, Diesel engines can be made to use a considerable amount of gaseous fuels in dual fuel mode without incorporating any major changes in engine construction. It is possible to trace the origin of the dual fuel engines to Rudolf Diesel, who patented an engine running on essentially the dual-fuel principle. Here gaseous fuel called primary fuel is either inducted along with air intake, or injected directly into the cylinder and compressed, but does not auto-ignite due to its very high self-ignition temperature. Ignition of homogeneous mixture of air and gas is achieved by timed injection of small quantity of diesel called pilot fuel near the end of the compression stroke. The pilot diesel fuel auto-ignites first and acts as a deliberate source of ignition for the primary fuel air mixture. The combustion of gaseous fuel occurs by flame propagation similar to SI engine combustion. Thus dual fuel engine combines the features of both SI and CI engine in a complex manner. The dual fuel mode of operation leads to smoother operation; lower smoke emission and the thermal efficiency are almost comparable to the diesel version at medium and at high loads. However, major drawback with these engines are higher NO*x* emissions, poor part load performance, and higher ignition delay with certain gases like biogas and rough engine operation near full load due to high rate of combustion [3].

Karim [4] has done extensive research to understand the nature of the combustion process in the dual fuel. He has used variety of gases like methane, ethane, propane, butane, hydrogen, ethylene, and acetylene as primary fuel. It is generally accepted that performance of dual fuel engines, irrespective of the type of gaseous fuel employed, is better at medium and high loads. However, it has been reported that at low outputs efficiency is slightly inferior to the base line diesel engine. Researchers have stressed the need to control the quantity of both pilot and gaseous fuel depending on load conditions for better performance.

* Corresponding author. Lux.bharani@gmail.com

Haragopala Rao et al. [5] investigated performance of diesel engine in dual fuel mode by inducting small quantity of hydrogen diesel. At higher loads, the efficiencies attained are close to diesel with notable reduction in smoke, soot formation, and exhaust temperature. NOx emissions are increased with increase in peak pressure.

Gunea, Razavi, and Karim [6] conducted experiments on a four-stroke, single cylinder, direct injection diesel engine fueled with natural gas. Tests were conducted with diesel as the pilot fuel having different cetane numbers in order to find the effects of pilot fuel quality on ignition delay. They concluded that ignition delay of a dual fuel engine mainly depends on pilot fuel quantity and quality. High cetane number pilot fuels can be used to improve performance of engines using low cetane value gaseous fuel.

Das [7] suggested that hydrogen could be used in both SI engine and CI engine without any major modification in the existing system. He studied different modes of hydrogen induction by carburetion, continuous manifold injection (CMI), timed manifold injection (TMI), low pressure direct injection (LPDI), and high pressure direct injection (HPDI); and suggested to use manifold injection method for induction of gases to avoid undesirable combustion phenomenon (back fire) and rapid rate of pressure rise.

Wulff et al. [8] used mixture of acetylene and alcohol to burn in spark ignition engine and in compression ignition engine in a controllable way in dual fuel mode. It exhibited higher efficiency than conventional engine, with cleaner burning better than that of fossil fuels. The combustion was under lower temperature, and this prolonged the life expectancy of the engine.

Ashok Kumar et al. [9] studied suitability of acetylene in SI engine along with EGR, and reported that emission got drastically reduced on par with hydrogen engine with marginal increase in thermal efficiency.

Swami Nathan et al. [10] had conducted experiment in CI engine by using acetylene as a fuel in HCCI mode along with preheated take charge heating. The efficiencies achieved were very near to diesel. NO*x* and smoke level were reduced drastically. However, HC level was increased.

2. Acetylene Production and Properties

Acetylene is chosen as an alternative fuel in the present study. Since it is renewable in nature, it seems to posses similar properties of hydrogen (table 1) and can be used as an alternative fuel in internal combustion engines in competition with hydrogen fuel. Acetylene was discovered in 1836 in England by E.Davy. It is a colorless gas with a garlic smell produced from calcium carbonate (lime stone), which is abundant and renewable in nature in a lime kiln at 825^{o}C which yields calcium oxide (lime) by liberating CO_2. Calcium oxide is heated along with coke in electric furnace to produce calcium carbide. Finally calcium carbide is hydrolyzed to liberate acetylene.

Acetylene has a very wide flammability range, and minimum ignition energy is required for ignition since the engine can run in lean mode with higher specific heat ratios leading to increased thermal efficiency. It has higher flame speed and hence faster energy release. And at stoichiometeric mixtures, acetylene engines could closely approach thermodynamically ideal engine cycle. High self-ignition temperature of acetylene allows larger compression ratios than diesel engines do. Due to lower quenching distance similar to hydrogen, flame cannot be quenched easily in the combustion chamber. Due to lower ignition energy, high flame speed, wide flammability limits, and short quenching distance lead to premature ignition and also lead to undesirable combustion phenomenon called knock, the primary problems that have to be encountered in operation of acetylene engines.

Table 1. Physical and Combustion Properties of fuels.

Properties	Acetylene	Hydrogen	Diesel
Formula	C_2H_2	H_2	$C_8 - C_{20}$
Density kg/m^3 (At 1 atm & 20 ^{o}C)	1.092	0.08	840
Auto ignition temperature (^{o}C)	305	572	257
Stoichiometeric air fuel ratio, (kg/kg)	13.2	34.3	14.5
Flammability Limits (Volume %)	2.5 – 81	4 – 74.5	0.6 – 5.5
Flammability Limits (Equivalent ratio)	0.3 – 9.6	0.1 – 6.9	------
Lower Calorific Value (kJ/kg)	48,225	1,20,000	42,500
Lower Calorific Value (kJ/m^3)	50,636	9600	-------
Max deflagration speed (m/sec)	1.5	3.5	0.3
Ignition energy (MJ)	0.019	0.02	--------
Lower Heating value of Stoichiometeric mixture (kJ/kg)	3396	3399	2930

In the present work, a single cylinder, direct injection air, and cooled diesel engine were modified to work in the dual fuel mode with acetylene as the secondary inducted fuel and diesel as the primary injected fuel. The performance and emission at different output with fixed quantity of aspirating acetylene are presented in this work.

3. Experimental Setup and Methodology

A single cylinder four stroke air cooled naturally aspirated direct injection diesel engine developing 4.4 kW at 1500 rpm, fueled with diesel fuel was utilized for acetylene dual fuel operation. The specifications of the engine are given in table 2. A Schematic of the experimental arrangement is shown in Figure 1.

Acetylene was introduced into intake manifold at a point closer to the intake valve by a non-return valve arrangement through a flame trap. The flow of acetylene was controlled by needle valve and was measured by a calibrated gas flow meter. Air flow was determined by measuring the pressure drop accurately across a sharp edge orifice of the air surge chamber with the help of a manometer. The diesel flow was measured by noting the time of fixed volume of diesel consumed by the engine. A water-cooled piezoelectric pressure transducer was fixed on the cylinder head to record the pressure variation on the screen of a cathode –ray oscilloscope along with crank angle encoder. Chromel-alumel K-type thermocouple was used for exhaust gas temperature measurement. The exhaust gas constituents CO, CO_2, HC, NO*x*, and smoke were measured by a Qurotech QRO-401 gas analyzer, and Bosch smoke meter was used for the measurement of smoke.

Table 2. Engine Specification.

Make and model	Kirloskar, TAF 1
Type	4 stroke , air cooled
General details	Four stroke, compression ignition, direct injection
Bore/stroke	87.5 mm/110 mm
Compression ratio	17.5:1
Type of combustion chamber	Hemispherical open combustion chamber
Rated output	4.4 kW at 1500 rpm
Injection timing and injection pressure	23 ^{o}C btdc and 200 bar

The engine was started using diesel fuel; and was allowed to warm up. Acetylene fuel was then supplied into intake manifold at fixed flow rate of 3lpm through a gas flow meter, which is at equivalence of 0.13 ratio. The load on the engine was increased. The quantity of injected diesel fuel was automatically varied by the governor attached to it, which maintains the engine speed at 1500 rpm throughout the experiment.

4. Error Analysis

Errors and uncertainties in the experiments may result from instrument selection, condition, calibration, environment, observation, reading, and test planning. Uncertainty analysis is needed to prove the accuracy of the experiments. An uncertainty analysis was performed using the method described by J.P. Holman [11].

Percentage uncertainties of various parameters like total fuel consumption, brake power; specific fuel consumption, and brake thermal efficiency were calculated using the percentage uncertainties of various instruments given in Table 3.

Total percentage uncertainty of this experiment == Square root of{(uncertainty of TFC)^2 +(uncertainty of brake power)^2 +(uncertainty of specific fuel consumption)^2 +(uncertainty of brake thermal efficiency)^2 +(uncertainty of CO)^2 +(uncertainty of CO_2)^2 +(uncertainty of unburned hydrocarbon)^2 +(uncertainty of NO*x*)^2 +(uncertainty of smoke number)^2 +(uncertainty of Exhaust gas temperature)^2 +(uncertainty of pressure pickup)^2}

Total percentage uncertainty of this experiment = square root of $\{(1)^2 + (0.2)^2 + (1)^2 + (1)^2 + (0.2)^2 + (0.15)^2 + (0.2)^2 + (0.2)^2 + (1)^2 + (0.15)^2 + (1)^2\} = \pm 3$ %

Using the calculation procedure, the total uncertainty for the whole experiment is obtained to be ± 3 %.

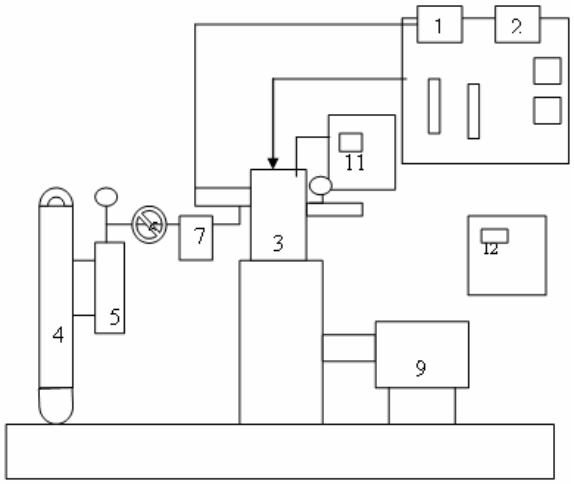

LEGENDS.
1. Air flow meter , 2. Diesel fuel tank ,3. Diesel engine
4. Acetylene generator, 5. Flame trap , 6. Flow control valve
7. Gas flow meter , 8. Intake manifold , 9. Dynamometer.
10. Control panel , 11.Oscilloscope, 12.Gas analyser.
Figure 1 Schematic of the experimental setup.

5. Result and Discussion

In the present work, acetylene gas was aspirated in the intake manifold in CI engine with diesel being the ignition source. The performance and emission characteristics are compared with baseline diesel operation.

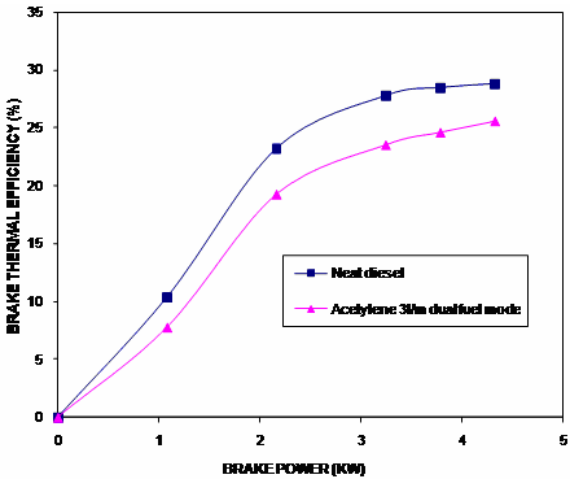

Figure 2. Variation of brake thermal efficiency with brake power.

5.1. Brake Thermal Efficiency

The variation of brake thermal efficiency with brake power is shown in figure 2.The brake thermal efficiency in induction technique is found to be 11.23% lower, when compared with neat diesel fuel of 28.84% efficiency at full load. In general, it may be noted that in the dual-fuel engines, the thermal efficiency decreases at low loads and

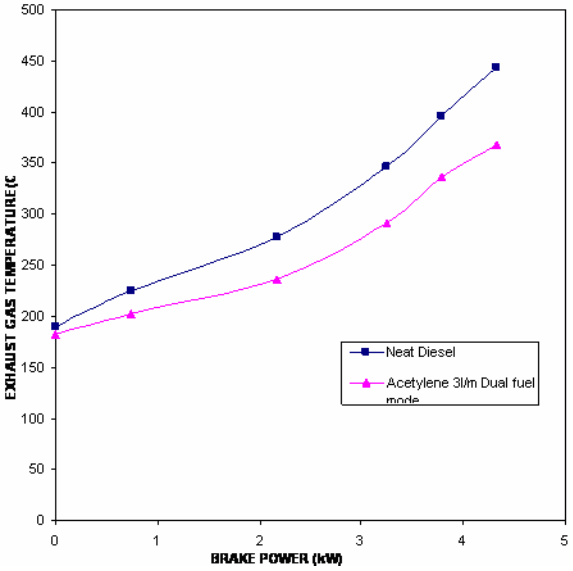

Figure 3. Variation of exhaust gas temperature with brake power.

increases above the base line at full load operation with addition of inducted fuels like LPG, CNG etc., [3]. However, acetylene, because of its wide flammability limit and high combustion rate, is an exception where efficiency is lower throughout the load spectrum. With high loads, the brake thermal efficiency falls because of high diffusion rate and faster energy release .This confirms that faster energy release occurs with acetylene introduction; and is also supported by the observed increase in maximum cycle pressure.

At partial loads with a small quantity of injected fuel, the flame fronts propagating from ignition centers do not extend to all the regions of the combustion chamber and leaves some of the homogeneously dispersed acetylene unburnt, causing low thermal efficiency at low loads.

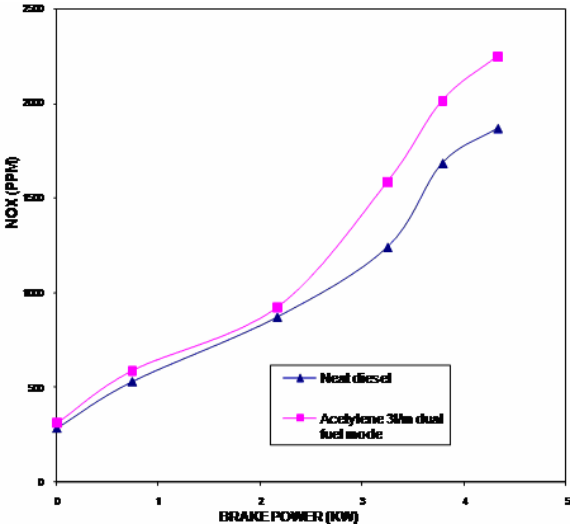

Figure 4. Variation of NO*x* with brake power.

5.2. Exhaust Gas Temperature

The exhaust gas temperature at full load, depicted in figure 3, reaches 368°C in acetylene induction technique and 444°C in the case of base line diesel operation. Acetylene induction decreased the exhaust gas temperature at all loads, indicating the advancement of energy release in the cycle and higher flame speed. Cylinder pressure diagram confirmed this, in which maximum pressure was observed to occur earlier in the cycle when acetylene was introduced along with the intake air.

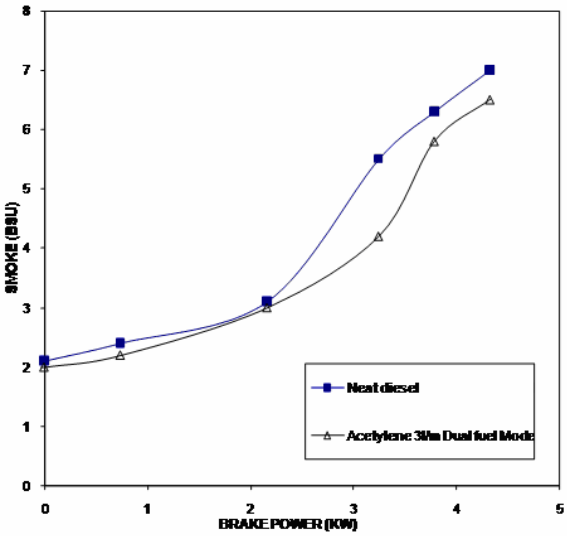

Figure 5. Variation of smoke with brake power.

5.3. Oxides of Nitrogen (NO_x)

It can be observed from figure 4 that NO*x* emission is 1866 ppm at maximum output with neat diesel fuel operation. In dual fuel operation with acetylene induction, NO*x* emission is increased by 17% when compared to baseline diesel operation. According to zeldovich mechanism model, the formation of NO*x* is attributed to the reaction temperature, reaction duration, and the availability of oxygen [1]. When acetylene is inducted, increase in NO*x* may be attributed to the increased peak cycle temperature level because of faster energy release, which is confirmed by increased peak cycle pressure.

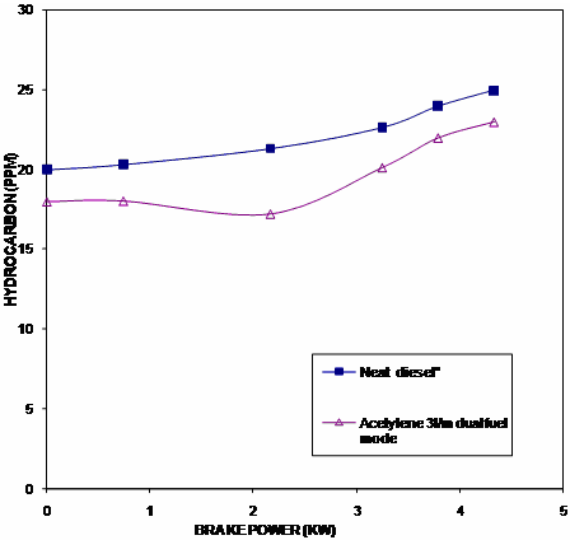

Figure 6. Variation of hydrocarbon with brake power.

5.4. Smoke

The variation of smoke level with brake power is shown in figure 5. The exact mechanism of smoke formation is still unknown. Generally speaking, smoke is formed by the pyrolysis of HC in the fuel rich zone, mainly under load conditions. In diesel engines operated

with heterogeneous mixtures, most of the smoke is formed in the diffusion flame. The amount of smoke present in the exhaust gas depends on the mode of mixture formation. The combustion processes and quantity of fuel injected occur before ignition [2]. The smoke level increases with increase in diesel flow rate, and at full load it is 7 BSU in case of diesel fuel operation. Dual-fuel operation with any gaseous fuel proved to be a potential way of reducing the smoke density as compared to diesel operation. A reduction in smoke level is noticed. The smoke level is reduced by 14% in induction technique at full load when compared to baseline diesel operation. This may be attributed to the fact that combustion of acetylene-diesel fuel is faster, contributing to complete combustion, and is also due to triple bond in acetylene which is unstable.

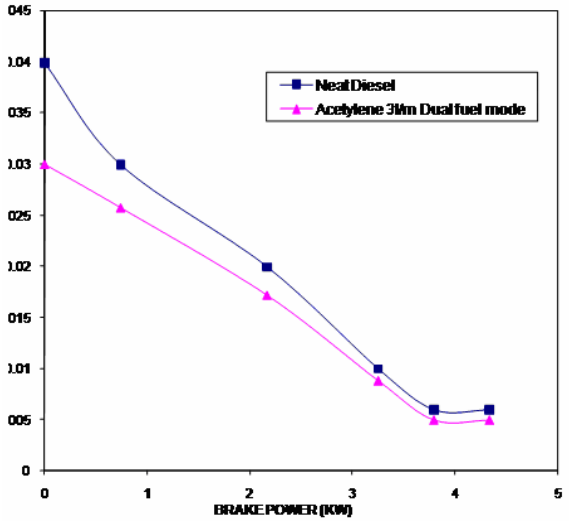

Figure 7.Variation of carbon monoxide with brake power.

5.5. Hydrocarbon Emissions

Figure 6 depicts the variation of hydrocarbon emissions with load. The HC emissions are 25 ppm in baseline diesel operation and 23 ppm when acetylene is aspirated at full load in induction technique. The reduction in HC emission in the case of dual fuel mode is due to the higher burning velocity of acetylene which enhances the burning rate.

5.6. Carbon Monoxide Emissions

The variation of carbon monoxide emissions with load exhibits similar trend of HC. This is shown in figure 7. The CO emissions are lower compared to the base line diesel operation. The maximum is 0.01% by volume in induction technique followed by base line diesel of 0.02% at full load. The CO emissions are lower due to the complete burning of the fuel, and is also due to the reduction in the overall C/H ratio of total fuel inducted into the engine.

5.7. Carbon Dioxide Emissions

The CO_2 emissions are lower compared to the base line diesel, the minimum being 8.7% by volume at full load in acetylene induction technique followed by 9.0% by volume in baseline diesel operation, as shown in figure 8. The CO_2 emission of acetylene is lowered because of lower hydrogen to carbon ratio.

5.8. Pressure Crank Angle Diagram

Figure 9 portrays the variation of cylinder pressure with crank angle. The peak pressure is about 72.1 bar at maximum power with base line diesel operation. Peak pressure is further increased in dual fuel operation with acetylene induction at maximum load. In dual fuel engine, the trend of increase in peak pressure is due to increased ignition delay and rapidity of combustion. There is an increase to about 3. bar when acetylene is inducted. The peak pressure for acetylene inducted dual fuel engine is advanced by 5°CA compared to peak pressure of diesel at full load. The advance in peak pressure for acetylene combustion is perhaps due to instantaneous combustion of acetylene as compared to diesel. The rate of pressure rise is also high for acetylene operated dual fuel engine, compared to diesel operated engine due to instantaneous combustion of acetylene fuel.

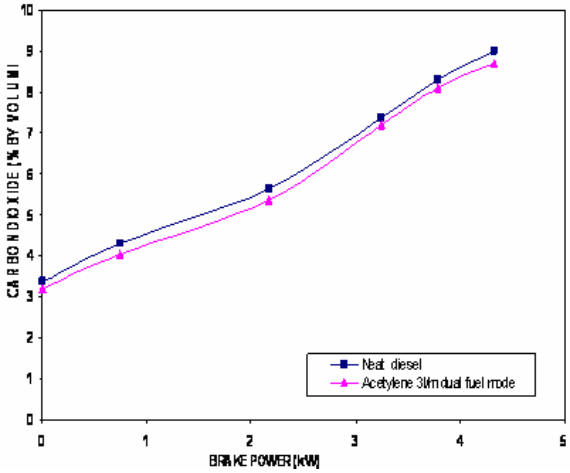

Figure 8. Variation of carbon dioxide with brake power.

5.9. Heat Release Rate

Figure 10 indicates the rate of heat release for acetylene operated dual fuel engine at 3 lpm flow rate, and diesel engine at full load as well. The burning rate diagram can be divided into three distinct phase, namely ignition delay, premixed combustion phase, mixing controlled combustion phase, and late combustion phase [1]. The heat release rate for acetylene aspiration shows distinct characteristics of explosive, premixed type combustion followed by a brief second phase dip in burning rate and then a rapid increase during the third phase of combustion of the gas mostly diffusion type of combustion.

6. Conclusions

Experiments were conducted to study the performance and emission characteristics of DI diesel engine in dual fuel mode of operation by aspirating acetylene gas in the inlet manifold for various loads, with diesel as an ignition source. The following conclusions have been arrived at, based on the experimental results:

- Brake thermal efficiency in dual fuel mode is lower than diesel operation at full load, as a result of continuous induction of acetylene in the intake.

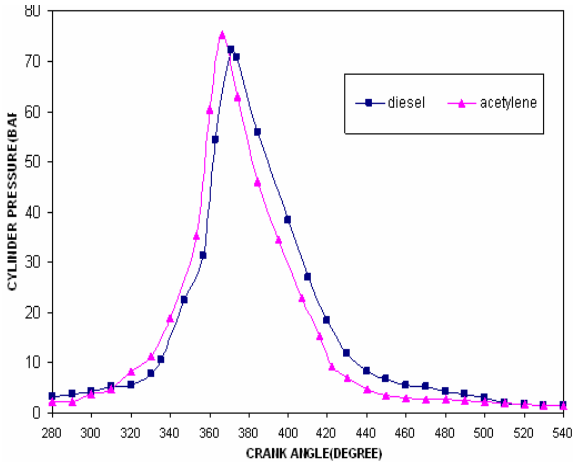

Figure 9.Variation of cylinder pressure with crank angle.

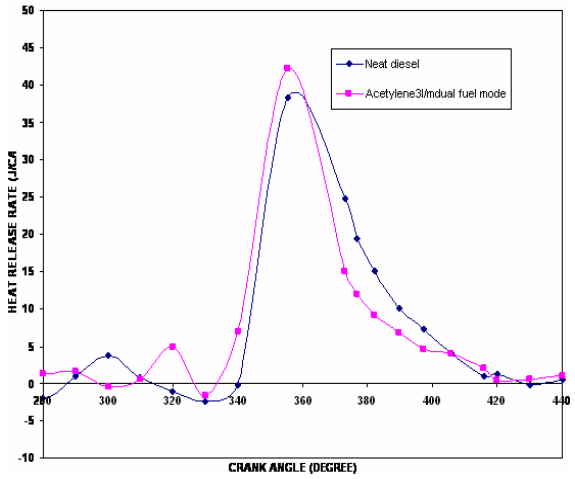

Figure 10. Variation of heat release rate with crank angle .

- Dual fuel operation of acetylene exhibits lower exhaust gas temperature of about 76°C as compared to diesel operation.
- There is an appreciable reduction in smoke level. It dropped from 7 to 6.50 BSU when compared to neat diesel operation.
- A perceivable reduction in HC, CO and CO2 emissions was observed with acetylene operated dual fuel mode. The reduction in HC and CO2 emissions at maximum load is of 8 % and 3% respectively when compared to diesel operation.
- There is an increase in the peak cylinder pressure and rate of pressure rise, when gas is inducted.

On the whole, it is concluded that acetylene induction resulted in a slight decrease in thermal efficiency, when compared to baseline diesel operation. Exhaust temperature, HC, CO, CO_2 and smoke emissions were less than baseline diesel operation. However, a significant increase in the NO_x emission is observed in the exhaust. To conclude, we state that acetylene would compete with hydrogen in near future for use of alternative fuel in internal combustion engine. By applying certain techniques like TMI, TPI of gas to get increased efficiency and reduced NOx emissions level.

References

[1] Heywood JB. Internal combustion engine fundamentals. Singapore: McGraw Hill Book Company; 1998.

[2] Ganesan V. Internal combustion engine. 3rd ed. Singapore: McGraw Hill Book Company; 2007.

[3] G.A. Karim, "The dual-fuel engine of the compression ignition type-prospects, problems and solutions-A review". SAE Paper No 831073, 1983.

[4] G.A. Karim, N.P.W. Moore, "The knock in dual-fuel engines". Proc Instn Mech Engrs, Vol. 181, 1966-67, 453-466.

[5] H. Rao, K.N. Shrivastava, N.H. Bhakta, "Hydrogen for dual-fuel engine operation". Int. J. Hydrogen Energy, Vol. 8, 1983, 381-384.

[6] C. Gunea, M.R.M. Razavi, G.A. Karim, "The effects of pilot fuel quantity on dual-fuel engine ignition delay". SAE Paper No 982453, 1998.

[7] L.M. Das, "Hydrogen engine research and development (R&D) programmes in Indian Institute of Technology (IIT)". Int. J. Hydrogen Energy, Vol. 27, 2002, 953-965.

[8] J. Wulff, W.Hulett, L. Sunggyu, "Internal combustion system using acetylene fuel". United States Patent No 6076487.

[9] V.M.S. Ashok, N.I. Khan, "Experimental investigation on use of welding gas (Acetylene) on SI Engine". Proceedings of AER Conference, IIT, 2006.

[10] N. Swami, J.M. Mallikarjuna, A. Ramesh, "HCCI engine operation with acetylene the fuel". SAE paper no 2008-28-0032.

[11] Holman JB. Experimental techniques for engineers. McGraw Hill Publications; 1992.

JJMIE

Volume 3, Number 2, June. 2009
ISSN 1995-6665
Pages 131- 140

Jordan Journal of Mechanical and Industrial Engineering

Investigation of the Mach Number Effects on Fluid-to-Fluid Interaction in an Unsteady Ejector with a Radial-Flow Diffuser

A.K. Ababneh[a,*], C.A. Garris[b], A.M. Jawarneh[a], H. Tlilan[a]

[a] *Department of Mechanical Engineering, Hashemite University, Zarqa, Jordan 11134*

[b] *Department of Mechanical Engineering, George Washington University, Washington DC, USA*

Abstract

The concept of fluid-to-fluid direct interaction whereby energy can be transferred among the interacting fluids was demonstrated and shown to be conceivable in non-steady ejectors. Unlike steady ejectors, the mechanism responsible for the energy transfer is reversible and thus higher efficiencies are expected. Of interest is to investigate the effects of Mach numbers on the performance of non-steady ejectors with radial-flow diffusers. The radial-flow ejectors usually lead to higher-pressure ratios with fewer stages. The Mach number of the primary fluid flow emerging out of the free-spinning rotor is considered an important factor among various parameters that affects the process of energy transfer. Specifically, the flow field is investigated at two Mach numbers 2.5 and 3.0 utilizing rectangular short-length supersonic nozzles for accelerating the primary fluid. Also the effects of increasing the total pressure of the primary fluid on the flow field are investigated. The results are compared with earlier investigation at Mach number 2.0, which showed significant enhancement in energy transfer with increase in Mach number. Fundamental to the enhancement of these devices performance relies on the management of the flow field in such a way to minimize entropy production. Numerical analysis utilizing a package of computational fluid dynamics was used for the investigation.

Keywords: Non-Steady Ejector; Fluid-to-Fluid Interaction; Pressure Exchange; Supersonic Flow; Radial-Flow Diffuser

Nomenclature [*]

B	Body force per unit mass, (N/kg)
c_v	Specific heat at constant volume, (J/kg-K)
c_p	Specific heat at constant pressure, (J/kg-K)
$\ddot{e}$	Deformation tensor, (1/s)
E	Total energy of system per unit mass and it includes internal and kinetic, (J/kg)
Es	The ratio of energy recieved by the secondary fluid relative to case M=2.0
F	Viscous surface forces of a fluid particle, (N/kg)
h	Static enthalpy, (J/kg)
h_o	Total enthalpy, (J/kg)
H	Height of rectangular supersonic nozzle at exit, (mm)
$\ddot{I}$	Identity strain tesor (1/s)
LHS	Left Hand Side
L_N	Length of the rectangular supersonic nozzle; from throat to exit plane, (mm)
L_{th}	Height of the supersonic nozzle at throat
mm	millimeter
p	Static pressure, (N/m^2)
$P_{o,ri}$	Total inlet pressure of the primary fluid, (N/m^2)
$P_{o,si}$	Total inlet pressure of the secondary fluid, (N/m^2)
$P_{o,so}$	Total outlet pressure of the secondary fluid, (N/m^2)
PEE	Pressure Exchange Ejector
q	Heat transfer flux, (W/m^2)
RHS	Right Hand Side
$\ddot{T}$	Stress tensor -with dots on top- which includes viscous and pressure, (N/m^2)
T_o	Total temperature, (K)
$T_{o,si}$	Total inlet temperature for the secondary fluid, (K)
$T_{o,so}$	Total outlet temperature for the secondary fluid, (K)
u	Fluid particle velocity in a non-inertial frame of reference, (m/s)
V	Fluid particle velocity, (m/s)
W	Depth of the rectangular supersonic nozzle and is constant throughout, (mm)
ϕ	Gravity potential, (N-m/kg)
μ	Dynamic viscosity of fluid, ($N\text{-}s/m^2$)
ρ	Density of fluid, (kg/m^3)
$\ddot{\tau}$	Viscous stress tensor, (N/m^2)
Ω	Angular velocity, (1/s)

1. Introduction

Therein lies a mechanism that regulates the energy flow between two directly interacting fluid-to-fluid which

[*] Corresponding author. *ababneh_hu@hu.edu.jo*.

potentially could be an optimal means for the energy transfer from high energetic fluid to a low energetic one. For this mechanism to come about the flow field must be unsteady. Non-steady ejectors have been utilized whereby this mechanism of energy transfer can take effect. The concept of non-steady ejector was introduced by Foa [1-3] and has since then been investigated by many researchers. The bulk of the work until the mid 1990s was focused on thrust augmentation where the theme was to induce larger mass flow rates for enhancing propulsion thrust; e.g., see [4-7]. Furthermore, this early research work was concerned with the primary fluid being accelerated to less than sonic speeds.

Fundamentally, this mechanism responsible for the energy transfer is related to pressure forces and it becomes apparent when the energy equation is expressed in the following differential form,

$$\frac{Dh_o}{Dt} = \frac{-1}{\rho}\nabla \cdot \bar{q} + \frac{1}{\rho}\bar{f} \cdot \bar{V} + \frac{1}{\rho}\frac{\partial p}{\partial t} \quad (1)$$

The left hand side of the equaiton represents the net rate of energy acquired by a fluid particle as it traverses an unsteady flow field, the first term on the right hand side is the energy transfer via heat transfer mode, the second is the energy transfer via the shear forces & turbulence mixing and the third is the energy transfer through the work of pressure forces. The later mode of energy transfer is often refered to as "pressure exchange" by researchers working in the field. The essence of the work of pressure forces that it is reversible in nature. In the classical ejectors, or as referred to steady ejectors, the unsteady term vanishes simply because the flow is steady hence for their operation they rely on the work of shear forces and turbulent mixing, highly non-reversible processes.

The non-steady ejectors, or sometimes are called pressure exchange ejectors, are considered to be an extension of the steady ejectors since they share several mechanical design features; i.e., primary fluid inlet ducting, secondary fluid inlet ducting, interaction region, a diffuser and more importantly they are known for their mechanical simplicity. However, a unique aspect of the non-steady ejectors is that they contain a frictionless free-spinning rotor whereby the flow is made non-steady with respect to an absolute frame of reference.

Beginning with the mid 1990s Garris [8-11] introduced the concept of utilizing supersonic nozzles to accelerate the primary fluid to supersonic speeds in the hope of achieving higher compression ratio of the secondary fluid for applications other than thrust augmentation as for example in the case of refrigeration and power augmentation. Soon experimental work for validation of concepts followed. Initial efforts, at the George Washington University, were made at building and testing a radial-flow non-steady ejector because of the potential application of this type. Basically, the radial-flow ejector consists of a free-spinning rotor embodied with as many supersonic rectangular nozzles as desired; The primary fluid is permitted to enter through the supersonic nozzles. The region where the two fluids are allowed to come in contact is confined between two plates where the flow is predominantly radial. Further description of the testing apparatus and concepts can be found in related work cited above.

Unforeseeably, the experimental work was halted because of mechanical difficulties; e.g., failures in thrust bearings, seals, development of instabilities and vibration in the set-up. Meaningful data could not be collected from the experimental work. Since then research activities have focused on numerical simulation to resolve the flow field regarding the radial-flow ejectors.

Numerical investigation was a step forward in keeping progress regarding the radial-flow non-steady ejector as well as other configuration [12-13]. The studies revealed in the case of subsonic flow fundamental features of the flow pattern whereby results showed vividly the two fluids remained discernable and separable throughout the ejector and at the same time energy was being transferred between the two interacting fluids. This is a distinct aspect to pressure exchange ejectors and a fundamental difference from steady ejectors whereby in the later mixing and turbulence are the mechanisms by which they energize the secondary fluid; i.e., in the steady ejectors the two interacting fluids emerge completely mixed. Therefore, higher performance levels for energizing secondary fluids when utilizing pressure exchange mechanism are perceivable. However, in the case of supersonic flows, the analyses revealed that the flow is predominantly unstable, hence the uniformity and quality of the flow was not observed to be as in the case of subsonic flow. Specifically, the flow field in the case of subsonic was observed to be steady in a reference frame attached to the rotating rotor while in the case of supersonic flow the two fluids tended to mix. The unsteadiness of the flow observed from the numerical results is likely the cause for the vibration encountered during the actual experimental work. The investigations were limited to subsonic flow and one case of supersonic flow at Mach number 2.0 with nozzles positioned at two spin angles 10^o and 20^o [14].

Undoubtedly, attaining higher levels of performance will necessitate going higher with Mach numbers as well as resolving the flow field instabilities. Therefore, in this paper the effects on the flow field of higher Mach numbers; i.e., 2.5 and 3.0, and that due to higher total pressure are investigated. Higher Mach numbers are achieved utilizing short-length rectangular supersonic nozzles with their profiles were generated using the method of characteristics. The base-line level for the boundary conditions; i.e., the total pressures, is that where the primary and secondary fluids are met at the matched condition which corresponds to the onset of the interaction between the two fluids, this in turn is governed by the secondary inlet total pressure. The total pressure of the primary fluid is then increased beyond that level to examine its effects on the flow field and performance. The matched condition is where the static pressures of the two fluids are the same, which results in perfect expansion of the primary fluid and also starts the interaction with no shocks.

Although the underlying objective is to gain further understanding of the various aspects of the energy transfer mechanism between the interacting fluids, in addition there are technical advantages of studying non-steady ejectors. For example, as has been repeatedly elucidated by various researchers working in the field that these devices are well

suited for steam refrigeration and hence environmental negative effects due to the use of the prevailing refrigerant nowadays can be significantly reduced if steam refrigeration becomes competitive alternative. Second, steam can be generated utilizing waste heat, which is abundant in automotive that utilizes internal combustion engines, therefore less of fossil fuel may be burned which otherwise needed to drive typical air-conditioning compressors.

2. Geometry and Model Construction

The ejector basically consists of three main parts as depicted in Figure 1: one, is the free spinning rotor; two, is the inlet ducting for the secondary fluid; and three, is the radial-flow diffuser. The free spinning rotor is the inner portion of the ejector, which includes the rectangular supersonic nozzles and spins on an axis aligned with the z-axis. It is exploded in Figure 1-d where in addition to the spin rotor half of the inlet ducting of the secondary fluid is shown. The inlet ducting of the secondary fluid is that portion where only the secondary fluid is present and it is seen to resemble an inner racing of a bearing in Figure 1-b; also half of it is seen in Figure 1-d. The radial-flow diffuser is the region where the two fluids come in physical contact and exchange energy. A segment of the diffuser is depicted in Figure 1-c. The length of the diffuser L_d (91.2 mm) is maintained constant for the two cases (M=2.5 and M=3.0) and is chosen of the same length as that in the case of M=2.0. The overall model geometry is based on the actual model that was attempted for the experimental study [10], however, the radial diffuser was modified to lessen the severity on the supersonic flow as was recommended [14] so that unnecessary shocks generation are avoided. The rectangular supersonic nozzles (total of 8) are positioned at a spin angle of 10^o from the meridian plane. The spin angle is the parameter that permits the rotor to spin.

As mentioned for accelerating the primary fluid two sizes of short-length rectangular supersonic nozzles are used in this study. The profiles for these nozzles were generated utilizing the method of characteristics [15,16]. The nozzles share the same cross-sectional area at the throat as that of M=2.0 [14]. The pertinent dimensions of the nozzles are given in Table 1. The nozzles were verified separately under stationary conditions for the purpose of ensuring the generation of the desired Mach numbers; e.g., 2.5, and 3.0, using ideal air isentropic analyses. These simulations showed satisfactory results as evident in Figure 2, which depicts the Mach number and total pressure variations along the distance in the stream wise direction. Also included in Figure 2 the results pertaining to the case M=2.0.

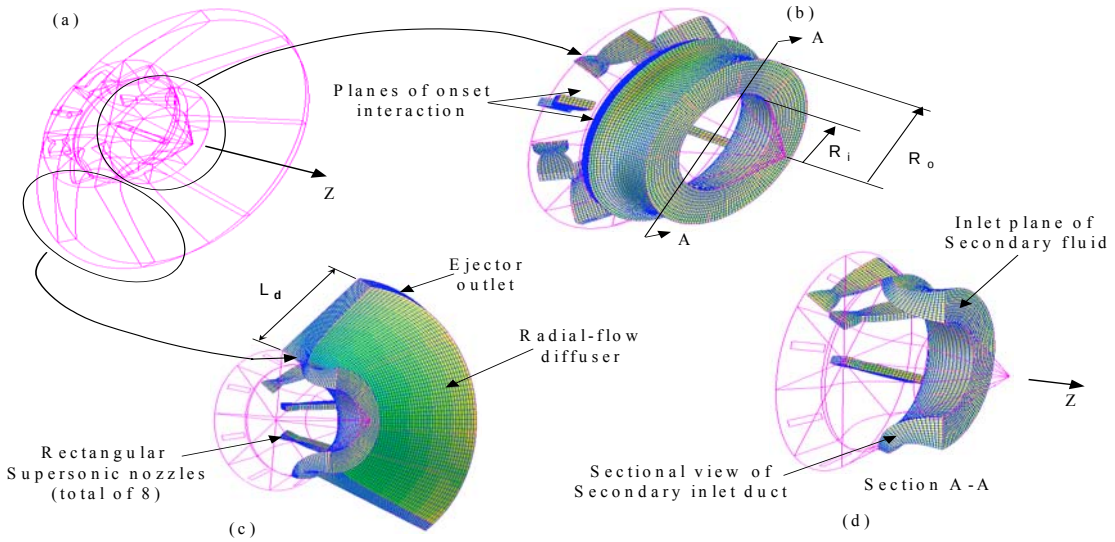

Figure 1. Non-steady flow ejector: (a) wire frame of the ejector; (b) inlet ducting of the secondary fluid and also is shown the rectangular supersonic nozzles; (c) radial-flow diffuser; and (d) wire frame of the rotor and a sectional view of the inlet ducting for the secondary fluid.

Table 1. Dimensions of the rectangular supersonic nozzles; each nozzle is specified by its design Mack No.

Mach No.	L_{th} (mm)	L_N (mm)	H (mm)	W (mm)
2.0	5.2	12.5	8.7	4.8
2.5	5.2	25.1	14.8	4.8
3.0	5.2	49.0	25.2	4.8

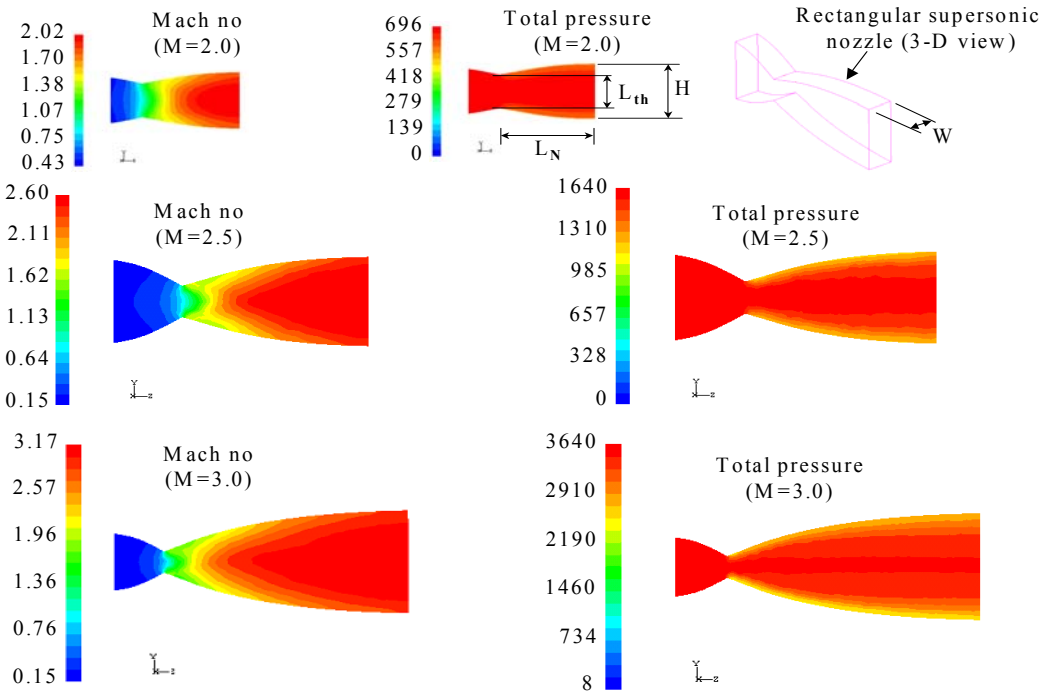

Figure 2. Mach number and total pressure variation in the stream wise direction in the three rectangular supersonic nozzles; Mach No =2.0, 2.5, 3.0.(Total pressure is in gage kPa).

3. Governing Equations and Solution Validations

3.1. Governing Equations

Because the aim of this paper is to investigate the effects of the Mach number and the total pressure of the primary fluid on the effectiveness of the pressure exchange mechanism; i.e., the third term in the right hand side of equation (1), the flow field is taken to be laminar, thus ignoring turbulant mixing. The governing principles are the basic equations of fluid motion; i.e., the continuity, momentum and energy equations [15,17]. The differential form of the continuity equation is

$$\frac{\partial \rho}{\partial t} + \nabla \cdot \rho \vec{V} = 0 \tag{2}$$

The momentum principle is that the rate of change of linear momentum for an enclosed region fixed in space is equal to the sum of forces acting on the region, which is expressed in a differential form as

$$\rho \frac{D\vec{V}}{Dt} = -\nabla p + \rho \vec{B} + \nabla \cdot \ddot{\tau} \tag{3}$$

Assuming the fluids being of Newtonian type along with the Stokes hypothesis the viscous stress tensor is expressed as

$$\ddot{\tau} = -\tfrac{2}{3}\mu \ddot{I} + 2\mu \ddot{e} \tag{4}$$

Where $\ddot{e}$ is the deformation tensor and μ is the fluid dynamic viscosity.

For the energy equation it is expressed as

$$\rho \frac{DE}{Dt} = \nabla \cdot \ddot{T} \cdot \vec{V} + \nabla \cdot \vec{q} \tag{5}$$

Where E is the sum of the internal and kinetic energies and $\ddot{T}$ is the stress tensor; with double dots on top. Potential energies is normally neglected in the case of gases. The working fluid is ideal air for both primary and secondary, hence the internal energy and enthalpy are expressed as

$$u = c_v T \quad and \quad h = c_p T \tag{6}$$

where T is the temperature. The equation of state for the ideal air is used to complete the system of equations.

3.2. Solution and Boundary Conditions

In the absolute frame of reference the interaction of the primary fluid with the secondary is time depedent. The problem, however, is treated with respect to a frame of reference attached to the rotor. In this non-inertial coordinate frame of reference the continuity and energy equations are unaffectedby by the coordinate transformation whereas the momentum equation is re-casted to account for the coordinate transformation, since Newton's Law of motion equates applied forces to acceleration in an inertial frame of reference.

As a result of the coordinate transformation there are two terms that appear; namely, the centriputal and Coriolis accelerations. The centriputal forces can be considered as an additional body force and hence they are added to the gravity potential.

The viscous dissipation term is unaffected by the coordinate transformation and hence the momentum equation becomes

$$\rho\left[\frac{D\vec{u}}{Dt}+2\vec{\Omega}\times\vec{u}\right]=-\nabla p+\rho\vec{F}+\rho\nabla\phi \qquad (7)$$

The second term in the LHS is the Coriolis forces, **F** represnets the viscous surface forces, ϕ is the gravity potential and Ω is the angular velocity. The velocity **u** is the relative velocity in the rotating frame of reference [18].

The angular speed of the rotor is based on the ideal free spinning speed of the rotor. Under the assumption of no applied external torque and in the absence of friction effects the fluid emerges from the nozzles with an exit velocity along the meridian plane for each nozzle. However, this speed is numerically fine tuned based on the energy conservation. The variation from the ideal speed is mainly due to the effects of nozzles three-dimensionality [8].

The boundary conditions include specifying the total pressure at the inelt ductings for the primary and secondary fluids. Because the primary is the energetic fluid its mass flow rate and velocity are known at the inelt while the masss flow rate of the secondary fluid is determined from the solution which results from the induction action. At the outlet of the ejector the static pressure is specified. Because the ejector performance is not known ahead of time and the two fluids have non-uniform conditions in the interaction region, the specification of the outlet static pressure was tangibly involved. An iterative approach was adopted where an efficiency of the ejector was first assumed and then the static pressure based on perfect mixture of the two fluids was computed. The solid walls provided the remaining boundary condition for the flow confinement. The current investigation considers mainly inviscid fluid and hence the walls provide the slip condition. In some cases, viscous effects were included to account for their action on the secondanry fluid, but the walls effects is turned off by considering slip condition. Thus, the normal component to the wall of the relative velocity with no seepage vanishes. Mathematically,

$$\left(\vec{u}-\vec{V}_b\right)\cdot\vec{n}_n=0 \qquad (8)$$

where **n** is the normal vector of the walls and $\mathbf{V}_b$ is the boundary velocity relative to the inertial frame of reference.

The optimal operating point for non-steady ejectors where entropy production is anticipated to be minimized has been recognized to be at the matched point [8,9] whereby the static pressures of the two interacting fluids at the onset of interaction are the same. The matched point specifies the baseline conditions; i.e., for the primary total pressure.

The numerical method is based on the Method of Finite Volume Finite Difference whereby the domain is subdivided into grid points with each point is surrounded by its control volume in a manner that is non-overlapping with the neighboring grid points' control volumes. Piecewise functions can be used as the simplest forms for expressing the variations of the dependent variables between the grid points. The discritization in this manner expresses the conservation of the dependent variables over the grids' control volumes just as the differential forms of the governing equations for the infinitesimal control volume. The implication is that mass, momentum, and energy equations are exactly satisfied; and not just in the limiting sense when the number of grid points becomes large [19].

The solutions were obtained utilizing the Computational Fluid Dynamics (CFD) package FLUENT-v6.2.16, which is a sophisticated analytical and a state of the art package and has been developed over the years. The package in addition to predicting fluid flows behavior it handles problems that involve heat transfer, mass transfer and as well as chemical reaction. The package also has found application in industry such as in Aerospace/Defense, Appliances, Automotive, Biomedical, etc.

3.3. Validation of The Solution

Because of the lack of experimental data to compare with the validation of the numerical solutions concerning the flow filed for pressure exchange ejectors with radial-flow diffuser, the validation is made in two ways. One is to demonstrate that the numerical technique is capable of resolving the flow field of a similar problem that involves the same mechanism of energy transfer but has an analytical solution. Second, is to verify that the numerical solution is convergent and consistent.

The shock tube, which has an analytical solution, has been utilized as a test case for the verification of the numerical procedure concerning the problem described herein. The unsteady events of the flow field in a shock tube begin at the onset of membrane breakup whereby energy flows from the energetic fluid to the low-energetic one and is shown to be governed by equation (1) [15-16]. The analytical solution however, is simplified by considering ideal fluids and neglecting the effects of thermal transfer thus the only term left on the right hand side of equation (1) is the unsteady pressure term, which is the mechanism that is being investigated herein. Figure 3 shows the pressure and velocity behind the traveling shock, moving to the right, in the tube after the membrane is broken up which was placed at position –12.5 mm. The initial temperature and pressure for the primary and secondary fluids were set at 500 K & 500 kPa, gage, and 330 K & 0 kPa, gage, respectively. Both fluids were chosen as ideal compressible air. From the analytical solution the pressure and velocity behind the traveling shock are 153.0kPa, gage and 259.3 m/s, which compares very well with the solution. The CFD method also did capture details of the phenomenon involved by revealing the expansion nature behind it (i.e., to the left where it s being gradual) and compression aspect ahead of it.

The convergence of the numerical solution has been demonstrated throughout this work and is evident from the results, which are presented in section 4. The consistency of the solutions was demonstrated by considering smaller mesh sizes and showing that the solutions are non-significantly different. Also to be noted the numerical procedure has shown satisfactory results when verifying

the flow in the supersonic nozzles (Figure 2), however, the procedure in this case was of a steady nature.

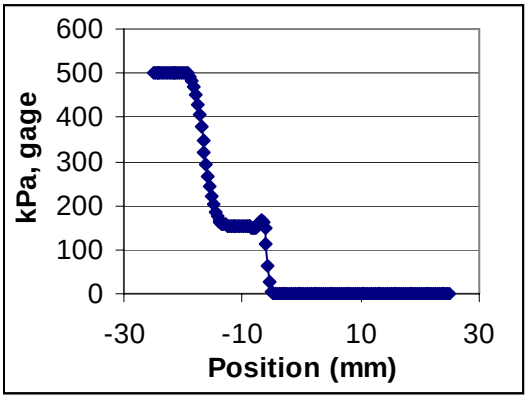

(a)

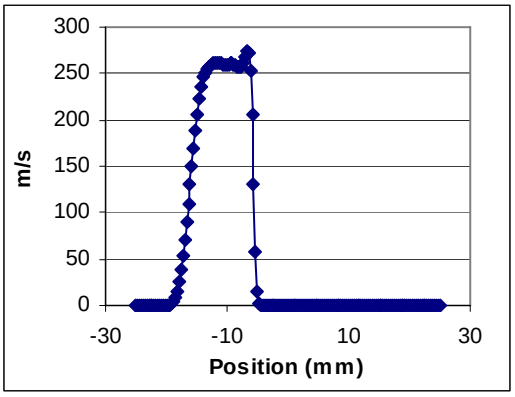

(b)

Figure 3. (a),(b). Pressure and velocity distribution along the shock tube .

The convergence of the numerical solution has been demonstrated throughout this work and is evident from the results, which are presented in section 4. The consistency of the solutions was demonstrated by considering smaller mesh sizes and showing that the solutions are non-significantly different. Also to be noted the numerical procedure has shown satisfactory results when verifying the flow in the supersonic nozzles (Figure 2), however, the procedure in this case was of a steady nature.

4. Results and Discussions

As dictated by equastion (1) the total enthalpy of a fluid particle traversing a non-steady flow field will change accordingly. This fact is demonstrated in Figure. 4 which shows the total temperature distribution in an r-z and r-θ planes of the ejector (Figure. 1). Recall that for an ideal gas the total enthalpies and temperatures differ by a constant. Prior to the onset of the interaction the total temperature of the secondary fluid remains constant T_o = 300 K since it entirely occupies the ejector's secondary nozzle. The secondary nozzle is a convergant ducting that is located in the opposite side that contains the primary supersonic nozzles. Down stream of the onset plane of interaction the total temperature for the secondary fluid is seen to increase continuously at the expense of the primary fluid. The two fluids can be distinguished from each other by examining the r-θ planes (identified at the locations z = 0.035, 0.045, 0.050) whereby the primary fluid is seen to have the higher T_o as compared to the secondary fluid. Further the primary fluid is observed to be localized in small elliptical areas since it leaves the rectangular supersonic nozzles at smaller areas while the secondary fluid fills the areas in between the primary jets; there are a total of eight primary jets corresponding to the number of the supersonic nozzles.

The unstability nature of the flow is evident in Figure 4 where the uniformity and quality of the flow is not well preserved as seen in the case of subsonic flow [14]; observe how the primary fluid is smearing as it progresses in the ejector; e.g., moving in the rθ planes identified with z = 0.035, z = 0.045 and z = 0.05. However, it is clear that the two fluids are still separable a feature is highly desirable in these technologies sepecially in the case of having dissimilar fluids. The primary jets were observed to oscillate causing the flow to be unbstable. The oscillation is likely caused by a system of waves reflections and interactions in the diffuser which eventually leads to distorting the flow field pattern. The non-stability of the flow and the oscillation of the primary jets are, most probably, the cause for the actual vibration developed during the actual experimental attempts. Therefore, a step forward in these technologies will invlove the flow management for yielding well behaved flow.

Consequent to the energy gained by the secondary fluid is that it is enabled to flow through the ejector by entering at the secondary inlet ducting, where its total pressure is set at 0 Pa gage, and overcoming a static pressure boundary 2kPa gage set at the outlet of the ejector. What is important however is that the secondary fluid is induced into the ejector at high speeds as evident in Figure 5 where it is seen that the velocity is approximately reaching 300 m/s at the secondary throat. Eventually, the total pressure at the outlet of the ejector is the measure of the useful work transferred to the secondary fluid. In addition, the mass rate of induction of the secondary fluid is required to compute the rate of energy transferred. Figure 6 shows the induction mass flow rate of the secondary fluid, which is caused, by the action of the primary fluid on the secondary. The Figure also reveals the non-stability nature of the flow field; nonetheless, the overall flow is remaining stable by yielding a time-average value of nearly 0.35 kg/sec for the case of Mach no 2.5.

The underlying mechanism is fundamentally different in a pressure exchange ejector than in a steady ejector. In the later the driving force for energizing the secondary flow is due to turbulence mixing and shear stresses hence the flow quickly tends to uniformity in all aspects and consequently the two fluids, primary and secondary, become essentially indiscernibile.

To the contrary in pressure exchange ejector when the flow is well maintained and managed by carefull design, only energy is allowed to flow from the primary to the secondary via the pressure forces that act at the inerfacial surfaces between the two fluids and eventually the two fluids emerge out of the ejector intact and seperable. These facts are still confirmed as depicted in Figure 4 even thoguh the flow was not maintained as orderly as in the caseyofhsubsonicgflow[14].

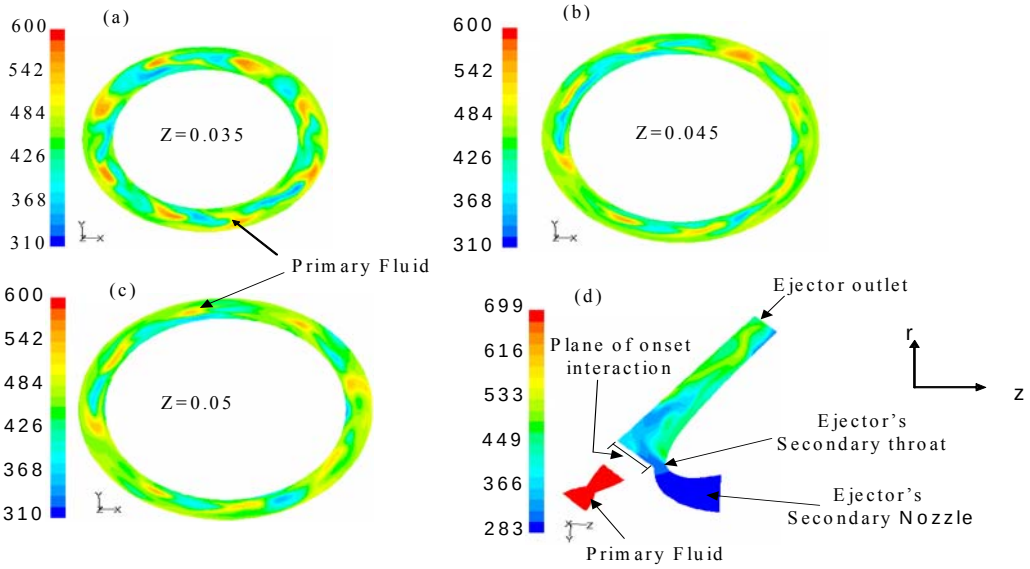

Figure 4. Total temperature variation M=2.5 in different planes of the ejector: a, b, and c are r-θ planes at z=0.035, 0.045, and 0.050, while d is an r-z plane.

The unstability nature of the flow is evident in Figure 4 where the uniformity and quality of the flow is not well preserved as seen in the case of subsonic flow [14]; observe how the primary fluid is smearing as it progresses in the ejector; e.g., moving in the rθ planes identified with z=0.035, z=0.045 and z=0.05. However, it is clear that the two fluids are still separable a feature is highly desirable in these technologies sepecially in the case of having dissimilar fluids. The primary jets were observed to oscillate causing the flow to be unbstable. The oscillation is likely caused by a system of waves reflections and interactions in the diffuser which eventually leads to distorting the flow field pattern. The non-stability of the flow and the oscillation of the primary jets are, most probably, the cause for the actual vibration developed during the actual experimental attempts. Therefore, a step forward in these technologies will invlove the flow management for yielding well behaved flow.

Consequent to the energy gained by the secondary fluid is that it is enabled to flow through the ejector by entering at the secondary inlet ducting, where its total pressure is set at 0 Pa gage, and overcoming a static pressure boundary 2kPa gage set at the outlet of the ejector.

What is important however is that the secondary fluid is induced into the ejector at high speeds as evident in Figure 5 where it is seen that the velocity is approximately reaching 300 m/s at the secondary throat. Eventually, the total pressure at the outlet of the ejector is the measure of the useful work transferred to the secondary fluid. In addition, the mass rate of induction of the secondary fluid is required to compute the rate of energy transferred. Figure 6 shows the induction mass flow rate of the secondary fluid, which is caused, by the action of the primary fluid on the secondary. The Figure also reveals the non-stability nature of the flow field; nonetheless, the overall flow is remaining stable by yielding a time-average value of nearly 0.35 kg/sec for the case of Mach no 2.5.

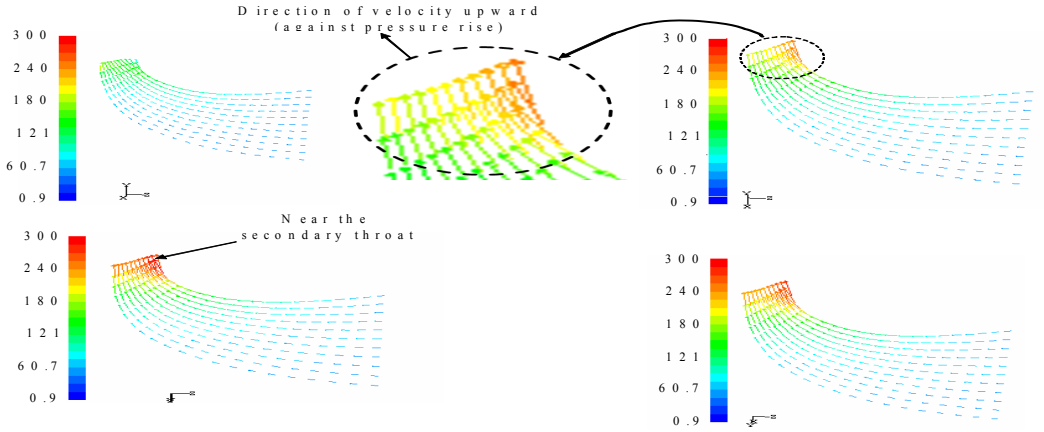

Figure 5. Secondary fluid velocity in the ejector's secondary inlet in different r-z planes.

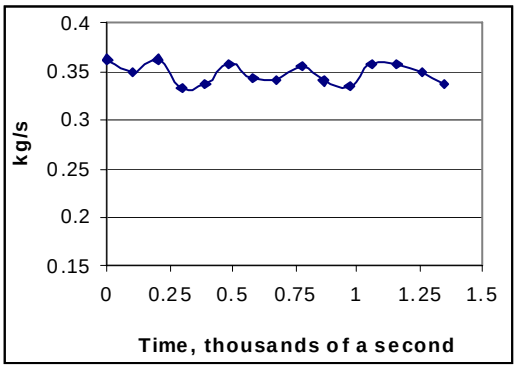

Figure 6. Mass flow rate of the secondary fluid induction. Mach no = 2.5.

The underlying mechanism is fundamentally different in a pressure exchange ejector than in a steady ejector. In the later the driving force for energizing the secondary flow is due to turbulence mixing and shear stresses hence the flow quickly tends to uniformity in all aspects and consequently the two fluids, primary and secondary, become essentially indiscernibile. To the contrary in pressure exchange ejector when the flow is well maintained and managed by carefull design, only energy is allowed to flow from the primary to the secondary via the pressure forces that act at the inerfacial surfaces between the two fluids and eventually the two fluids emerge out of the ejector intact and seperable. These facts are still confirmed as depicted in Figure 4 even thoguh the flow was not maintained as orderly as in the case of subsonic flow [14].

Examining Figure 4 closely it is evident that the total enthalpy of the primary is decreasing as the fluid proceeds in the ejector; e.g., compare Figure 4a and c. That is the level of total enthalpy of the primary fluid, which is seen as the red spots, is decreasing in value when moving from rθ planes z=0.035 (Figure 4a) to z=0.045 (Figure 4b) and to z=0.05 (Figure 4c). On the otherhand, the secondary fluid which fills the space between the primary fluid is seen to increase in total enthalpy when moving outward in the planes along the z-axis. In the limit as the diffuser gets larger, it is expected that the total pressures of the two fluids will become identical and hence energy transfer will come to an end; at least in terms of useful work. The total pressure is used to measure the ejector performance since the total temperature includes the effects of irreversibilities such as the rise in static temperature due to the presence of shocks and shear stresses. Therefore, to evaluate the performance of the ejector the mass averaged of the total pressures at the outlet was obtained, see Figure 7 which reveals the variation in the outlet total pressure. Mean averages over a reasonable length of time were used for computing the total pressure to account for flow non-stabilities. The peculiar difference in the two curves at the begining of the simulation time is due to a difference in the initial starting conditions. Table 2 summarizes the results in the form of pressure ratio ($P_{o,so}/P_{o,si}$) gained by the secondary fluid versus that of the primary fluid $P_{o,ri}/P_{o,si}$.

The cases presented in Table 2, except for case 3, are for the matched conditions; i.e., the static pressures of the two fluids are equal at the onset of the interaction. The amount of energy Es, last column, received by the secondary fluid is seen to increase with Mach number. The Es is the ratio of energy recieved by the secondary fluid relative to case 1 and it is related to the product of the compression ratio and the mass flow rate. Note also that for choked conditions the mass rate is proportional to the total pressure and inversely to the square root of the total temperature. Because increasing Mach number while maintaining matched conditions implies that the total pressure of the fluid must increase, case number 3 was generated to isolate the effects of Mach number on the performance. Specifically, the inlet total pressure equal to that of case number 4, total pressure for Mach no 3.0, was used with the case of Mach no 2.5. The increase in performance seen in case 4 over that of case 3 is mainly due to the Mach number effects, which clearly reveals its superiority in terms of energy transfer over case 3. One reason for this behavior is that at the matched conditions there are no developed shocks at the onset of interaction and hence less of entropy production is generated in the flow which eventually leads to higher performance.

Table 2. Summary of Mach number effects on ejector performance.

Case no.	Mach No	$P_{o,ri}/P_{so,i}$	$P_{o,so}/P_{o,si}$	m_s/m_p	Es
1	2.0	4.13	1.11	1.71	1.0
2	2.5	9.03	1.10	1.28	1.5
3*	2.5	19.4	1.36	0.68	5.7
4	3.0	19.4	1.35	0.81	6.6

* Total pressure is at higher level than that at the matched conditions.

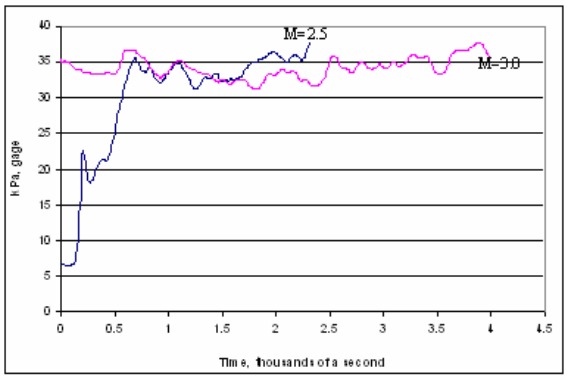

Figure 7. Effects of Mach number on ejector performance; total pressure ratio 19.4 for both cases (M=2.5 and M=3.0).

The increase in the level of compression ratio of the secondary fluid with the total pressure has lead to evaluating the ejector at primary pressure levels higher than the ideally matched conditions Figure 8. The matched conditions are expected to yield best performance since entropy production due to shocks are expected to be least; in the case of ideal fluids entropy production should be zero if no shocks are developed in the diffuser. Nevertheless, in real applications where higher compression ratio for the secondary fluid are desired it may be necessary to run ejector beyond the matched conditions simply because higher Mach number requires longer supersonic nozzles (see Table 1.0) as well as higher velocities which might be more involved in terms of

entropy production due to stronger shocks in the diffuser. The results from the these simulations with pressures higher than the match condition are summarized in Table 3 for the case with M = 3.0. Similar trend is expected with the other cases. In these simulations, it was also observed that the quality of the flow improved with the increase in the primary total pressure by showing less flow reversals and non-stability.

The implication of this is that the diffuser may have been starved of fluid at lower pressures. It is to be noted that the primary mass flow rate m_p increases with total pressure thus leading to the mass ratio of the secondary m_s to the primary to decrease.

Table 3. Effects of primary pressure on the ejector performance. Mach no = 3.0.

$P_{o,ri}/P_{o,si}$	$P_{o,so}/P_{o,si}$	m_s/m_p
19.4	1.35	0.81
20.1	1.41	0.75
30.0	1.78	0.53
40.0	2.38	0.39
50.0	3.02	0.31

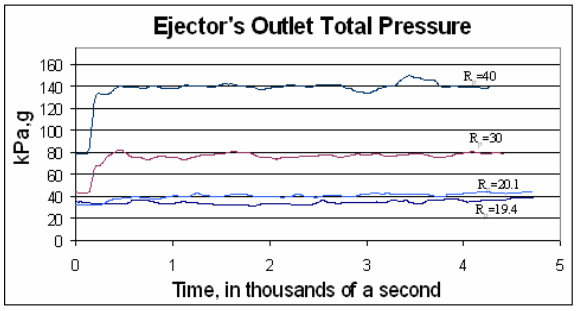

Figure 8. Variation of outlet total pressure at Mach no = 3.0; curves identified with the ratio in total pressure of primary to secondary ($R_p=P_{o,ri}/P_{o,si}$).

5. Conclusions

The flow field of a non-steady ejector with a radial-flow diffuser was investigated at Mach numbers; i.e., M=2.5 and 3.0, as well as with total pressure of the primary fluid that are higher than those at the matched conditions. Results have confirmed anticipated trend whereby optimal performance of non-steady ejectors are achieved when they are operated at matched conditions as was demonstrated in Table 2 with cases 3 and 4. It was observed that the increase of the Mach number resulted in an increase in the amount of energy transfer to the secondary fluid. However, with the increase in Mach number longer supersonic nozzles are required as well as the flow field in the diffuser will be more susceptible for stronger shocks due to the higher velocities. Thus, from practical engineering point it may be necessary to run these devices at total pressures higher than their optimal design point; i.e., higher than that of the matched conditions, but with lesser Mach numbers. As evident from Table 3, higher compression ratio of the secondary fluid can be readily obtained with the increase in the primary total pressure.

The flow behavior was also observed to be of less severe in terms of non-stabilities and flow reversals with higher total pressures, however still showing non-stabilities. This quality of the flow is a critical area that must be resolved to improve the performance of these devices. The improvement in the flow pattern with the increase in total pressure is likely related to the diffuser of being less starved of fluid. Nonetheless, additional studies must be carried out to systematically produce higher flow qualities.

The results also showed clearly the two fluids are still discernable and separable throughout the flow field and most importantly near the ejector's outlet; i.e., after energy is transferred to the secondary fluid.

This is a distinguishing feature of non-steady ejectors especially if the fluids are dissimilar.

References

[1] Foa JV. New method of energy exchange between flows and some of its applications. Technical Report No. TR-AE-5509: Rennselaer Polytechnic Institute; December 1955.

[2] Foa JV. Elements of flight propulsion. John Wiley & Son; 1960.

[3] Foa JV, Garris CA. Cryptosteady modes of direct fluid-fluid energy exchange. Chapter in ASME Book AD-7; 1984.

[4] S.M. Amin, C.A. Garris, "An experimental investigation of a non-steady flow thrust augment". AIAA/ASME/SAE/ASEE Joint Propulsion Conference, Paper No.AIAA-95-2802, July 1995.

[5] Avellone G. Theorectical and experimental investigation of the direct exchange of mechanical energy between two fluids. Grumman Research Dept. Memorandum RM 365; June 1967.

[6] Costopoulos T. A wide-jet strip analysis of crypto steady-flow thrust augmenters Parts 1 and 2. Technical Report No. TR-UTA-772: George Washington University; March 1977.

[7] K.H. Hohenemser, J.L. Porter, "Contribution to the theory of rotary-jet flow induction". J. Aircraft, Vol. 3, No. 4, July 1966, 339-346.

[8] C.A. Garris, W.J. Hong, "Radial-flow pressure exchange ejector". ASME Proceeding of the Third International Symposium on Pumping Machinery, Vancouver, Canada, June 1997.

[9] Garris CA. Pressure exchange ejector and refrigeration apparatus and method. US Patent No. 5,647,221; July 1997.

[10] C.A. Garris, W.J. Hong, C.M. Mavriplis, J. Shipman, "A new thermally driven refrigeration system with environmental benefits". Intersociety Engineering Conference on Energy Conversion, Colorado Springs, Co, August 2-6,1998.

[11] Garris CA. Pressure exchange compressor-expander and method of use. US Patent No. 6,434,943 B1; August 2002.

[12] W.J. Hong, K. Al-Hussan, H. Zhang, C.A. Garris, "A novel thermally driven rotor-vane/pressure-exchange ejector refrigeration system with environmental benefits and energy efficiency". International Conference on Efficiency, Costs, Optimization, Simulations and Environmental Impact of Energy Systems, Berlin, Germany, July 3-5, 2002.

[13] K. Al-Hussan, C.A. Garris, "Non-steady three dimensional flow field analysis in supersonic flow induction". ASME International Fluids Engineering Summer Conference, Montreal, Canada, July 14-18, 2002.

[14] Ababneh AK. Investigation of fluid to fluid interaction in a radial-flow pressure exchange ejector. PhD Dissertation, George Washington University; 2003.

[15] Anderson JD. Modern compressible flow with historical perspective. McGraw-Hill Inc.; 1990.

[16] Saad MA. Compressible fluid flow. Prentice Hall, Inc.; 1993.

[17] Aris R. Vector tensor and the basic equations of fluid mechanics. Prentice Hall; 1962.

[18] Pedlosky J. Geophysical fluid dynamics. 2nd ed, Springer-Verlag; 1987.

[19] Pantankar SV. Numerical heat transfer and fluid flow. Hemisphere Publishing Corporation; 1980.

JJMIE

Volume 3, Number 2, June. 2009
ISSN 1995-6665
Pages141 - 150

Jordan Journal of Mechanical and Industrial Engineering

Spatial Distribution and Environmental Implications of Lead and Zinc in Urban Soils and Street Dusts Samples in Al-Hashimeyeh Municipality

Kholoud Mashal [a,*], Mohammed Al-Qinna [a], Yahya Ali [b]

[a] Department of Land Management and Environment, Hashemite university , Zarqa, Jordan

[b] Department of Humanities and Social Sciences, Hashemite university , Zarqa, Jordan

Abstract

The state of heavy metal pollution and mobility of both Pb and Zn were investigated in selected urban soils and street dusts samples in Al-Hashimeyeh Municipality. A total of 43 selected sites were sampled, using composite sampling technique derived from four sub-samples. Sequential extractions were implied to predict the percentages of Pb and Zn present in each soil geochemical phases. Results indicated that street dust samples in Al-Hashemiya have elevated concentrations of Pb (115.3 mg/kg) and Zn (228 mg/kg). Very little amounts of Pb and Zn were retrieved from the exchangeable phase, the readily available for biogeochemistry cycles in the ecosystems. The hydroxide-bound fraction of Pb dominated in almost all soils and dust with highest percentages (69%, 77%, respectively) indicating that this metal is strongly bounded to the solid. Zinic mostly occurred in hydroxide bound fraction in street dust (65%) while the highest percentages of Zn, in urban soils, were found in the hydroxide bound fraction and mineral structure (residual fraction) with 44% and 51.2%, respectively. Furthermore, the concentrations of Pb in urban and street dust samples pose a low risk to the environment with 8% and 9% respectively, existing in exchangeable and carbonate fractions. While the results show that Zn in street dust poses a medium risk with 15% exists in exchangeable and carbonate fractions. The chemical results were intensively investigated using spatial and statistical modeling techniques to predict heavy metal loads and distribution in space. The analyses suggest the presence of heavily contaminant zones allocated at, or close to, industrial activities at the area, suggesting that the major contamination sources might be attributed to both traffic emissions and industrial activities. The paper also provides prediction models for both heavy metals spatial behavior using stepwise regressions and varigogram techniques.

Keywords: Heavy Metals; Spatial Variability; Sequential Extraction; Lead; Zinc

1. Introduction

Generally, urban systems are highly sophisticated and complex. In these systems, top soils and roadside dusts are indicators of several environmental pollutants [1-2]. Levels of contaminants associated with street dusts have received a great interest in the previous decades, because elemental composition and concentrations in these dusts reflect the characteristics of the activities going on in a particular area. These systems have the potential to provide considerable loadings of several contaminants to the receiving water and water bodies, particularly with changing environmental conditions [3].

Heavy metals (particularly Pb, and Zn) are good indicators of contamination in urban soils and street dust. They appear in gasoline, car components, oil lurbicants, industrial, incinerator emissions, municipal wastewater discharges [4,5]. Contamination with the heavy metals is of major concern because of their toxicity and threat to human life and environment, particularly in light of the impact of high blood–Pb levels in children living in urban areas and the likelihood of this being caused by unintentional hand–mouth contamination while children play in a city street [2,6].

Since 40 years ago, one of the largest chemical and petrochemical industrial complexes in Jordan is located in Al- Hashimeyeh at Zarqa Governorate. The presence of a highway and several roads with heavy traffic influences enormously the environment of this area. There have been a number of previous studies on the distribution of heavy metal in road dust and soils in Jordan [7-10]. However, these studies focused only on limited locations, particularly road dusts from traffic areas collected from the urban part of Amman and total levels of these contaminants.

Environmental and health effects of trace metal contaminants in dust are initially dependent on the mobility and availability of the elements. Mobility and availability of these contaminants are functions of their chemical speciation and partitioning within or on dust

* Corresponding author : *kmashal@hu.edu.jo*

matrices. However, there is little information available; most studies on trace elements in street dust have concentrated on total levels with little emphasis on chemical forms. The identification of the main binding sites, phase associations of trace metals in soils, and sediments help in understanding the bioavailability of an element and the signature of multiple sources [11]. Most commonly, the sequential extraction procedures (SEP) are applied for solid phase speciation [12].

Recently, environmental concerns are growing and sustainable use of natural resources and risk and impact assessments are becoming increasingly important to avoid any human health impacts. A common approach to determine the origin of contamination is to identify the spatial relationships among environmental variables. Many recent studies were concerned with the identification of the sources of contamination either in soil, groundwater, rivers, streams, lakes, seas, or oceans [e.g.13], while other studies were focused on assessing the impact of industrial and agricultural uses on soil and groundwater quality [e.g.14].

Considering the above discussed facts, the primary objectives of the present study are to: (1) Determine average concentrations of heavy metals (Zn and Pb) in the urban soil and street dusts. (2) Define their natural or anthropogenic origin, and (3) Assess their mobility and bioavailability by solid phase speciation of these metals using sequential extraction.

2. Materials and Methods

2.1. Study Site

Al- Hashimeyeh is the most major industrial region at Zarqa Governorate in Jordan. It is located about 5 km eastern north of Zarqa city and 37Km to the east of the capital Amman (Figure1). The area of study is mainly consisting of highly dissected rocks with very gently undulating limestone parent material of Wadi esSir Limestone Formation, which represents the upper most of the Ajlun Group Formation [15].

Al- Hashimeyeh area is considered the vital part of Zarqa Governorate holding the largest industrial zones [16]. Since 40 years ago, the largest chemical and petrochemical industrial complexes in Jordan were built at the study area. At the same time, the presence of a highway and several roads with heavy traffic influences enormously the environment of this area.

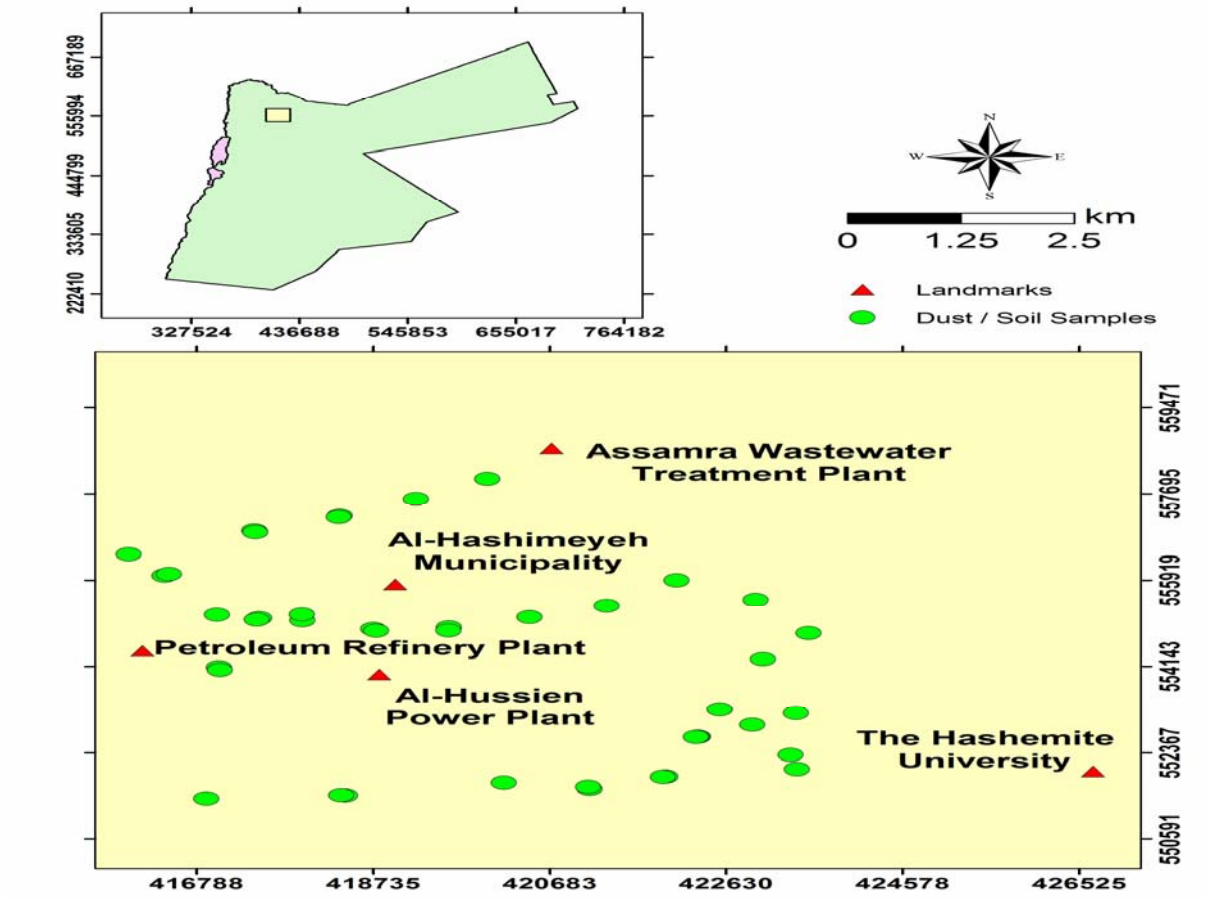

Figure 1. Study Area at the Al-Hashimeyeh Municipality.

2.2. Sample Collection and Preparation

Twenty six street dust samples were collected from both sides of the major streets in Al-Hashimeyeh in November 2005 (Figure1). Another seventeen topsoil samples were collected at a depth 0-15 cm. These urban soils were around one hundred meters away from the main streets (Figure1). The sampling was done using a plastic sweep and stored in mouth-closed polyethylene bags. In the laboratory, all the samples were air-dried, ground, and passed through a 2 mm sieve. The sampling procedure was intended to obtain a representative average sample made of mixing sub-samples from 4 points taken on the corners of a $1m^2$.

2.3. Soil Analyses

Several chemical analyses were conducted using appropriate analytical procedures which are reported in Methods of soil analysis, part 3 [17] as follow: Soil pHe and ECe were determined using soil past extraction. The Walkley- Black wet combustion method was used to determine the total soil organic carbon. Calcium carbonate ($CaCO_3$) was determined, using calcimeter method. Exchangeable cations and soil cation exchange capacity (CEC) were determined, using ammonium acetate. Active or amorphous iron oxide was determined by Tamm's Reagent. All chemicals were of analytical reagent grade unless otherwise indicated.

2.4. Sequential Extraction

Heavy metals of both Pb and Zn in all samples were fractionated by the sequential extraction procedure adopted by Tessier et al. [12] in duplicate. This procedure was selected because it is well documented, widely used, and it has been adapted to the study of soils and dusts [18]. Extractions were conducted in 50 ml polypropylene centrifuge tubes. Between each successive extraction, the supernatant was centrifuge at 6000 rpm for 15 min, and filtered. The chemical reagents, extraction conditions, and corresponding fractions used were as follows:

1. Exchangeable (EXC): 1 g of soil sample is shaken with 8 mL of 1 mol L^{-1} $MgCl_2$ at pH 7 for 1 h at room temperature.
2. Bound to carbonate (CA): the residue from the exchangeable is shaken with 8 mL of 1 mol L^{-1} CH_3COONa, adjusted at pH 5.0 with CH_3COOH for 5 h, at room temperature.
3. Bound to Fe–Mn oxides (Fe–Mn oxides): 20 mL of 0.04 mol L^{-1} NH_2OH . HCl in 25% CH_3COOH, pH 2.0, is added to residue and heated 96 ˚C in water bath for 6 h, with occasional shaking.
4. Bound to organic matter (OM): 3 mL of 0.02 mol L^{-1} HNO_3, 30% H_2O_2 (adjusted to pH 2.0), are added to the residue from the Fe-Mn oxide and heated at 85 ˚C in water bath, for 5 h. another 3.2 mol L^{-1} CH_3COONH_4 in 20% (v/v) HNO_3, is added and agitated for 30 min.
5. Residual (RES): 3 mL of HNO_3+$HClO_4$+HF is added to the residue from bound to OM under high pressure and heated at 170 ˚C.

The atomic absorption spectrophotometer was used for the determination of Pb, and Zn contents in all analyzed soil samples in both street dust and urban soils.

2.5. Statistical Analyses

Arithmetic means (AM) of the duplicate extraction results were calculated as well as the standard deviations (Std.). All the chemical responses, including both Pb and Zn heavy metals, were statistically investigated using JMP 5.01 program [19] platforms for multivariate correlations and regressions basing upon the direct and indirect effect of other independent soil chemical properties as pH, ECe, Cl^-, HCO_3^-, SO_4^{-2}, Na^+, Mg^{2+}, Ca^{2+}, %$CaCO_3$, %Organic Matter, CEC, and Fe concentration.

Both multivariate and partial multivariate analyses were adopted to investigate the direct and indirect effects of each independent chemical property on Pb and Zn concentrations. Multivariate analyses represent the strength of the linear relationships between each pair of responses. However, the partial multivariate analysis refers to the effect of each independent response on the heavy metals concentration, taking into account the presence of all other responses being constant (i.e. computes correlations using all the values for a given pair of variables in multi-linear regressions).

At the same time, for better understanding of the exact variability of both heavy metals and their relations to other chemical responses, multiple regression analyses were investigated for both heavy metals, using the stepwise regression technique as a critierion to eliminate the colinearity between responses and selecting a subset of effects for best prediction model. The technique is adopted when theory is modest and can not guide the selection of terms for a model especially in complex models that are regulated by many factors.

2.6. Spatial Analyses

The geospatial analyses performed in this study were achieved in three stages. The first stage involved the characterization of spatial distribution of both heavy metals at the study area, using geostatistical tools within the ArcMap within ArcGIS 9.2 program [20]. This stage was achieved by computing the semivariance clouds in all directions using Eq. 1 [21] and tested for isotropy.

$$\gamma_h = \frac{1}{2N}\sum_{i=1}^{N}\left[Z(x) - Z(x+h)\right]^2 \quad (1)$$

where γ_h is the semivariance, Z(x) the regionalized variable, and N(h) the number of pairs of sample data taken a distance (h) a part.

The second stage dealt with the modeling algorithm that involved the selection of the best empirical fit to represent the actual Pb and Zn spatial variations according to minimum Root Mean Square Error (RMSE). Parameter estimation of the final variogram model was implemented in this stage according to; (1) an independent range (distance of independency) for isotropical cases or major and minor ranges for non-isotropical cases, (2) a sill that represents the ordinary sample variance, and (3) a nugget representing the measurement error due to micro-regionalization. Generally, there are several theoretical models (e.g., linear, spherical, Gaussian or exponential) which were tested to represent spatial semivariance distribution. The selection of the best empirical semivariance model was based on both cross-validation test and provided smallest nugget value [22].

The final stage involved the estimation or prediction of Pb and Zn concentrations at unknown locations using kriging technique. Kriging is a simple linear weighted-interpolation scheme that assumes a weighing fraction for each point associated by each semivariance allocated at a known distance to the point under consideration by which the sum of all weight are set to be one.

3. Results and Discussion

3.1. Ordinary Statistics of Heavy Metal Concentrations

The mean concentrations and standard deviations of chemical properties and heavy metal (Pb and Zn) concentrations for all studied samples are shown in Table 1. The mean total concentrations of Pb and Zn in the street dust samples (115.3 and 228.2 $\mu g g^{-1}$, respectively) are much higher than the upper limits of their typical soil concentrations, 20 [23] and 90 $\mu g g^{-1}$ [24], respectively. This likely reflects an anthropogenic source, especially derived from traffic and industrial activities at the study area. As Zn is used as a vulcanization agent in vehicle tires [25], the higher wearing rate at the high temperature in Al-Hashimeyeh may contribute to the high Zn content in the street dust. Tetraethyland tetramethyl-lead have been added to gasoline from the mid-1920s to increase the octane rating of the fuel, but early 2008 production of leaded gasoline was stopped and all gasoline, at present, is unleaded. The lead is converted to PbO and PbO_2 which are then transformed into volatile $PbCl_2$, $PbBr_2$ and PbBrCl by addition of dichloro- or dibromo-methane to the gasoline [26].

In urban soils, the mean total concentration of Pb and Zn were 98.8 and 86.8 $\mu g g^{-1}$, respectively. In comparison to dust samples, the urban soil samples have lower Pb and Zn concentration. The high standard deviation values, and thus standard error means associated with most of the chemical properties, are indications of the complexity of the system. This huge variation in the data is an indication of spatial dependence attributed to either inherited conditions from human interferences with nature and/or induced by various sources of contaminations at the area.

3.2. Sequential Extraction

The distribution of heavy metals Zn, and Pb in the five fractions: exchangeable (EXC), carbonate (CA), Fe–Mn oxides, organic matter (OM) and residual (RES) fractions for all studied samples are summarized in Figure. 2. The results obtained show that the amounts of heavy metals extracted from each fraction vary widely. As with Pb, Zn distribution among the various solid phases depended on the soils characteristics (Figure 2). Total Zn concentrations in urban soils were particularly variable (49.3-185.2 mg kg^{-1}).

Significant amounts of Zn were associated with the residue and the Fe oxides fractions. The 44.0% of the total Zn was found in the Fe-Mn oxide fraction, whereas residual-Zn accounted for 51.3%. These Zn fractions are considered to be occluded inside the crystalline structures and not readily available for plant absorption. The findings are in agreement with those of Shuman [27], who reported that soil Zn was mainly associated with crystalline Feoxides and with the non-extractable residual fraction.

Table 1. Descriptive basic statistics of the chemical properties and heavy metal (Pb and Zn) in the studied samples.

Parameter	Sample	Mean	S.D.	Mean (S.E.)
pHe	Street dust	7.5	0.36	0.07
	Urban soil	7.7	0.42	0.10
ECe	Street dust	16.4	16.8	3.30
	Urban soil	13.5	12.2	3.00
Cl^- (meq/L)	Street dust	127.4	150.4	29.50
	Urban soil	114.8	127.4	31.00
HCO_3(meq/L)	Street dust	22.2	16.0	3.10
	Urban soil	8.7	1.8	0.43
SO_4^{2-} (meq/L)	Street dust	51.7	36.10	7.1
	Urban soil	21.6	12.44	3.0
Na^+ (meq/L)	Street dust	98.6	136.1	26.70
	Urban soil	95.9	148.45	36.00
K^+ (meq/L)	Street dust	8.7	22.6	4.4
	Urban soil	2.0	1.5	0.35
Ca^{2+} (meq/L)	Street dust	62.83	37.4	7.3
	Urban soil	64.0	71.97	17.5
Mg^{2+} (meq/L)	Street dust	44.0	56.5	11.1
	Urban soil	28.7	36.6	8.9
$\%CaCO_3$	Street dust	52.8	7.2	1.4
	Urban soil	37.0	8.9	2.2
%OM	Street dust	3.0	3.1	0.61
	Urban soil	1.3	0.50	0.12
CEC (cmol/kg)	Street dust	3.7	1.3	0.25
	Urban soil	7.8	3.0	0.71
Fe (mg/kg)	Street dust	2105.2	315.4	61.86
	Urban soil	721.9	333.4	80.85
Pb (mg/kg)	Street dust	115.3	95.2	18.67
	Urban soil	98.8	105.6	25.60
Zn (mg/kg)	Street dust	228.1	197.7	38.78
	Urban soil	86.86	34.7	8.43

Zinc associated with the chemically reactive fractions such as the Zn in exchangeable and adsorbed forms generally represented less than 10% of the total Zn in the studied soils. Similarly, Hseu [28] reported that Zn associated with the exchangeable and carbonate fractions in native tropical soils varied from approximately 2% to 6% of total Zn.

The greater the amounts of active sites for Zn sorption (mainly Mn and Fe oxides), the less Zn was found in the exchangeable fraction. Usero et al. [29] using also the Tessier method on four marine sediments found that Zn is bound to iron–manganese oxides. Maskall and Thornton [30] indicate that in contaminated soils, Zn is mainly found in the residual fractions. The results for dust street are similar, but with less association with the residual fraction and a higher percentage with the Fe oxides (65%).

Lead in the street dust and urban soil samples are mainly associated with the Fe-Mn oxides with 82.1, and 68.5% respectively. A study by Flores-Rodriguez et al.[31]

on the bioavailable and stable forms of roadside dust and soils found that the Fe-Mn crystalline hydroxides and carbonate fractions of suspended solids are the most important in terms of metal binding, irrespective of the heavy metal. This finding is in general agreement with the results of this study for lead. Studies on the fractionation of roadside soils have suggested that lead has a high affinity for carbonates or iron– manganese oxides [32]. As such, lead is generally considered to be immobile within the soil profile, primarily as a result of its small soluble component. It seems that the same fractionation profile exists for lead in street dust and urban soils.

Environmental risks of Pb and Zn were evaluated using the risk assessment code (RAC). The RAC assesses the availability of metals in solution by applying a scale to the percentage of sediments that can reduce metals in the adsorptive and exchangeable and bound to carbonate fractions [33]. These fractions are considered to be weakly bonded metals, which may equilibrate with the aqueous phase, and thus become more rapidly bioavailabile [34]. The results of the present study show that Zn in street dust poses a medium risk with 15% exists in exchangeable and carbonate fractions. While the percentage of urban Zn in exchangeable and carbonates fractions is 1%, posing a low environmental risk. The concentrations of Pb in urban and street dust samples pose a low risk to the environment with 8% and 9% respectively, exists in exchangeable and carbonate fractions. It is possible to suggest the sequence of mobility for Pb, Zn, in the street dust samples is as the following Zn>Pb while in urban soil it is as the following Pb>Zn.

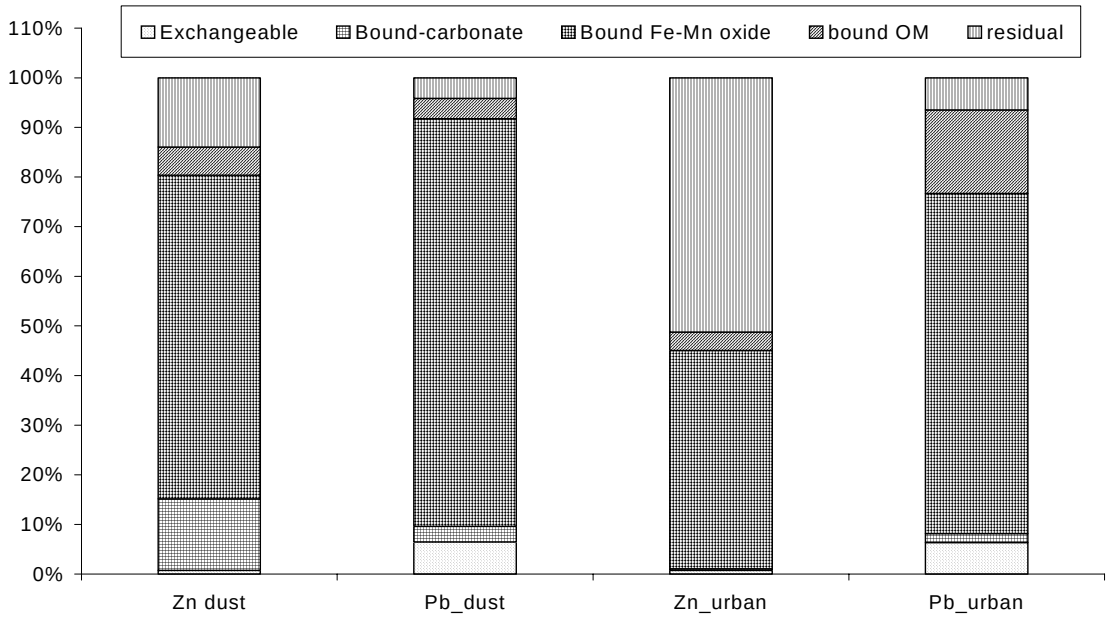

Figure 2. Percentage distributions of Zn and Pb in the studied soils .

3.3. Multivariate Analyses

Processes of metal mobilization–inmobilization are affected by a variety of soil properties [35]. To examine this influence, correlations between pH, carbonate, organic matter and contents of Zn and Pb in the five chemical phases of the sequential extraction have been established for all soils.

According to multivariate correlation analysis (Table 2), Pb concentration actually has a positive significant correlation with Zn of about 51% and inversely correlated to CEC with correlation coefficient of 34%. At the same time, Zn shows a high correlation with organic matter, hydrocarbonates and Fe with correlation coefficients of 58%, 46%, and 43%, respectively. Those relations represent the coefficient of determinations of single pair linear relations. The inter relations between the independent variables agree with the chemical analyses perspective such as the correlations of EC with Cl, SO_4^{2-} with EC, and Na^+ with Cl^-.

On the other hand, the partial multivariate correlation analysis (Table 3) represents the correlation corresponding to the presence of all chemical factors together as a multiple regression. The partial analysis indicates that sulfate, followed by Mg^{2+}, and CEC have a significant negative effect on Pb, while pHe, Cl^-, and HCO_3^- have significant positive effects of Pb. Also, Zn concentration is highly correlated to organic matter with correlation coefficient of 75% followed by K^+ content with a negative correlation coefficient of 59% which proves that Zn is highly associated with organic sources and competes by presence of potassium on the exchangeable sites.

3.4. Prediction Modeling

According to stepwise analysis using the backward strategy (Figure 3), the final effective significant linear prediction model for Pb concentration (R^2 of 56.2%, RMSE of 71.40 ppm) was as follows:

$$Pb(= -512.85 + 82.46\,pH + 0.85\,Cl^- + 4.25\,HCO_3^- - 2.62\,SO_4 - 1.44\,Mg - 10.65\,CEC + 0.23\,Zn. \quad (2)$$

This model suggests that the colinearity between chemical responses was removed, ending by the major significant individuals of pHe, Cl^-, HCO_3^-, SO_4, Mg, CEC, and Zn. Therefore, Pb contamination at the study area can

Table 2: Multivariate correlation analysis for some chemical response.

	pHe	ECe	Cl^-	HCO_3^-	SO_4^{2-}	Na^+	K^+	Ca^{2+}	Mg^{2+}	% $CaCO_3$	%OM	CEC	Fe mg/kg	Pb mg/kg	Zn mg/kg
pHe		-0.46	-0.45	-0.01	-0.22	-0.46	-0.04	-0.49	-0.32	-0.22	0.06	0.25	-0.26	0.23	0.28
ECe	-0.46		0.97	0.29	0.63	0.93	0.32	0.65	0.78	0.20	0.21	-0.24	0.07	0.12	-0.08
Cl^-	-0.45	0.97		0.28	0.63	0.91	0.32	0.65	0.83	0.16	0.19	-0.21	0.02	0.11	-0.10
HCO_3^-	-0.01	0.29	0.28		0.74	0.15	0.78	0.09	0.58	0.31	0.83	-0.40	0.49	0.18	0.46
SO_4^{2-}	-0.22	0.63	0.63	0.74		0.48	0.48	0.28	0.63	0.49	0.49	-0.42	0.40	0.03	0.20
Na^+	-0.46	0.93	0.91	0.15	0.48		0.20	0.75	0.70	0.13	0.11	-0.15	0.03	0.11	-0.11
K^+	-0.04	0.32	0.32	0.78	0.48	0.20		-0.01	0.69	0.08	0.88	-0.21	0.20	0.11	0.25
Ca^{2+}	-0.49	0.65	0.65	0.09	0.28	0.75	-0.01		0.53	-0.04	-0.07	-0.09	0.13	0.06	-0.11
Mg^{2+}	-0.32	0.78	0.83	0.58	0.63	0. 70	0.69	0.53		0.08	0.54	-0.20	0.19	0.06	0.07
%$CaCO_3$	-0.22	0.20	0.16	0.31	0.49	0.13	0.08	-0.04	0.08		0.18	-0.68	0.65	0.01	0.13
%OM	0.06	0.21	0.19	0.83	0.49	0.11	0.88	-0.07	0.54	0.18		-0.28	0.37	0.21	0.58
CEC	0.25	-0.24	-0.21	-0.40	-0.42	-0.15	-0.21	-0.09	-0.20	-0.68	-0.28		-0.62	-0.34	-0.33
Fe conc.	-0.26	0.07	0.02	0.49	0.40	0.03	0.20	0.13	0.19	0.65	0.37	-0.62		0.09	0.43
Pb conc.	0.23	0.12	0.11	0.18	0.03	0.11	0.11	0.06	0.06	0.01	0.21	-0.34	0.09		0.51
Zn conc.	0.28	-0.08	-0.10	0.46	0.20	-0.11	0.25	-0.11	0.07	0.13	0.58	-0.33	0.43	0.51	

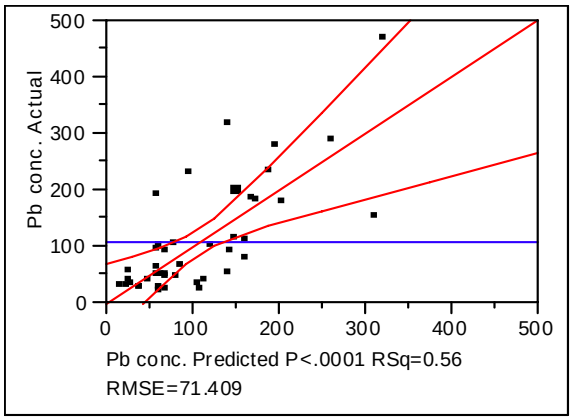

Figure 3. Predicted Model of Pb concentration using the Stepwise linear regression .

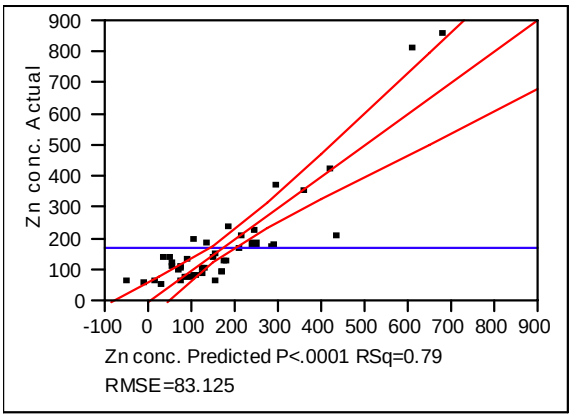

Figure 4. Predicted Model of Zn concentration using the Stepwise linear regression.

be predicted using the former multi-regressive model with negligible error.

On the other hand, Zn contaminants prediction model (Figure 4) estimated using stepwise regression (R^2 of 78.7%, RMSE of 83.12 ppm) suggests the effectiveness of K, $CaCO_3$, OM, Fe, and Pb as inter-related to Zn loads.as follows:

$$Zn = 4.66 - 9.91\ K\ - 2.72\ CaCO_3 + 91.47\ OM + 0.05\ Fe\ + 0.56\ Pb \quad (3)$$

It is important to remark that the presence of both heavy metals in both prediction models is a clear indication of the direct correlation of both metals and approves the assumption of being both related to same subjected pollutant sources..

3.5. Spatial Modeling

According to spatial analysis, the Pb contamination at the study area appeared to have a nonisotropic behavior that is skewed due to heavy weight tail. However, the variability of Pb concentration was exponentially behaved in space with a major range (range of independence) of 78.6 km in 22.5 degree direction, minor range

(perpendicular to major range) of 12.1 km and a partial sill (variance at which the semivariogram levels) of 0.21 ppm holding a nugget (smallest error that can not be detected due to smallest sampling spacing or zero separation distance) of 0.23 ppm as described in the following equation:

$$\gamma(h) = C_0 + C\ [1\text{-}exp(\text{-}h/A)] \quad (4)$$

where

h = lag class interval,

C_0 =0.23= nugget variance

C = 0.21 =structural variance

$A = A_1^2[\cos 2(\theta - \phi)] + A_2^2[\sin 2(\theta - \phi)]$

A_1 =78.6 km = range parameter for the major axis (ϕ)

A_2 = 12.1 km = range parameter for the minor axis ($\phi + \pi/2$)

ϕ = 22.5 = angle of maximum variation

θ = angle between pairs

Using point kriging with 5 neighbors surrounding technique, the final krigged map is given at Figure 5 with a

RMSE of 66.78. Final krigged map for Pb distribution in space indicates that Pb contamination is concentrated at the southern east territory of the study area and decreases towards the main Al-Hashemyiah city; and started again to rise near by the northern west of the study area near the power sanitation plant. The high Pb levels at the southern east territory was mainly due to the presence of the high way that is mainly used to transport and ship petroleum across the kingdom.

Similarly, Zn contamination is behaving nonisotropiclly with a high skweness which was exponentially distributed in space with a major range of 78.6 km in 289 degree direction, minor range of 12.1 km and a partial sill of 0.27 ppm holding a nugget of 0.18 ppm (Figure 6) as described by the following equation:

$$\gamma(h) = C_0 + C[1-\exp(-h/A)] \quad (5)$$

where
h = *lag class interval,*
C_0 = *0.18 = nugget variance*
C = *0.27 =structural variance*
$A = A_1^2[\cos 2(\theta-\phi)] + A_2^2[\sin 2(\theta-\phi)]$
A_1 = *78.6 km = range parameter for the major axis* (ϕ)
A_2 = *12.1 km = range parameter for the minor axis*
ϕ = *289 = angle of maximum variation*
θ = *angle between pairs*

According to the final krig distribution maps, Zn is behaving similarly to Pb in space by which both have a very high spatial dependence reflected by having high similar major and minor ranges. However, the differences in the non-iostropical variance directions in both spatial distributions of the heavy metals may not be attributed to differences in pollution sources, but rather may indicate the variability in the interactions with nature as explained by the sequential analyses.

4. Conclusion

This study served to evaluate the distribution, retention, and release of Zn and Pb in selected street dust and urban soil samples of the Al-Hashimeyeh municipality. The results obtained are a first approach to assess the environmental levels of these metals in function of their availability to the ecosystems.

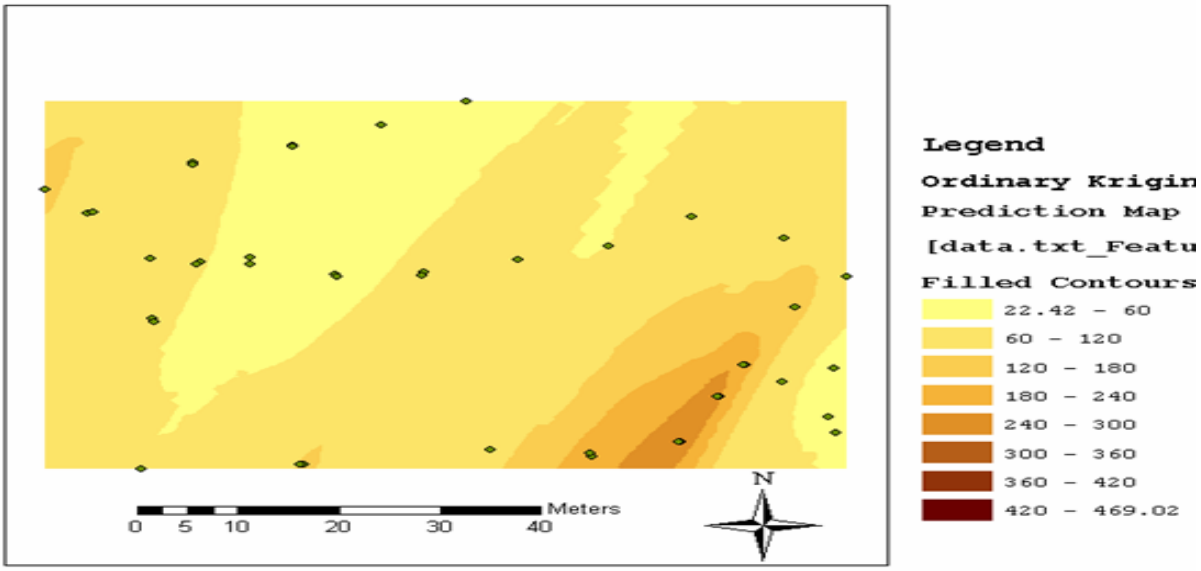

Figure 5. Spatial Krigging for Pb concentration of the studied samples in Al-Hashimeyeh.

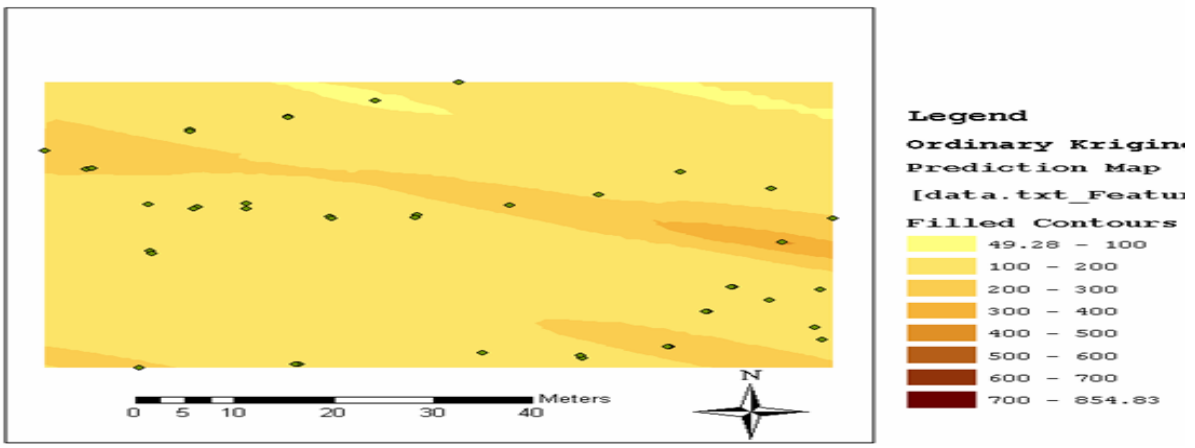

Figure 6. Spatial Krigging for Zn concentration of the studied samples in Al-Hashimeyeh.

Of the total amounts of Zn and Pb only very small proportions were extracted in a readily mobile form. Therefore, these low amounts suggest that metal migration downwards would be limited. The largest proportions for Zn and Pb were extracted in the iron oxide fraction, in which metals are strongly retained in the soil minerals. Nevertheless, this is not expected in the agroecosystems of our region because soil conditions are highly alkaline with a high buffering capacity due to carbonates that can also contribute to retain heavy metals. Further, the high metal loads allocated at or close to industrial zones suggest that major contamination sources were traffic emissions from heavy vehicles along the highways and the industrial activities allocated within the study area.

5. Acknowledgments

We thank the Deanship of Research and Graduate Studies at the Hashemite University who funded this project. Also we thank the center of environmental studies at the Hashemite University for their Help to analyze projects' samples. We wish to thank Hana Al-Nounah for her sampling and analytical work during all stages of the project.

References

[1] F.B. Culbard, I. Thornton, J. Watt, M. Wheatley, S. Moorcroft, M. Thompson, "Metal contamination in British urban dusts and soils". J. Environ. Qual., Vol. 17, 1988, 226-234.

[2] J.W.C. Wong, N.K. Make, "Heavy metals pollution in children playgrounds in Hong Kong and its health implications". Environ. Technol., Vol. 18, 1997, 109-115.

[3] P. Lee, Yu. Youn-Hee, Y. Seong-Taek, M. Bernhard, "Metal contamination and solid phase partitioning of metals in urban roadside sediments". Chemosphere, Vol. 60, 2005, 672-689.

[4] R.A. Sutherland, C.A. Tolosa, "Multi-element analysis of road-deposited sediment in an urban drainage basin, Honolulu, Hawaii". Environmental Pollution, Vol. 110, 2000, 483–495.

[5] H. Yu, "Environmental carcinogenic polycyclic aromatic hydrocarbons: photochemistry and phototoxicity". Journal of Environmental Science and Health-Part C, Vol. 20, 2002, 149–183

[6] L.S. Hughes, G.R. Cass, J. Gone, M. Ames, I. Olmez, "Physical and chemical characterization of atmospheric ultrafine particles in the Los Angeles area". Environ. Sci. Technol, Vol. 32, 1998, 1153–1161.

[7] Q. Jaradat, K. Momani, "Contamination of roadside soil plant, and air with heavy metals in Jordan: A comparative study". Turk. J. Chem., Vol. 23, 1999, 209:220.

[8] A.G. Jiries, H.H. Hussein, Z. Halash, "The quality of water and sediments of street runoff in Amman, Jordan". Hydrological Processes, Vol. 15, 2001, 815– 824.

[9] Jiries A.G. Vehicular contamination of dust in Amman, Jordan. The Environmentalist 2003; 23:205-210.

[10] O.A. Al-Khashman, "Heavy metal distribution in dust, street dust and soils from the work place in Karak Industrial Estate, Jordan". Atmospheric Environment, Vol. 38, 2004, 6803-6812.

[11] F.M.G. Tack, M.G. Verloo, "Chemical speciation and fractionation in soil and sediment heavy metal analysis: a review". International Journal of Environmental Analytical Chemistry, Vol. 59, 1995, 225–238.

[12] A. Tessier, P.G.C. Campbell, M. Bisson, "Sequential extraction procedure for the speciation of particulate trace metals". Analytical Chemistry, Vol. 51, 1979, 844–850.

[13] P. Maillard, N. Santos, "A spatial–statistical approach for modeling the effect of non-point source pollution on different water quality parameters in the Velhas river watershed—Brazil". J. Environ. Manage. Vol. 86, 2008, 158–170.

[14] M. Milovanovic, "Water quality assessment and determination of pollution sources along the Axios/Vardar River, Southeastern Europe". Desalination, Vol. 213, 2007, 159–173.

[15] M.I. Al-Qinna, A.S. Mohammed, N.S. Ziad, "Effect of carbonates and gravel contents on hydraulic properties in gravely-calcareous soils. Dirasat, Agricultural Sciences, Vol. 35, 2008, 145-158.

[16] Department of Statistics (DOS). Estimation of population by Governorate. Amman, Jordan, 2004.

[17] Sparks DL. Methods of Soil Analysis, Part 3: Chemical Methods. 2nd ed. Madison: SSSA; 1996.

[18] A. Navas, H. Lindhorfer, "Geochemical speciation of heavy metals in semiarid soils of the central Ebro Valley (Spain)". Environment International, Vol. 29, 2003, 61-68.

[19] JMP 5.1 user manual. Statistics and graphics guide. North Carolina: SAS Institute; 2005.

[20] ArcView GIS user manual. Version 9.2. USA: ESRI-Environmental systems research institute; 2006.

[21] Selker JS, Keller CK, McCord JT. Vadose zone processes. Florida: Lewis Publishers/CRC Press LLC; 2009.

[22] Goovaerts P. Geostatistics for natural resources evaluation. New York: Oxford University Press; 1997.

[23] Grimshaw HM, Allen SE, Parkinson JA. Nutrient elements. In: Allen SE, editor. Chemical Analysis of Ecological Materials, London: Blackwell Scientific Publications; 1989, p. 81–159.

[24] Bowen HJM. Environmental chemistry of the elements. New York: Academic Press; 1979.

[25] Alloway BJ. Heavy metals in soils. London: Blackie; 1990.

[26] N. Sezgin, O. Zcan, H.K. Demir, G.S. Nemliog˘ lu, C. Bayat, "Determination of heavy metal concentrations in street dusts in Istanbul E-5 highway". Environment International, Vol. 29, 2003, 979–985.

[27] L.M. Shuman, "Fractionation method for soil microelements". Soil Sci., Vol. 140, 1985, 11–22.

[28] Z.Y. Hseu, "Extractability and bioavailability of zinc over time in three tropical soils incubated with biosolids". Chemosphere, doi:10.1016/j.chemosphere 2004;10.042, 2005.

[29] J. Usero, M. Gamero, J. Morillo, I. Gracia, "Comparative study of three sequential extraction procedures for metals in marine sediments". Environ. Int., Vol. 24, 1998, 487– 97.

[30] J.E. Maskall, I. Thornton, "Chemical partitioning of heavy metals in soils, clays and rocks at historical lead smelting sites". Water Air Soil Pollut., Vol. 108, 1998, 391– 409.

[31] J. Flores-Rodriguez, A.L. Bussy, D.R. Thevenot, "Toxic metals in urban runoff: physico-chemical mobility assessment using speciation schemes". Water Sci. Technol., Vol. 29, 1994, 83–93.

[32] F.Y. Lee, J. Touray, "Characteristics of a polluted artificial soil located along a motorway and effects of acidification on the leaching behaviour of heavy metals (Pb, Zn, Cd)". Water Res., Vol. 11, 1998, 3425– 35.

[33] Perin G, Craboledda L, Lucchese M, Cirillo R, Dotta L, Zanetta ML, Oro AA. Heavy metal speciation in the sediments of northern Adriatic Sea: A new approach for environmental toxicity determination. In: Lakkas TD, editor. Heavy Metals in the Environment, Edinburg: CEP Consultants; 1985, p. 454-456.

[34] R. Pardo, E. Barrado, I. Perez, M. Vega, "Determining and association of heavy metals in sediments of the Pisucrga river". Water Res., Vol. 24, 1990, 373–379.

[35] Jones LHP, Jarvis SC. The fate of heavy metals. In: Greenland DJ, Hayes MHB, editors. The chemistry of soil processes. New York, USA: Wiley; 1981, p. 593–620.

JJMIE

Volume 3, Number 2, June. 2009
ISSN 1995-6665
Pages 151 -156

Jordan Journal of Mechanical and Industrial Engineering

Mathematical Model of Inductive Effect on the Multi-motors Synchronization Systems

Ali Akayleh *, Samarai Ahmed, Al-Soud Mohammed

Department of Electrical Engineering, Tafila Technical University, Tafila - Jordan.

Abstract

Systems of synchronous rotation with AC machines depend on the equality of speed of two or more induction motors (mechanical or non mechanical-shaft connected) with the existence of load differences allocated on these shafts. The most popular ones among non-mechanical-shaft synchronization systems are the synchronization systems with auxiliary machines, electrical shaft systems, and the electromagnetic working shaft systems. In this work, using MATLAB – SIMULINK program, we suggest a mathematical model which represents a synchronous drive with electromagnetic working shaft system. The model will be tested with two similar induction motors 5hp, 50 Hz, 380 line voltage. Principle of operation and advantages related to the synchronous capability and recovery time for the electromagnetic working shaft system in deferent operational stats were also studied.

Keywords: Mathematical Model; Synchronous Capability; Induction Motors; Electromagnetic Shaft

1. Introduction

Systems of synchronous rotation are most used in cranes, cutting tool machines, and lifting machines [1]. The main performance of synchronization systems is very much related to the synchronous capability (speed synchronization, with maximum different loads on the motors shafts), and the required synchronization process time (recovery time).

When difference in load distribution is high, the system requires more synchronous capability. Therefore, the synchronous capability should be determined for any change in rated load, variation in load distribution, and rated power parameters. Accordingly, synchronous capability differs according to the connection, which links up the motors in the system. If the connection is direct mechanical one, then synchronous capability is unlimited. If the connection is non-mechanical, then synchronous capability will depend on the load distribution and the type of the control element connected between the main motors.

Electromagnetic working shaft system is recently the most applicable system compared to other synchronization systems. Each motor in this system is connected to a wounded coil on steel cylinder (inductive reactance element), which is very similar to transformer connections, where primary coils are connected to one motor and the secondary to the other, figure (1).

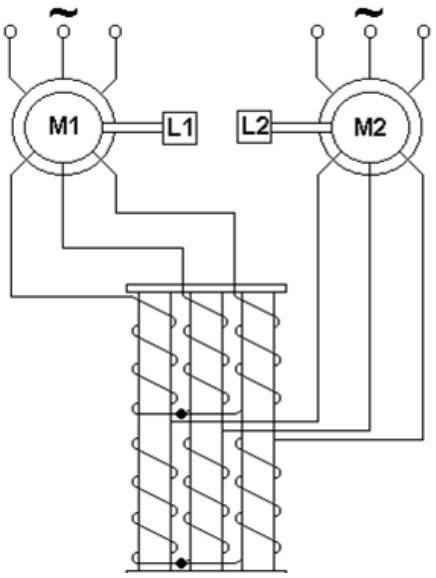

Figure1. Electromagnetic working shaft system.

For the electromagnetic working shaft system, the inductive reactance element parameters and dimensions mainly depend on the rated motors power and loads [2]. If the rotor currents flow inside the inductive reactance from both sides, and electromagnetic connection is generated between them, the main motors' coils fall under a correspondent and continuous influence of the power, where a change in one current of any of the motors leads to a change of the current motor in the other. Therefore the system principle of operation depends on the electromagnetic transformation of energy.

* Corresponding author. akayleh_em@yahoo.com.

If the loads on motors shafts are equal, $(L_1 = L_2)$, the rotor currents moving inside the inductive reactance are also equal, and the electromagnetic fields generated in those rotors are equal in quantity and are opposite in direction, so there will be no connection between the rotors, and the motors are operating as individual induction motors.

If the loads and the motors shafts are not equal $(L_1 \neq L_2)$, then the rotor currents and the electromagnetic fields will also change. This will lead to an electromagnetic connection amongst the inductive element of the rotor's coils that will be used to synchronization of the motors speed.

When the system is started with any load difference, there will be a great difference in the starting currents on the inductive reactance terminals, this difference will cause the smallest loaded motor to operate as a generator causing a decrease in the electromotive force value, and therefore the motor speed will decrease rapidly. Therefore the current will increase. The increased current will reverse the previous operation.

This variation will cause a system vibration. And to overcome this effect, the system should start when the loads are equal.

2. System Equivalent Circuit

To derive the control equations for the system, it is possible to use the simplified equivalent circuit given in Figure (2) [3].

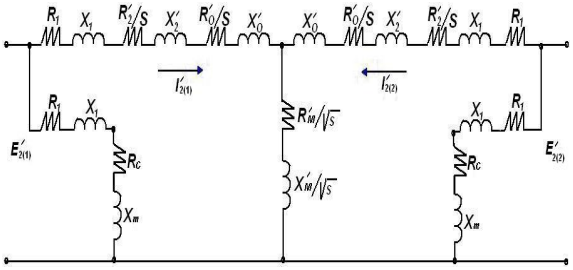

Figure 2. System equivalent circuit.

Where:

R_1, X_1 : Stator resistance and inductive reactance of first and second motors.

R'_2, X'_2 : Rotor Resistance and inductive reactance of first and second motors.

R'_o, X'_o : Resistance and inductive reactance of inductive element.

R'_M, X'_M : Resistance and inductive reactance of magnetizing circuit of inductive element.

R_c, X_c : Resistance and inductive reactance of magnetizing circuit of induction motor.

$E'_{2(1)}, E'_{2(2)}$: Rotor phase voltage in the first and the second motors.

$I'_{2(1)}, I'_{2(2)}$: Rotor current of the first and the second motors.

S: Slip.

When the loads become equal, the rotors and stators phase shift will be equal too $(\alpha_1 = \alpha_2)$ and $(\Delta\alpha = 0)$.

Where:

$$T_{A(1)} = \frac{\left\langle R_1 + \frac{R'_o + R'_2}{S} + \frac{2R'_M}{\sqrt{S}} \right\rangle^2 . \langle 1 + \cos\Delta\alpha \rangle}{\left\langle R_1 + \frac{R'_o + R'_2}{S} + \frac{2R'_M}{\sqrt{S}} \right\rangle^2 + \left\langle X_k + X'_o + \frac{2X'_M}{\sqrt{S}} \right\rangle^2}$$

α_1, α_2 . Phase angles between the stator and rotor windings of main motors.

From the equivalent circuit Figure (2), the balance equations for the phase rotor voltage can be calculated as follows:

$$E'_{2(1)} = I'_{2(1)}\left[Z_d + Z_M\right] + I'_{2(2)}Z_M \quad (1)$$

$$E'_{2(2)} = I'_{2(2)}\left[Z_d + Z_M\right] + I'_{2(1)}Z_M \quad (2)$$

Where:

$$Z_d = (R_1 + \frac{R'_2}{S} + \frac{R'_o}{S}) + J\left(X_k + X'_o\right)$$

$$Z_M = \frac{R_M}{\sqrt{S}} + j\frac{X_M}{\sqrt{S}} \quad , \quad X_k = \left(X_1 + X'_2\right)$$

From (1 and 2) the rotor current for the first motor can be calculated as:

$$I'_{2(1)} = \frac{1}{2}\left[\frac{E'_{2(1)} + E'_{2(2)}}{Z_d + 2Z_M} + \frac{E'_{2(1)} - E'_{2(2)}}{Z_d}\right] \quad (3)$$

Based on [4 and 5], if the first motor is determined as a reference motor of the system, so; $(E'_{2(1)} = E'_2, E'_{2(2)} = E'_2 e^{j\Delta\alpha})$, and the torque of the first motor can be calculated as:

$$T_1 = \frac{m E'^2_2}{2\omega_o}\left[\dot{I}'_{2(1)} + I'_{2(2)}\right] \quad (4)$$

Where:

m: number of phase, $\dot{I}'_{2(1)}$. Conjugate value of the first rotor current.

If we add the value of rotor current $(I'_{2(1)})$ and its conjugate $(\dot{I}'_{2(1)})$, and after some transformations the torque (equation 4) will be:

$$T_1 = \frac{m E'^2_2}{2\omega_o}\left[T_A + T_S . Sin\,\Delta\alpha\right] \quad (5)$$

Where:

$T_A = T_{A(1)} + T_{A(2)}$ - Asynchronous part of the torque.

$T_S = T_{S(1)} + T_{S(2)}$ - Synchronous part of the torque.

$$T_{S(1)} = \frac{\left\langle X_k + X'_o + \frac{2X'_M}{\sqrt{S}} \right\rangle^2}{\left\langle R_1 + \frac{R'_o + R'_2}{S} + \frac{2R'_M}{\sqrt{S}} \right\rangle^2 + \left\langle X_k + X'_o + \frac{2X'_M}{\sqrt{S}} \right\rangle^2}$$

$$T_{A(2)} = \frac{\left\langle R_1 + \frac{R'_o + R'_2}{S} \right\rangle . \langle 1 - \cos \Delta\alpha \rangle}{\left\langle R_1 + \frac{R'_o + R'_2}{S} \right\rangle^2 + \langle X_k + X'_o \rangle^2}$$

$$T_{S(2)} = \frac{\langle X_k + X'_o \rangle^2}{\left\langle R_1 + \frac{R'_o + R'_2}{S} \right\rangle^2 + \langle X_k + X'_o \rangle^2}$$

If the second motor is determine as a reference ($E'_{2(2)} = E'_2$ and $E'_{2(1)} = E'_2 e^{j\Delta\alpha}$), then the motor torque can be determined similar to the first motor but with negative part of synchronous torque [5].

$$T_2 = \frac{mE'^2_2}{2\omega_o}\left[T_A - T_S . Sin\Delta\alpha\right] \quad (6)$$

3. System Block Diagrams

Using the main equivalent circuit equations, rotational dynamic torque equations, angular speed, and angular positions equations, the mathematical model of the electromagnetic working shaft system has been built [6]. This model (see figure 3) consists of three blocks each of them has a specific functions.

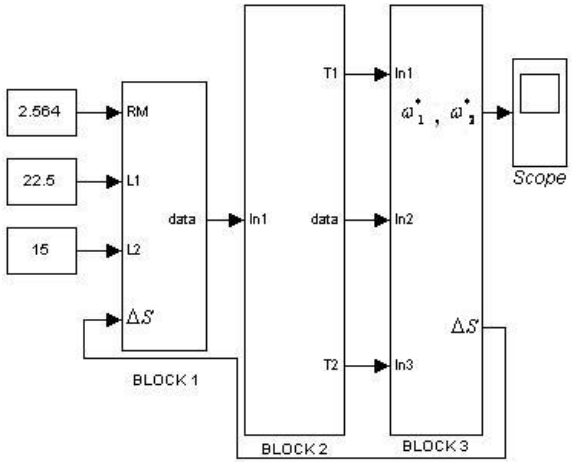

Figure 3. System block diagram.

3.1. Block 1 (General Data Block)

This block was built using difference basic data such as the similar induction motors parameters, (5hp, 4 pole 50 Hz, VL=380*V*, *R1=1.115 Ω*, R'_2 *=1.083 Ω*, $X_1 = X'_2$ *= 2.252 Ω*, X_c *= 76.8 Ω., J=0.02 kg.m²)*, inductive element parameters (R'_o, X'_o, X'_M), inputs (R'_M , *L1, L2)*, feedback (ΔS . $\Delta\alpha$, *S1, S2*) , and parameters.

Where:

L1. Load torque of first motor. *L2*. Load torque of second motor.

3.2. Block 2 (System Main Equations Block)

The main input of this block is the output data signal of general data block. Using this data, the torque equations, *(5 and 6)* were built Figure (4).

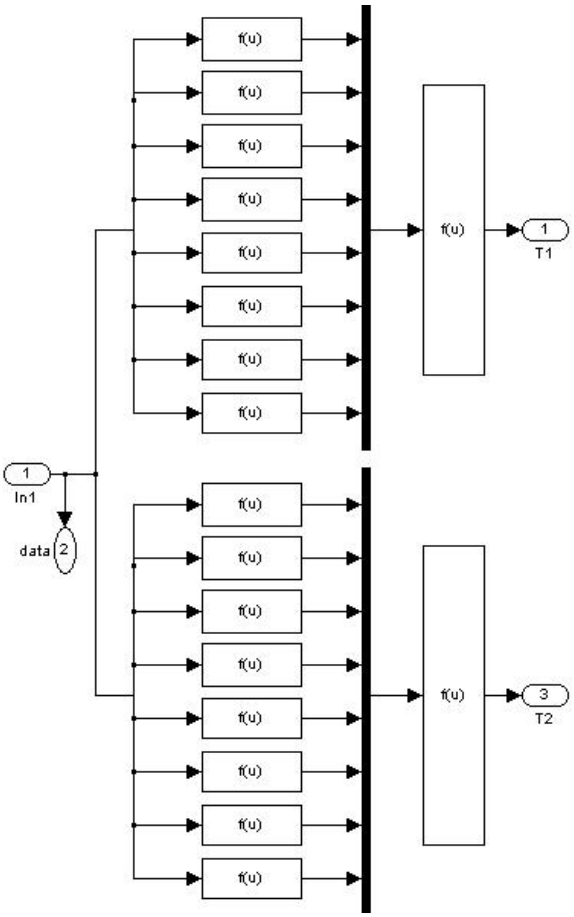

Figure 4. System main equations block

3.3. Block 3 (Error Calculation Block)

The error calculation block input consists of torque equations (*T1, T2*), load torque value *(L1, L2)*, and general data signal incoming from the first block Using dynamic torque equation:

($T_{in} - T_L = J\frac{d\omega}{dt}$) and relationships between angular speed, difference between windings phase shift and slip ($\omega_1, \omega_2, \Delta\alpha, S_1 S_2$), the synchronous process, synchronous capability and recovery time of the system are calculated.

The above mentioned output values of this block diagram are presented as the main system response and as the feedback values, which goes back to first block.

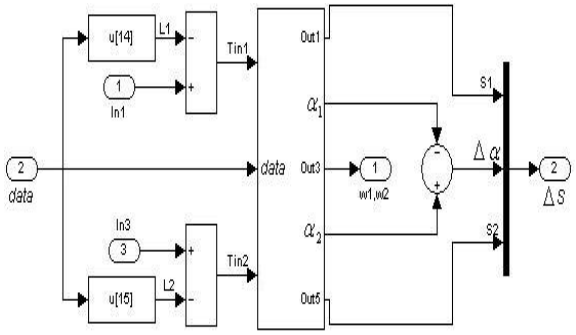

Figure 5. Error calculation block.

4. System Operation and Test

According to [6], and based on practical applications of electromagnetic working shaft systems, the inductive reactance element power factor ($COS\alpha$) ranges between 0.7 and 0.85, and relationships inductive reactance parameters with resistance R'_M are joined .

$$X'_M = \tan\alpha . R'_M$$

$$X'_o = R'_o = (0.1 - 0.2) R'_M$$

For our system model, using specific method [6], the model will be tested with the below inductive reactance element parameters and dimensions:

R'_M : Rated magnetizing resistance = 2.564 Ω.
La: Axial distance between rods = 243mm.
D: Diameter of the steel rod =125 mm.
Lc: Length of steel core = 496mm.
Oh: Length of turn (half steel rod) =238 mm.

Operation of the system model can represent the inductive reactance magnetizing resistance R'_M effect on the synchronous capability and recovery time of the system.

If the magnetizing resistance is equal to zero, (R'_M = 0), and the loads on the shafts are not equal $(L_1 = 2L_2)$, there will be no relationship between the motors in the control system, and the motors will operate as individual induction motors, Figure (6).

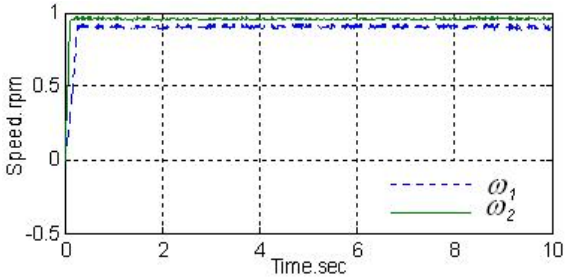

Figure 6. Speed response without rotor connection.

If the magnetizing resistance is not equal to zero, ($R'_M \neq 0$), and the loads on the shafts are equal $(L_1 = L_2)$, the electromotive forces generated in inductive reactance coils will be equal in quantity and will be opposite in direction. Therefore, the motors will also operate as individual motors with equal speeds, $(\omega_1 = \omega_2)$,Figure (7).

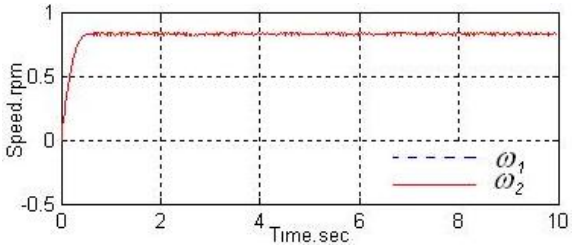

Figure 7. Speed response when equal loads.

If the magnetizing resistance is not equal to zero ($R'_M \neq 0$), and the loads on the shafts are not equal, $(L_1 \neq L_2)$, and then the electromotive forces generated in inductive reactance coils will be not equal. This will produce energy difference in the common rotor circuit, $(\Delta E = E'_{2(2)} - E'_{2(1)})$.

This energy will decrease the speed of the motor with the lowest effect until it leads to equality of speeds in both motors. In this case, the system will be tested with three values (0.5, 1.0, 1.5) $R'_M(Rated)$, Figure (8).

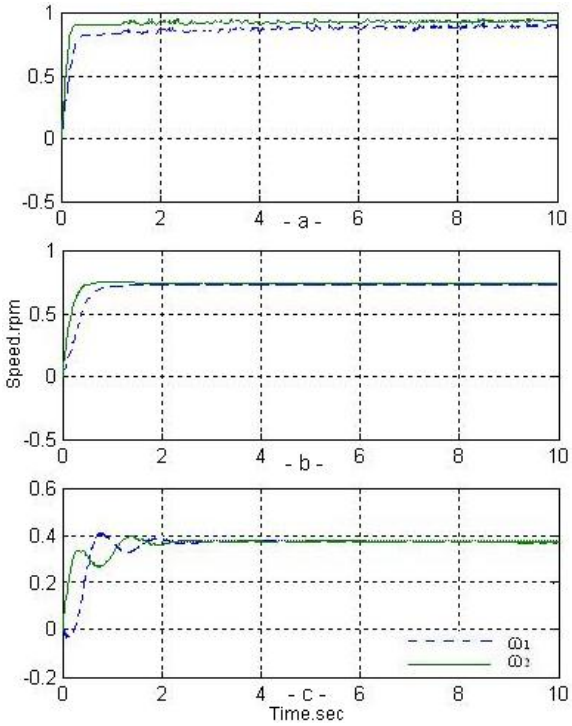

Figure 8. Speed response when $(L_1 = 1.5L_2)$
(a) $0.5R'_M(Rated)$, (b) $R'_M(Rated)$
(c) $1.5R'_M(Rated)$.

Comparing the speed system response, we can see the real role of magnetizing resistance on the synchronization process of the system. For our case, the best synchronous capability and recovery time can be determined only when using rated magnetizing resistance, (see figure 8-b).

Figure (9) shows the effect of load difference on the synchronization process. The figure represents three cases

for the load difference on the induction motors shafts. ($L_1 = (1.5\_2\_2.5)L_2$)

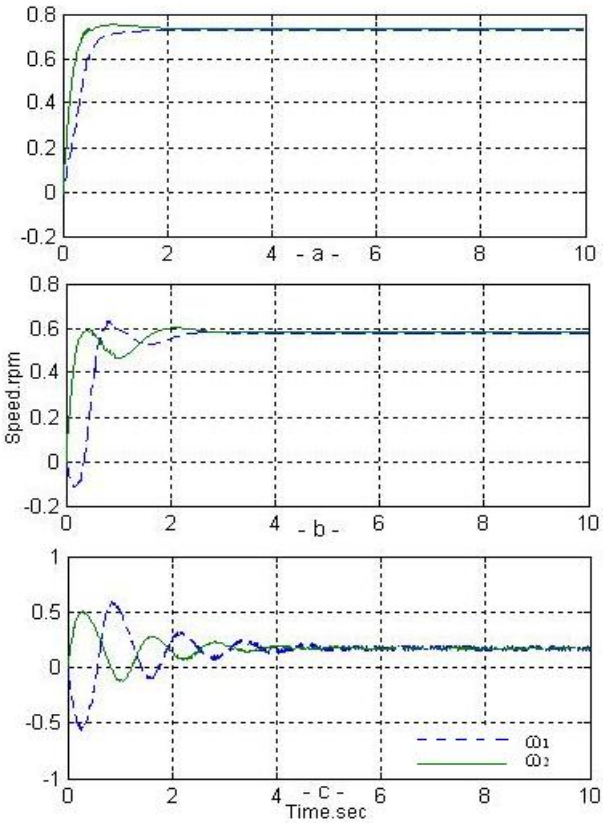

Figure 9. Speed response when rated R'_M ,
(*a*) $(L_1 = 1.5L_2)$,(*b*) $(L_1 = 2L_2)$
(*c*) $(L_1 = 2.5L_2)$.

*In figure 8-a $(L_1 = 1.5L_2)$, the system has the best synchronous capability with the best recovery time.

*In figure 8-b $(L_1 = 2L_2)$, the system has a medium synchronous capability with little vibration.

*In figure 8-c $(L_1 = 2.5L_2)$, the system has the worst synchronous capability with the longest recovery time and high system vibration.

5. Conclusion

The design of the electromagnetic shaft systems depends on the motors power because it depends on the value of R'_M , and by changing this value, the dimensions of the inductive reactance and the synchronous capability will be determined [5].

The effect of R'_M on the synchronous capability and recovery time depends on the load distribution, if the load distribution is greater than the rated value, then the R'_M effect will decrease and the system vibration will increase. Therefore, to have a more stable system with less vibration, the maximum load difference must be determined before choosing the inductive reactance element for the system.

The required recovery time for the synchronization process of the system will be faster in the implementation than the calculated values because of the presentation of the gear box where the speeds are reduced to the tenth of its maximum speed.

References

[1] Howard I, Jay P, Lawrence T. Cranes and derricks. Copyrighted Material; 1991.

[2] A.S. Al-Akayleh, S. Abdallah, "The systems of Synchronous rotation in the base of electromagnetic working shaft with insertion capacitances in the rotor coils". Production Jordan Journal of Applied Science, Natural Sciences, Vol. 7, 2005,.

[3] A.S. Al-Akayleh, "Synchronization of induction motors rotation in the multi-motor drive systems". The International Carpathian Control Conference, ICCC'2004, Zakopane, Poland, May,25-28, 2004.

[4] A.S. Al-Akayleh, " The synchrono rotation of AC machines". Proceding of the 5t Middle East Symposium on Simulation and Modeling MESM, Sharjah, UAE, January 5-7, 2003.

[5] Osmanhadjaev, N . M, Kadirov , M . T. "Calculation of inductive reactance dimensions for IM synchronous rotation drives, in the base of electromagnetic working shaft", Russia Electro-mechanic ,Vol. 9, 1991, 118-126.

[6] A.S. Al-Akayleh, S. Abdallah, "The systems of Synchronous rotation with AC motors in the base of electromagnetic working shaft". Proceeding of the InternationaL Engineering Conference, Mutah, Jordan, April 26-28, 2004.

JJMIE

Volume 3, Number 2, June. 2009
ISSN 1995-6665
Pages 157 - 160

Jordan Journal of Mechanical and Industrial Engineering

Evaluating the Effects of High Velocity Oxy-Fuel (Hvof) Process Parameters on Wear Resistance of Steel-Shaft Materials

Adnan Al-Bashir [a], A. K. Abdul Jawwad [*,b], Khaleel Abu Shgair [c]

[a] Industrial Engineering Department, The Hashemite University, P.O.Box: 150459, Zarqa 13115, Jordan

[b] Industrial Engineering Department, University of Jordan, Amman 11942- Jordan

[c] Mechanical Engineering Department, Faculty of Engineering Technology, Al-Balqa' Applied University, P.O. Box 15008, Amman 11134, Jordan

Abstract

Thermal spray processes are widely used in industries to compensate for worn surfaces of different power transmission steel shafts. These include plain carbon, alloyed and stainless steels. This comes as a means of saving the worn parts by reusing them after they have been thermally sprayed by suitable wear-resistant coatings. As there are several factors to be controlled in this process, this makes it necessary to get the best combination of process parameters to provide the required level of wear resistance and, hence part life. In this study the oxy-fuel process is applied to 4140 alloy steel. Process parameters have been varied using a 2^k experimental design. The Pin-on-Disc test was used to estimate the wear resistance of the different material-coating-parameters combinations. The data were analyzed and a statistical model, explaining the effect(s) of different parameters as well as their interaction, was obtained.

Keywords: Statistical Modeling; Design of Experiments; High Velocity Oxy Fuel (HVOF)

1. Introduction

High velocity oxy fuel (HVOF) flame spray process is one of the most widely spread thermal spraying techniques used for the repair of worn parts such as power transmission shafts and other parts which experience continuous sliding contact [1-2]. This provides an economical and a more environmentally sound alternative for scrapping of these parts [1] and/or other coating techniques such as hard chromium plating [3-4]. A great effort has been recently devoted to investigating the HVOF process including the effect of microstructure of HVOF-sprayed coatings [5-8], in-flight particle properties [[9-11] and process parameters [8-12] on the resulting wear behaviour. In the above studies, a general trend has been observed as to the effect of in-flight particle properties on the resulting microstructure and wear resistance of the coatings; the higher the particles' velocity and temperature the denser, more coherent and more wear resistant the coating is. Studies which involved the effect of process parameters have considered several process parameters such as carrier gas flow rate [8,10], stand off distance [8-12], powder feed rate [9-10,12] and substrate surface speed [9]. These studies indicated major factors controlling the particle in-flight properties, and hence wear behaviour to be the powder feed rate and the gas flow rate, while there has been some ambiguity about the effect of stand off distance on the in-flight particle properties and the resulting wear behaviour [8,9]. This uncertainty and lack of accurate distinction of the different effect(s) of the various spraying factors may, very well, be due to their interaction effects, which have not been dealt with in the previous attempts [9]. In the light of the above a need for a more distinguishing method of analysis is obvious, i.e. a proper methodology should be able to, quantitatively; determine the effects of the various process parameters as well as their interaction effects which some times could be more prominent that the effects of separate factors themselves [13]. In this study a full factorial 2^k design of experiments (DOE) has been employed to pre-plan the experiments for further analysis of the results. Factors investigated in this study were fuel gas pressure (substitute for gas flow rate); stand off distance and rotational speed of shafts (pins) during the coating process.

2. Materials and Experimental Procedure

The substrate material used in this study was 4140 alloy steel with composition shown in Table 1. 8-mm diameter rods were prepared by turning from an original stock of 65 mm diameter for the purpose of HVOF spraying. The coating material used in this study is a commercially available iron-based coating (Eutalloy RW 19400) produced by Castolin Eutectic, Table 1. Spray parameters investigated in this study included fuel gas

* Corresponding author. akjawwad@ju.edu.jo

(acetylene gas) pressure; stand off distance and rotational speed of shafts (pins) during the coating process. Two levels (high and low) were used for each factor, Table 2, yielding eight different experimental combinations, Table 3. After spraying, pins were tested for wear, using the pin-on-disc test with 25 N test load and 250 rpm at 180 mm diameter. Mass loss was measured by a sensitive balance every 15 minutes with a total number of four readings recorded for each experiment. As cross sectional areas differed slightly among different specimens, mass loss data were corrected to reflect this variation and final values of mass loss per unit area were reported for analysis purposes.

Table 1. Chemical composition of substrate (4140 alloy steel) and coating material wt.%.

Material	Fe	Mn	Cr	Mo	C	Si	Ni	P
Substrate	Bal.	1	1.1	0.2	0.4	0.25	--	0.03
Coating	Bal.	0.08	16		0.26	0.9	1.87	

Table 2. Low and high values used for the different spray parameters.

Parameter (symbol)	Low	High
Acetylene gas pressure (C), Bar	3	10
Stand off distance (A), mm	100	400
Rotational speed (B), rpm	100	650

Table 3. Parameter combinations used for the different HVOF spray trials.

Experiment No.	Fuel gas pressure	Rotational speed	Stand off distance
1	High	High	High
2	High	High	Low
3	High	Low	High
4	High	Low	Low
5	Low	High	High
6	Low	High	Low
7	Low	Low	High
8	Low	Low	Low

3. Results and Discussion

The designed experiments were performed and the output of each experiment was recorded as a mass-loss (to be considered as response) as shown in Table 4.

The results, qualitatively, indicate the following general trends (i) mass loss decreased with increasing gas pressure; (ii) at the same pressure- level-rotational-speed combination, the mass loss decreased with increasing the stand off distance with this effect being more evident at high pressure levels, indicating a stronger interaction and (iii) rotational speed does not seem to have a large impact on the average mass loss.

These experiments were analysed, Figure 1, and a statistical model was obtained, (1). Figure 1 shows the half normal probability plot of the effects' estimates for the above experiments. This is a plot of the absolute value of the effect estimates against their cumulative normal probabilities. Many analysts feel that the half-normal plot is easier to interpret, particularly when there are only a few effect estimates such as when the experimenter has used an eight-run design similar to the case in this paper.

Table 4. Parameter combinations used for the different HVOF spray trials and their respective average mass loss (mg/mm^2).

Experiment No.	A Distance mm	B R. Speed rpm	C Pressure Bar	Response Av. Mass loss mg/mm^2
1	400	650	10	0.008
5	100	650	10	0.027
3	400	100	10	0.010
7	100	100	10	0.045
2	400	650	3	0.033
6	100	650	3	0.039
4	400	100	3	0.051
8	100	100	3	0.037

The important effects that emerge from this analysis (indicated by their large distance from the straight line) are the gas pressure (C), the stand off distance (A) and the interaction between these two factors (AC). The rotational speed, however, does not have the same level of effect. The acetylene gas pressure in the model (1), also appears to be the dominant factor in the average loss of mass model, followed by the interaction effect between gas pressure and stand off distance and then by the stand off distance as a separate factor.

Figure 1 and the statistical model (eqn. 1) also show an effect of the three-factor interaction, (ABC) on the average mass loss. This ABC interaction has more effect on the average mass loss than the rotational speed factor alone, indicating the fact that interaction effects could exceed the effects of some principal process parameters.

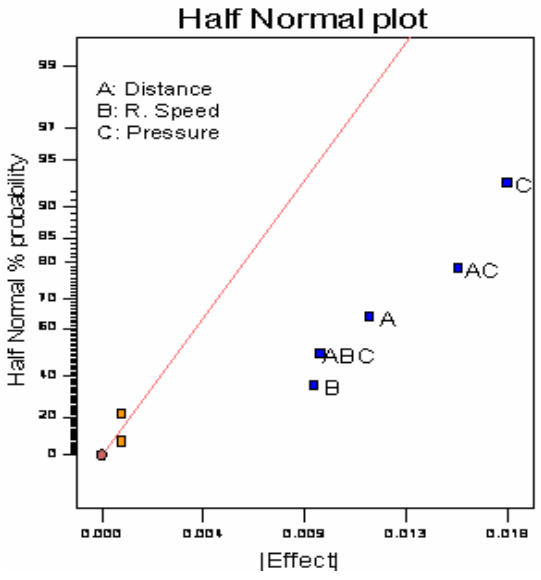

Figure 1. Effects of different factors on the average mass loss.

$$Av.\ Loss = +0.031 - 0.0058*A - 0.0046*B - 0.0086*C - 0.0077*AC + 0.0048*ABC \quad (1)$$

To check the adequacy of the model above, normality assumption should be checked. Residual analysis is an efficient and major tool used in this diagnostic checking. The model is tested against normality of its residuals, Figure 2, indicating no presence for any outliers nor indication of non-normality. The general impression from examining this figure is that the error is approximately normal. The tendency of the normal probability plot to bend down slightly on the left side and upward slightly on the right side implies that the tails of the error distribution are somewhat thinner than would be anticipated in normal distribution.

The experiments were performed randomly, and in order to check the independence assumption, plotting the residuals in time order of the data was performed as shown in Figure 3. A tendency to have runs of positive and negative residuals indicates positive correlation. Figure 3, shows no correlation between residuals.

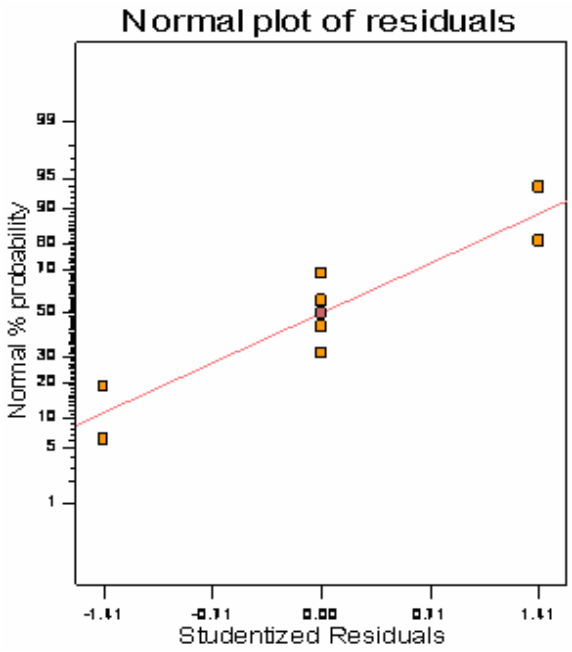

Figure 2. Normal Plot of Residuals.

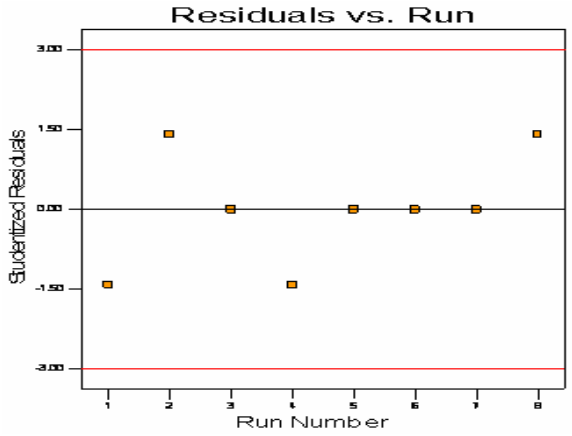

Figure 3. Plot of residuals versus run order or time.

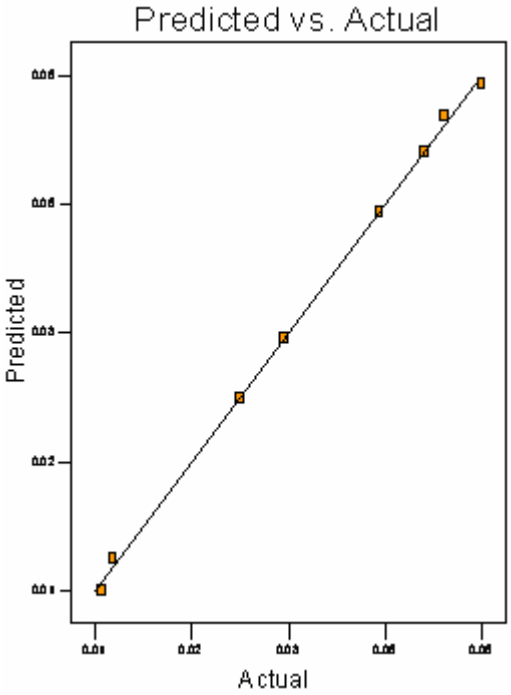

Figure 4. Plot of actual versus predicted values.

Another test on the prediction model is comparing the actual values against their corresponding predicted values obtained from the model. Figure 4, provides a clear picture of the negligible differences between the predicted values and the actual ones indicating adequacy of the obtained statistical model.

The analysis of variance (ANOVA) for the selected factorial model, Table 5, was significant with p-value = 0.0044, against F-value of 225. There is only a 0.44% chance that a "Model F-Value" this large could occur due to noise. Also it is evident from the ANOVA that all the model terms were significant .

As mentioned above, the two-factor-interaction effect between the acetylene pressure and the stand off distance (AC) had more prominent effect than the rotational speed factor. This interaction effect is evident in Figure 5, where greater mass losses are favored by a low gas pressure and a high stand off distance.

When the level of the gas pressure is high and the stand off distance level is high, then the average mass loss is the minimum. While, if the level of the gas pressure is low and the stand off distance level is high, the average mass loss is high.

4. Conclusion

Wear resistance of HVOF coating (represented by mass loss) is affected by the respective process parameters such as, fuel gas pressure (flow rate), stand off distance and speed. In this study a statistical model was developed covering all the above factors in one equation. It is clear that the effect of the gas pressure seems to be the greatest, followed by the interaction between the gas pressure and the stand off distance. The rotational speed did not show a significant level of effect on the average mass loss. The model adequacy seems to be high, as excellent agreement

between experimental and predicted values has been observed.

Table 5. Analysis of variance for the statistical model.

ANOVA for Selected Factorial Model					
	Sum of		Mean	F	
Source	Squares	DF	Squares	Value	Prob. > F
Model	1.72E-03	5	3.45E-04	225.13	0.0044
A	2.7E-04	1	2.7E-04	176.51	0.0056
B	1.71E-04	1	1.71E-04	111.76	0.0088
C	6.21E-04	1	6.21E-04	405.73	0.0025
AC	4.81E-04	1	4.81E-04	313.80	0.0032
ABC	1.81E-04	1	1.81E-04	117.88	0.0084
Residual	3.06E-06	2	1.53E-06		
Total	1.73E-03	7			

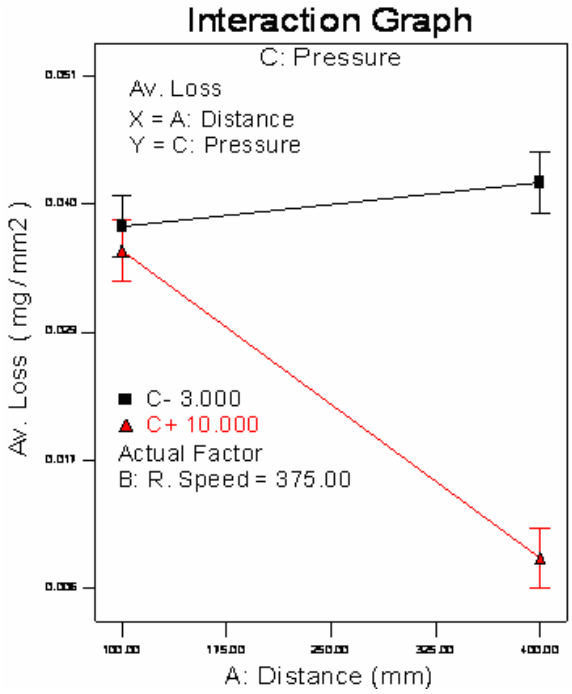

Figure 5. Pressure-Distance interaction effect on average mass loss.

Acknowledgment

The authors would like to thanks The Jordan Petrol Refinery Co. for providing the materials and facilitating the experimental work and Castolin Eutectic for providing the coating data.

References

[1] T. Sharaoui, N. Fenineche, G. Montavon, C. Coddet, "Alternative to chromium: Characteristics and wear behavior of HVOF coatings for gas turbine shafts repair (heavy duty)". Mat. Proc. Tech., Vol. 152, 2004, 43-55.

[2] T. Sudaprasert, P.H.Shipway, D.G. McCartney, "Sliding wear behaviour of HVOF Sprayed WC-Co coatings deposited with both gas-fuelled and liquid-fuelled systems". Wear, Vol. 255, 2003, 943-949.

[3] T. Sharaoui, N. Fenineche, G. Montavon, C. Coddet, "Friction and wear behaviour prediction of HVOF coatings and electroplated hard chromium using neural computation". Mat. Let., Vol. 58, 2004, 654-660.

[4] J.A. Picas, A. Forn, A. Igartua, G. Mendoza, "Mechanical and tribological properties of HVOF thermal sprayed nano crystalline CrC-NiCr coatings". Surf. & Coat. Tech., Vol. 174-175, 2003, 1095-1100.

[5] E. Fleury, S.M. Lee, J.S. Kim, D.H. Kim, W.T. Kim, H.S. Ahn, "Tribological properties of Al-Ni-Co-Si quasicrystalline coatings against Cr-coated cast Iron disc". Wear, Vol. 253, 2002, 1057-1069.

[6] H. Liao, B. Normand, C. Coddet, "Influence of coating microstructure on the abrasive wear resistance of WC/Co cermet coatings". Surf. & Coat Tech., Vol. 124, 2000, 235-242.

[7] Yang, Q., Senda, T. and Ohmori, A., "Effect of Carbide Grain Size on Microstructure and Sliding Wear Behaviour of HVOF-Sprayed WC-12%Co Coatings". Wear, **254**, 2003, p 23-34.

[8] J. Wang, K. Li, D. Shu, X. He, B. Sun, Q. Guo, M. Nishio, H. Ogawa, "Effects of structure and processing technique on properties of thermal spray WC-Co and NiCrAl-WC-Co coatings". Mat. Sci. Eng., Vol. A 371, 2004, 187-192.

[9] W. Lih, S. Yang, C. Su, S. Huang, I. Hsu, M. Leu, "Effects of process parameters on molten particle speed and surface temperature and properties of HVOF CrC/NiCr coatings". Surf. & Coat. Tech., Vol. 133-134, 2000, 54-60.

[10] L. Zhao, M. Maurer, F. Fischer, R. Dicks, E. Lugscheider, "Influence of spray parameters on the particle in-flight properties and the properties of HVOF coating of WC-CoCr". Wear, Vol. 257, 2004, 41-46.

[11] T. Zhang, D.T. Gawne, Y. Bao, "The influence of process parameters on the degradation of thermally sprayed polymer coatings". Surf. & Coat. Tech., Vol. 96, 1997, 337-334.

[12] J.C.Tan, L. Loonney, M.S.J. Hashmi, "Component repair using HVOF thermal spraying". J. Mat. Proc. Tech., Vol**. 92-93**, 1999, 203-208.

[13] Montgomery DC. Design and analysis of experiments. 6th ed. New York: John Wiley and Sons; 2005

المملكة الأردنية الهاشمية

الجامعة الهاشمية

المجلة الأردنية
للهندسة الميكانيكية والصناعية

JJMIE

مجلة علمية عالمية محكمة

http://jjmie.hu.edu.jo/

ISSN 1995-6665

المجلة الأردنية للهندسة الميكانيكية والصناعية
مجلة علمية عالمية محكمة

المجلة الأردنية للهندسة الميكانيكية والصناعية: مجلة علمية عالمية محكمة أسستها اللجنة العليا للبحث العلمي، وزارة التعليم العالي والبحث العلمي، الأردن، وتصدر عن عمادة البحث العلمي والدراسات العليا، الجامعة الهاشمية، الزرقاء، الأردن.

هيئة التحرير

ترسل البحوث إلى العنوان التالي :

رئيس تحرير المجلة الأردنية للهندسة الميكانيكية والصناعية
عمادة البحث العلمي والدراسات العليا
الجامعة الهاشمية
الزرقاء - الأردن
هاتف : 3903333 5 00962 فرعي 4147
Email: jjmie@hu.edu.jo
Website: www.jjmie.hu.edu.jo